Titre: Title:	New Methods for the Design of Wideband Reflectarrays and Reconfigurable Metasurfaces
Auteur: Author:	Pablo Emilio Camacho Prieto
Date:	2025
Type:	Mémoire ou thèse / Dissertation or Thesis
Référence: Citation:	Camacho Prieto, P. E. (2025). New Methods for the Design of Wideband Reflectarrays and Reconfigurable Metasurfaces [Thèse de doctorat, Polytechnique Montréal]. PolyPublie. https://publications.polymtl.ca/62690/

URL de PolyPublie: PolyPublie URL:	https://publications.polymtl.ca/62690/
Directeurs de recherche: Advisors:	Elham Baladi, & Mohammad S. Sharawi
Programme: Program:	Génie électrique

POLYTECHNIQUE MONTRÉAL
affiliée à l'Université de Montréal

New Methods for the Design of Wideband Reflectarrays and Reconfigurable Metasurfaces

PABLO EMILIO CAMACHO PRIETO
Département de génie électrique

Thèse présentée en vue de l'obtention du diplôme de *Philosophiæ Doctor*
Génie électrique

Janvier 2025

POLYTECHNIQUE MONTRÉAL
affiliée à l'Université de Montréal

Cette thèse intitulée :

New Methods for the Design of Wideband Reflectarrays and Reconfigurable Metasurfaces

présentée par **Pablo Emilio CAMACHO PRIETO**
en vue de l'obtention du diplôme de *Philosophiæ Doctor*
a été dûment acceptée par le jury d'examen constitué de :

Ke WU, président
Elham BALADI, membre et directrice de recherche
Mohammad S. SHARAWI, membre et codirecteur de recherche
Jean-Jacques LAURIN, membre
George V. ELEFTHERIADES, membre externe

DEDICATION

A mi menina, por tu eterno apoyo,
A mis viejos, soy pan, soy paz soy más, soy el que está por acá gracias a ustedes
To those who know depression... there is always a light.

ACKNOWLEDGEMENTS

First, I want to thank my directors, Professor Elham Baladi and Professor Mohammad Sharawi. Doing the PhD has always been my objective, and Prof. Sharawi trusted in my capabilities and allowed me to join his group. I appreciate his tenacity, exigence, and humanity in directing his students. Similarly, working with Prof. Baladi has been a pleasure. She became my director at the last moment. In the short time I have worked with her, I have seen her passion for research. I sincerely thank her for her support and advice, and I hope we can collaborate in the future. I also thank Professor Ke Wu for serving as jury president of the thesis and Professor Jean-Jacque Laurin and Professor George Eleftheriades for serving as jury.

Secondly, I thank the staff of Polygrames, and I give immense thanks to Vincent Rolko for his support in the measurements. The measurements of the reflectarrays required lots of effort, hundreds of tries, and a considerable amount of patience; the results would have been impossible without his help. Thanks to the fabrication staff, Traian Antonescu for his very efficient labor in the PCB fabrications, and Steve Dubé for his support on the waveguide fabrication.

Thirdly, thanks to MITACS, which partially sponsored the reflectarray project through its acceleration program in partnership with Professors Sharawi, Professor Baladi, and MDA Space. I am grateful to many people from MDA Space who have helped me with the project: Francesco Coccimiglio and Anthony Palmeri, who helped me think about and prepare the measurement setup. Virginie Dupessey and Maria Brumos who have opened the doors of MDA to me. And an exceptional thanks to Karim Glatre, who was very involved in the project and always shared his helpful advice. Moreover, we have had various exciting discussions about ideas and solutions for designing antennas and very nice conversations about music.

Last but not least, to three of the most important people in my life. To *mamá*, *papá* and *hermanito*. I could write a book about all my thoughts and feelings for them, but this is beyond the reader's interest. For instance, a simple *gracias, infinitamente gracias* is enough. You fill my heart, my soul, my all. There is one last special person to whom no book is enough for describing my feelings and gratitude: to my fiancee, *mi menina*, who has been the most supportive, lovely, special, and ∞ person in this journey (and hopefully for our whole life).

A special mention to my friends, David, Dani, Juan, Yury, Violeta, Laura, Clau, Xime, Carlos,

Juan, Laura, Eray, and a long etcetera to avoid another paragraph. Also, to my laboratory colleagues Mohammad Moradi, Rash, Farhad, Guillaume Ndjamba, Lamine Bamogho, and again a long etcetera (and an apology to the ones I have forgotten!).

RÉSUMÉ

La demande croissante d'interconnexion et de trafic de données pour les applications des villes intelligentes s'est développée parallèlement à l'intérêt sur les surfaces périodiques de la communauté qui travaille en antennes. Ce domaine, qui inclut les métasurfaces, les surfaces sélectives en fréquence, les réseaux réflecteurs et les réseaux transmitteurs, est devenu clé pour trouver des solutions potentielles dans l'avenir des télécommunications. C'est avec cette idée, que cette thèse explore des surfaces périodiques pour deux applications : premièrement, on explore des réseaux réflecteurs de grandes ouvertures pour des applications à large bande et double bande applicables aux communications par satellite dans les ondes millimétriques. Deuxièment, on explore des métasurfaces reconfigurables pour le contrôle du faisceau dans le spectre sub-6 GHz pour des applications 5G.

La première partie de la thèse se concentre sur les réseaux réflecteurs à multiples surfaces comme alternative économique et légère aux réflecteurs paraboliques. En particulier, la recherche aborde les limitations de la largeur de bande du gain pour des réflecteurs avec des grandes ouvertures ($\geq 40\lambda_0$) dans les bandes Q et V (37.5–42.5 GHz et 47.2–51.4 GHz respectivement). La thèse propose une méthodologie pour concevoir des réseaux réflecteurs à multiples surfaces afin de minimiser les erreurs de phase sur la bande de fréquence, améliorant ainsi la largeur de bande du gain. Cette méthodologie comprend le développement de cellules unitaires à une et deux bandes avec une large couverture de phase, des faibles pertes ainsi qu'un bon rapport axial. Cette méthodologie nécessite également l'étude d'un mode d'évaluation alternative pour estimer de manière rapide et efficace le gain et le patron de rayonnement des réseaux réflecteurs à multiples surfaces et à grande ouverture. À cet effet, l'approche par réseau (*array approach*) est étendue pour évaluer les réseaux réflecteurs. L'application de cette méthodologie permet d'estimer le patron de rayonnement et la largeur de bande du gain en quelques minutes, tandis que les simulations avec des logiciels commercials requièrent plusieurs jours (ou même des semaines) pour finir les calculs. Les résultats de cette partie incluent une analyse théorique et des mesures dans une base compacte de mesure d'antennes pour un réseau réflecteur à une et à deux bandes. Le cas à une bande montre une amélioration du patron de rayonnement, étant la seule configuration capable de maintenir un faisceau-crayon sur une large plage de fréquences, avec des largeur de bande de gain à 1 dB et à 3 dB de 13.4% et 25.6% respectivement, et un rapport axial inférieur à 0.9 dB. De l'autre côté, l'antenne à deux bandes présente des limitations sur son rapport axial atteignant 3.5 dB, En revanche, sa largeur de bande de gain dépasse 5% et 7% dans les deux bandes, ce qui la rend comparable ou meilleure que les travaux précédents.

La deuxième partie de la thèse traite des métasurfaces reconfigurables intégrées dans des radômes pour des applications d'orientation de faisceau en temps réel. La thèse explore l'intégration de la bianisotropie pour atteindre des réfractions à large angle, en abordant les limitations des métasurfaces anisotropes conçues avec des gradients de phase. Ce travail introduit une analyse complète des exigences d'impédance et une nouvelle conception des cellules unitaires avec une capacité de réglage sur une plage de 250 Ω, dépassant largement la plage de 100 Ω que montrent des travaux précedents. La méthodologie traite également des défis tels que les pertes d'insertion et les effets de couplage inter-couches, avec une validation par des simulations et des mesures en guide d'onde. Les capacités anisotropes et bianisotropes de la cellule unitaire sont démontrées par des simulations d'une supercellule, montrant une capacité d'orientation de faisceau de $\pm$ 30° en mode anisotrope et de 59° en mode bianisotrope avec une efficacité de 86%. Enfin, la cellule unitaire est également évaluée par des simulations en dans une métasurface composée de 12x12 cellules unitaires avec des lignes d'alimentation de polarisation des diodes varacteurs, permettant une orientation de faisceau jusqu'à 30° dans un plan.

ABSTRACT

The increasing demand for interconnection and data traffic for smart city applications has grown in parallel with the interest of the antenna community in research on periodic surfaces. This topic, which includes metasurfaces, frequency selective surfaces, transmitarrays, and reflectarrays, has become the key to potential solutions for the future of telecommunications. This thesis investigates two novel applications of periodic surfaces: wideband and dual-band, large-aperture reflectarrays for satellite communications in the millimeter-waves and reconfigurable metasurfaces for beam tilting in sub-6 GHz 5G networks.

The first part of the thesis focuses on multi-faceted reflectarrays as a cost-effective and lightweight alternative to parabolic reflectors. Specifically, the research addresses the limitations of bandwidth and for large-aperture sizes ($\geq 40\lambda_0$) in the Q- and V-bands (37.5–42.5 GHz and 47.2–51.4 GHz respectively). The thesis proposes a methodology to design multi-faceted reflectarrays to minimize phase error across the frequency, enhancing gain bandwidth. This methodology includes developing single-band and dual-band unit cells with wide phase coverage, low losses, and good axial ratio. Moreover, it requires the study of an alternative for fast and efficient evaluation of large-aperture multi-faceted reflectarrays. For this reason, the array approach method is extended to evaluate multi-faceted reflectarrays. Applying this methodology allows us to estimate the radiation pattern and gain bandwidth in minutes, in contrast to the days (or even weeks) that take full-wave simulations. The results of this part of the thesis include theoretical analysis and measurements in a compact antenna test range of a single-band and a dual-band multi-faceted reflectarray. The single-band case shows an improvement in the radiation pattern, being the only configuration capable of maintaining a pencil beam in a wide range of frequency, as well as a 1-dB and 3-dB gain bandwidth of 13.4% and 25.6% and an axial ratio below 0.9 dB. On the other side, the dual-band antenna has limitations on the axial ratio with values up to 3.5 dB, but its gain bandwidth is more than 5% and 7% in the two bands, which makes it comparable or better than previous reports.

The second part treats reconfigurable metasurfaces embedded into radomes for real-time beam tilting applications. The thesis explores the integration of bianisotropy to achieve wide-angle refractions, addressing the limitations of beam tilting in anisotropic metasurfaces designed with phase gradients. This work introduces a comprehensive analysis of impedance requirements and a novel unit cell design with tunability within a range of 250 Ω, significantly exceeding the conventional 100 Ω range. The methodology also addresses challenges such as insertion losses and inter-layer coupling effects, with its effectiveness validated through full-

wave simulations and waveguide measurements. The anisotropic and bianisotropic capabilities of the unit cell are proved by full-wave simulations of a supercell showing a beam tilting capability of ± 30° on its anisotropic mode and to 59° on its bianisotropic mode with 86% of efficiency. Finally, the unit cell is also evaluated by full-wave simulations in a metasurface of 12x12 unit cells with the biasing feedlines for beam tilting up to 30° in one plane.

TABLE OF CONTENTS

LIST OF TABLES

LIST OF FIGURES

LIST OF SYMBOLS AND ABBREVIATIONS

RA	Reflectarray
UC	Unit cell
BW	Bandwidth
AA	Array approach
CATR	Compact antenna test range
HPBW	Half power beamwidth
SLL	Sidelobe levels

LIST OF APPENDICES

CHAPTER 1 INTRODUCTION

1.1 Motivation

All the current investigations in the antenna field agree on one statement: we are looking for solutions that allow us to satisfy the continuously growing data traffic. Every time, more devices are interconnected, and this dynamic requires new technologies with antennas that satisfy the new requirements. Among the novel topics in the antenna community, one that has shown potential solutions to these new demands is periodic surfaces.

Periodic surfaces might be considered as a young topic. Just two decades ago (in 2000), Smith et al. published the first paper reporting measurements of a metamaterial [3]. Earlier, in 1968, Munk had studied the frequency selective surfaces (FSSs) to then publish a book about it in 2000 [4]. Today, hundreds of contributions based on metasurfaces, FSSs, reflectarrays, and transmitarrays propose solutions for addressing the challenges of the upcoming telecommunication networks. This thesis enters into this category. Nonetheless, instead of focusing on a single type of surface for a specific spectrum of frequency, the thesis addresses two different problems: reflectarrays in millimeter-waves for satellite communications and reconfigurable Huygens' metasurfaces embedded in a radome for applications in the sub-6 GHz spectrum of 5G networks.

The first topic is a research on reflectarrays done in partnership with MDA Space. Reflectarrays are a technology of interest for the space industry as they offer various advantages over parabolic reflectors. Reflectarrays offer easier and cheaper fabrication, lighter weight, and easier deployment. However, its main disadvantage is its narrow bandwidth, which becomes more critical for larger apertures. The motivation of the research is the proposition of a methodology to design large aperture size reflectarrays with wideband and/or multi-band capability for the unexplored Q and V bands.

The second topic is reconfigurable metasurfaces for beam scanning. The motivation of this topic is to respond to the requirement of smart cities, where devices are capable of real-time, limitless scanning of the environment. In this case, we pictured radomes integrated with metasurfaces for WLAN applications (around 2.4 GHz). Our goal is to explore a metasurface capable of beating the blind angles of common beam scanning. For this reason, we explored a methodology to design unit cells that, besides typical phase-gradient, integrate bianisotropy for wide refraction.

In summary, while the two topics cover different applications at different frequencies, the

complete thesis explores periodic surfaces as a potential solution to respond to the challenges posed by the upcoming networks.

1.2 Problem Statement

1.2.1 Reflectarrays

Over the past two decades, RA antennas have become one of the main topics in academia and are gaining attention in the space industry. Their advantages include ease of fabrication, lightweight design, and deployability. The great interest in this topic has led to numerous contributions, as summarized by the mind map in Fig. 1.1. The center of the map cites books and surveys that are relevant for a first insight into this topic [5–11]. The branches highlight the common characteristics for space RAs: circular polarization, wideband or multiband coverage for uplink and downlink communication (X, K_a, and K_u are the most common bands), and high gain to mitigate atmospheric attenuation.

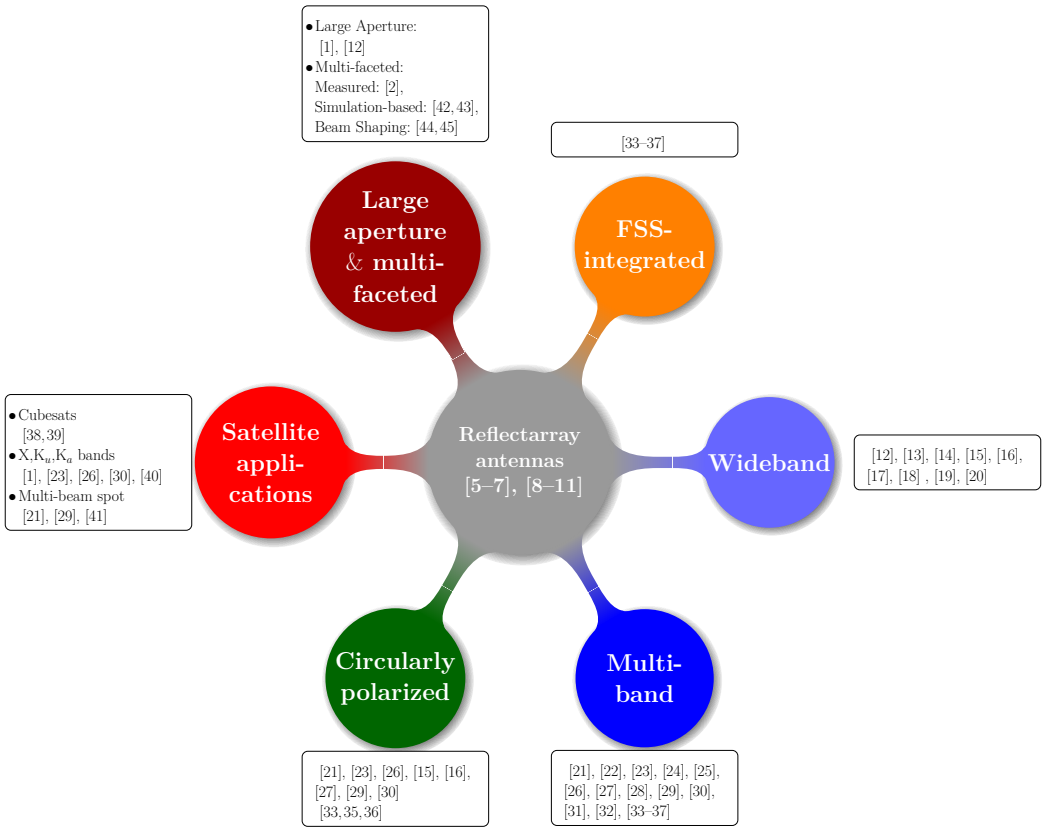

Figure 1.1 Mind map of literature review on reflectarray antennas

One of the current challenges in the field of satellite communications is the development of

technology at higher frequencies to overcome the congestion in the X, K_a, and K_u bands [46, 47]. These new frequencies are the Q-band (37.5–42.5 GHz for downlink) and V-band (47.2–51.4 GHz for uplink). However, despite their importance, these bands remain mostly unexplored for RAs. Most existing designs focus on one of the bands (e.g., Q-band [13, 14], V-band [32]) and are limited to small apertures ($<20\lambda_0 \times 20\lambda_0$). In contrast, these bands require larger apertures to be applicable in satellite telecommunications ($\gtrsim 30\lambda_0 \times 30\lambda_0$). This requirement responds to the necessity of high gain to overcome atmospheric attenuation. However, large apertures limit the gain bandwidth due to phase-wrapping effects. This challenge is evident in the RA described in [1] (Fig. 1.2a). Its aperture size is 5 m $\times$ 0.26 m (594 $\lambda_0 \times 32\ \lambda_0$ at 35.75 GHz), and it only performs at the frequency of design.

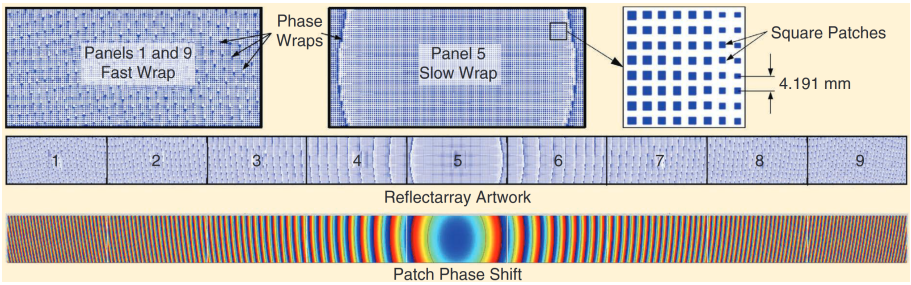

(a)

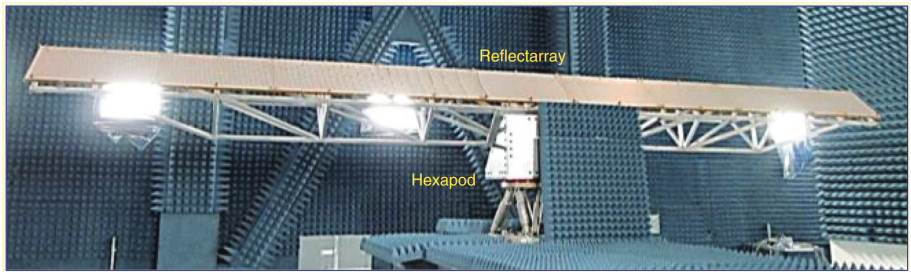

(b)

Figure 1.2 Picture of a 5 m x 0.26 m reflectarray operating at 35.75 GHz (K_a band) reported in [1] (a) phase distribution, and (b) photo of the prototype.

Efforts to address the bandwidth limitations primarily focus on UC-based methodologies, such as multi-resonant geometries [13, 15–17] and true-time delay (TTD) [12, 14, 18–20]. While multi-resonant UCs improve phase coverage, they increase insertion loss. Similarly, TTD designs can achieve broader phase unwrapping but introduce design complexity, and its functionality depends on the aperture size. An alternative approach is to modify the RA geometry using multi-faceted configurations, which have shown promising results for bandwidth improvement [42, 43]. However, these studies are primarily simulation-based, with limited experimental validation. The only work with measured results demonstrates reduced phase

wrapping using a multi-faceted configuration and an improvement in the gain bandwidth [2]. However, the design is limited to K_a and K_u bands, operates with linear polarization, and uses a small aperture ($18\lambda_0 \times 18\lambda_0$). Moreover, no methodology has been proposed for designing multi-faceted RAs, and features such as circular polarization, dual-band, and large-aperture size have not been explored.

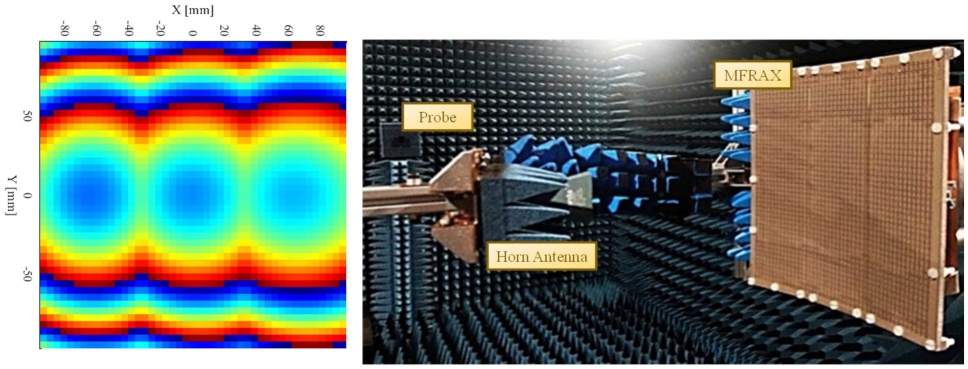

(a) (b)

Figure 1.3 Picture of a multi-faceted reflectarray operating in the K_a band reported in [2] (a) phase distribution, and (b) photo of the prototype.

In summary, the design of dual-band or wideband large-aperture RAs covering the Q- and V-band still needs to be explored. However, the existing methodologies are mostly UC-based and consider small aperture-size RAs. These solutions are insufficient for large aperture sizes because the phase wrapping remains. In contrast, the multi-faceted perspective addresses this challenge. However, the literature lacks a comprehensive methodology of design, experimental validation, and adaptation for circular polarization and dual-band operation. These gaps highlight the need for further research into multi-faceted, large-aperture, wideband, and dual-band RAs to address the growing demand for high-frequency satellite communication.

1.2.2 Reconfigurable metasurfaces

The growing demand for highly adaptive and efficient electromagnetic devices in applications like smart cities highlights the need for antennas capable of real-time and wide-angle beam capability. Metasurfaces are a potential solution for this requirement. This technology has transformed electromagnetic wave engineering, enabling dynamic control of wave behavior through precise impedance and susceptibility synthesis. However, existing reconfigurable metasurface designs face significant limitations that are strength by the inclusion of p-i-n and varactor diodes: insertion losses of up to 5 dB, restricted impedance tunability of less than

100Ω, and inadequate consideration of inter-layer coupling effects in multi-layer UCs leading to sub-optimal performance. These limitations are present in various reports referenced in the *beam tilting surfaces* branch of the mind map in Fig. 1.4. An overview shows that lens-based designs achieve a beam scanning up to 50° [48], while anisotropic surfaces hardly pass 30° [49, 50].

The existing beam tilting capability falls short of the requirements for *connected-to-everything devices* in smart cities. An unexplored solution is the integration of bianisotropy for wide refraction. This concept has been explored and tested in passive designs [51–53]. However, no existing work has demonstrated a comprehensive methodology for synthesizing UCs that combine anisotropic and bianisotropic properties. Such a UC requires wide impedance tunability of more than 200Ω, which exceeds the typical range offered by single-resonant UCs ($\leq$100Ω). Moreover, this UC requires a characterization of the inter-layer coupling effects to have precise impedance control.

This research aims to study and verify by measurements a methodology to design reconfigurable UCs for metasurfaces capable of beam tilting across any desired angle by addressing wide-impedance tunability and inter-layer coupling. This objective will be achieved through miniaturized, dual-resonant UCs. The offered perspective of this research gives an insight into challenges and solutions for implementing active metasurfaces. This contribution complements recent theoretical studies which rely on idealized, lossless materials [53–57], and to other experimental works which focus on magnitude and phase measurements and neglect impedance verification and coupling analysis. These new approaches are key for designing metasurface with limitless reconfigurability, enabling transformative applications for the upcoming telecommunications.

1.3 Objectives

This thesis covers reflectarrays and reconfigurable metasurfaces. Each topic has their respective general and specific objectives.

1.3.1 General objectives

The following conceptual map illustrate the composition of the thesis and includes the general objectives of it in the blue squares.

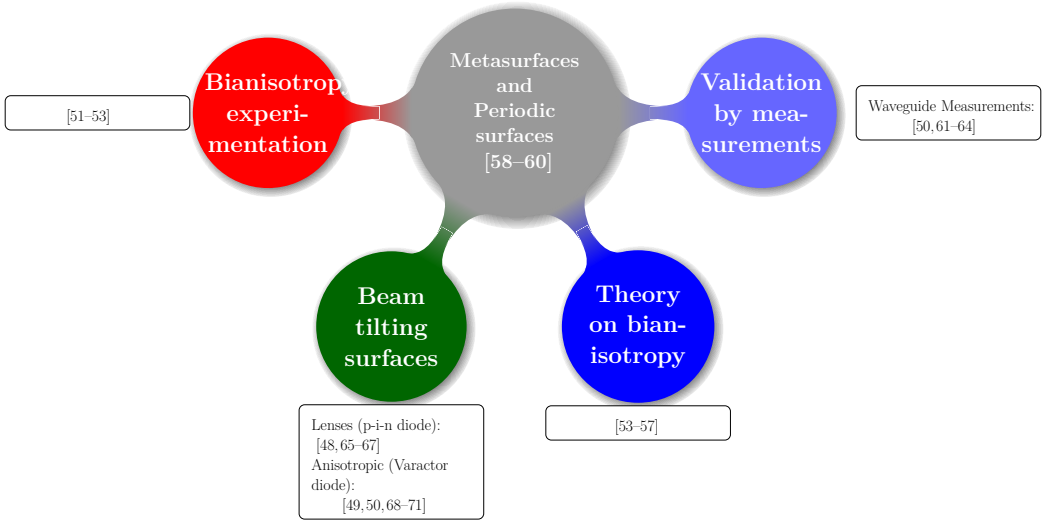

Figure 1.4 Mind map of literature review on metasurfaces

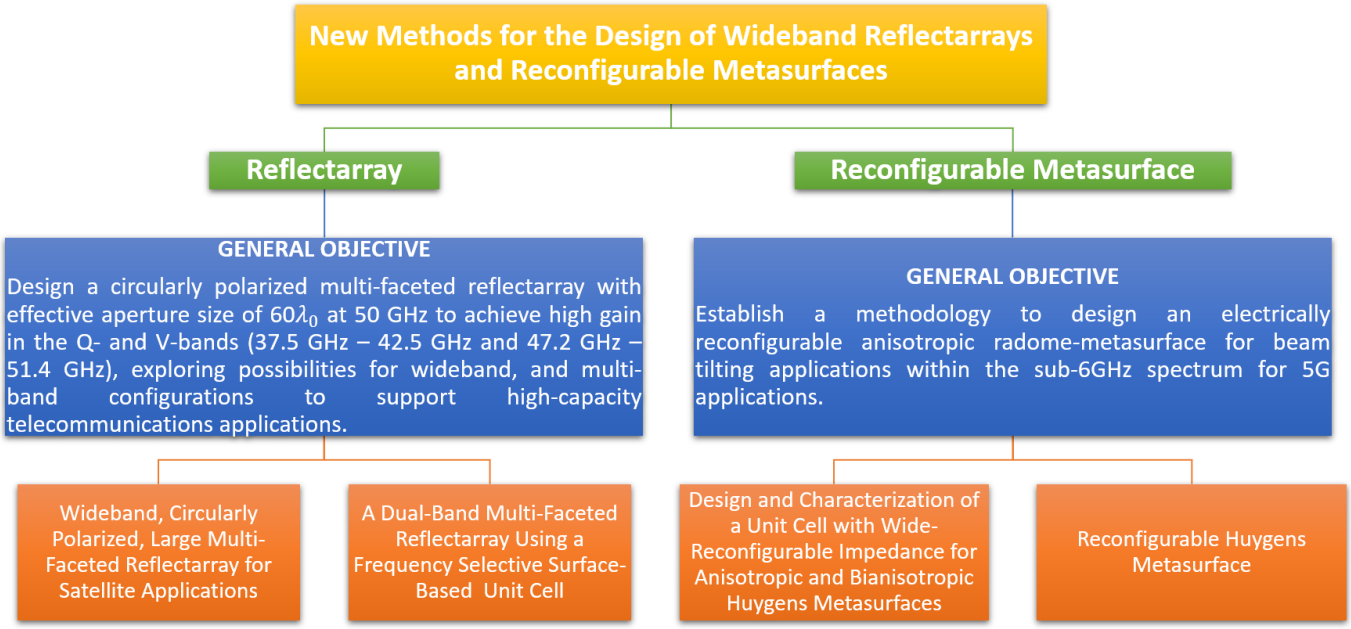

1.3.2 Specific objectives

Reflectarray

- Propose a single-band unit cell designed for optimal performance at 50 GHz, and having a phase coverage of at least 360° in the V-band and losses below -1 dB.
- Design a dual-band unit cell offering independent control in the Q- and V-bands offering a phase coverage of at least 360° in the two bands, as well as low losses.

- Establish a methodology to select the inclination of the reflectarray's faces, allowing a decrease in the phase error across the operational frequency range, using the proposed unit cells.
- Develop a code to estimate in a short time the radiation pattern and gain bandwidth of large, multi-faceted reflectarrays based on the array approach method.
- Compare the gain bandwidth and axial ratio of the multi-faceted reflectarray with single and dual-band unit cells.

Reconfigurable metasurface

- Propose a methodology to design a reconfigurable sub-wavelength unit cell to enable impedance reconfiguration meeting the conditions required for anisotropy and bianisotropy for beam tilting and wide-refraction applications.
- Characterize the impact of the inter-layer coupling in the reconfigurability of different geometries in a three-layer unit cell.
- Measure the reconfigurable reactance of the unit cells by a waveguide.
- Validate the applicability of the unit cell as an anisotropic and bianisotropic metasurface by full-wave simulations.
- Test the beam tilting capability of the metasurface up to 30° in one of the planes by full-wave simulations.

1.4 Thesis Organization

This thesis consists of four technical chapters. Chapters 2 and 3 present contributions related to reflectarrays, while Chapters 4 and 5 cover research on reconfigurable metasurfaces.

Chapter 2 presents advances in the design of a single-band, circularly polarized, multi-faceted reflectarray. The main contributions include a proposed methodology for optimally designing multi-faceted reflectarrays, an extension of the array approach to evaluate these types of reflectarrays, and performance validation through measurements. Additionally, the chapter demonstrates the advantages of the multi-faceted configuration over planar and previously reported multi-faceted antennas. The results show that the proposed array approach effectively estimates the radiation pattern and gain curve. Notably, the proposed reflectarray

maintains a pencil beam from 37.5 GHz to 51.4 GHz and achieves an axial ratio of less than 0.9 dB.

Chapter 3 presents a different approach to multi-faceted reflectarrays. The proposed reflectarray maintains the same parameters and requirements as in the previous chapter, but a new unit cell is introduced to enable independent control in the Q- and V-bands. The chapter's main contribution is a dual-band unit cell based on a frequency-selective surface, achieving a more compact design by eliminating air layers. Results show that the phase coverage at 40 and 50 GHz exceeds 400°. Gain measurements indicate that the unit cell achieves independent peaks at these two frequencies and exhibits a gain bandwidth superior to previous reports, while having a larger aperture size.

Chapter 4 presents a study of the impedance requirements and constraints for designing three-layer, reconfigurable unit cells for anisotropic and bianisotropic metasurface synthesis. The integration of these methodologies aims to address the impedance mismatch in anisotropic metasurfaces for wide-angle beam tilting by utilizing bianisotropic synthesis. This chapter defines the reactance requirements for the unit cells, proposes a methodology to meet these requirements, examines the inter-layer coupling effects on the unit cells, measures the reactances, and demonstrates their applicability to the intended applications through full-wave simulation. Notably, this chapter reveals for the first time the limitations of single-layer metasurface designs due to inter-layer coupling effects. It proposes a solution combining two types of unit cells to achieve integrated anisotropy and bianisotropy. The result is a supercell capable of tilting an incident wave up to ±30° applying phase gradient, and also capable to refract an incident wave to 58.25° on its bianisotropic mode. Chapter 5 extends the applicability of the unit cell proposed in the previous chapter by incorporating it into a metasurface composed of a 12x12 array of unit cells. The chapter provides insights into how biasing feedlines affect reactance reconfigurability and, based on these results, proposes the optimal configuration to test the beam tilting capability through full-wave simulations.

The thesis concludes in Chapter 6, which proposes future work and summarizes the most important contributions of the thesis.

CHAPTER 2 WIDEBAND, CIRCULATLY POLARIZED, LARGE MULTI-FACETED REFLECTARRAY FOR SATELLITE APPLICATIONS

2.1 Introduction

Reflectarray antennas are a mature technology. Various books and surveys exploring design methodologies and prototypes are found in the literature [5, 6, 8]. Some of the common topics on RA developments include wideband design using true time delay (TTD) techniques [12, 14, 20], multi-band RAs [22, 23, 31], and metasurface applications [72]. Most of these designs target the X, Ka, and Ku bands. While these bands are of interest for satellite applications, the telecommunication community has started to talk about exploring higher bands since the common ones are becoming increasingly congested [46, 47]. For this reason, the Q-band (37.5 GHz - 42.5 GHz) and V-band (47.2 GHz - 51.4 GHz) are becoming relevant. These higher bands are applicable for gateway links, and the increased bandwidth (BW) allows a higher capacity for sending and receiving large volumes of data between the stations. Compared to traditional reflectors, RAs provide solutions that are more compact, lightweight, easier to build, and easier to launch into space to use as downlink satellites. Nonetheless, few RA designs are found in these bands in the literature. For example, [13, 14] present designs in the Q-band, and [32] in the V-band. While each design explores different types of unit cells (UCs) (multi-resonant elements, TTD, and 3D printed), all the designs have an aperture less than 20 λ_0 by 20 λ_0, and target linear polarization. In contrast, satellite applications require circular polarization and a larger aperture to increase the gain and compensate the atmospheric losses. However, larger apertures usually lead to a narrow gain BW [5]. There are two ways to face this challenge. One is at the unit cell (UC) design stage. The most commonly used approach is TTD UC design. This methodology is based on designing UCs covering an unwrapped phase range larger than 360^o and providing a phase response that changes linearly with frequency in order to minimize beam squint effects away from the design frequency. This large coverage increases the phase compensation capability of the UCs in the RA. However, it often adds complexity to the UC design. Additionally, the resonant nature of the TTD UC increases the overall losses [12]. The second possibility are multi-faceted RAs. Differently from the TTD approach, the multi-faceted perspective concentrates on the aperture geometry. Hence, instead of a single planar face, a multi-faceted RA with several planar faces is used. Each face is in a different position emulating a parabolic dish. Although this approach involves losing the planarity of the design, the multiple faces can be used to facilitate the deployment of the antenna, and most importantly, the gain BW is

improved. This approach is rarely investigated in the literature. One example includes [2], which compares a planar RA with its equivalent three-faceted prototype. The RA aperture measures 18 λ_0 x 18 λ_0, covering the Ka band for dual-linear polarization. The results show a BW enhancement of 9% in the measurements compared to the planar RA. The same authors have explored a 5-faceted RA in simulations [42], and the results show a 2% increase in the BW compared to an equivalent three-faceted design. Following the same idea, another study shows the analysis of a 3 and 5-faceted RA using geometric optics analysis [43]. The results are similar to the ones in [42]. The only study presenting a prototype and measurements is [2]. Additionally, all these papers consider a multi-faceted geometry in one plane of the antenna. In contrast, other works have presented simulations of multi-faceted RAs imitating a paraboloidal reflector [44, 45]. However, they focus on beamforming instead of BW enhancement. Finally, preliminary results of this work were presented in [73]. This previous conference paper publication shows simulations of a seven-faceted RA and compares its phase distribution and radiation pattern with an equivalent planar version. Nonetheless, it does not present a methodology to minimize the phase errors, nor discusses the approach to adapt the antenna array theory for multi-faceted calculations. The work also lacks an analysis on gain and axial ratio BWs, and it does not provide any fabrication and measurement data.

This study presents a large, wideband, circular-polarized RA optimized for the V-band but maintaining a pencil beam in the Q-band too. The contributions of this work are:

- A methodology to design a multi-faceted RA to decrease phase errors at and away from the design frequency. Different from previous works, this study presents a parametric evaluation of the multi-faceted geometry to evaluate the phase error across a wide frequency band.
- Application of the array approach (AA) to study large, multi-faceted RAs. Large RAs require a lot of computational resources, especially if they have several faces. In contrast, AA is a fast methodology that provides a good estimation of RA performance. This methodology is well known from previous works [5]. Nonetheless, it is rarely applied for wideband analysis and multi-faceted RAs. This work explains how to define multiple faces and evaluate the directivity of the overall structure. The results are compared to simulations and measurements.
- Prove wide-band gain and axial ratio by prototyping and measuring the multi-faceted RA.

The rest of the chapter is organized as follows: Section 2.2 defines the geometry of the RA aperture, explains how to use the AA to evaluate it, and shows the UC to populate the

reflector. Next, Section 2.3 explains the methodology to evaluate the phase errors on the surface of the RA, and illustrates the impact of the multi-faceted aperture design choice on the radiation pattern. After that, Section 2.4 shows the experimental validations to finally discuss the measurements in Section 2.5. The chapter concludes in Section 2.6.

2.2 Aperture description and definitions for the array approach analysis

The RA has seven faces, one regular hexagon in the center, and six trapezoids (petals) (Fig. 2.1a). The aperture top view in Fig. 2.1b shows that the complete structure is a regular hexagon with a fixed edge-to-edge length (L_{RA}) equal to 36.23 cm ($\sim 60\lambda_0$ at 50 GHz). In contrast, the center face length (L_{hex}) and the petals' inclination (ψ_{petal}) can be set to optimize the performance (see Figs. 2.1b and 2.1c). The petals' length (L_{petal}) depend on L_{hex} and ψ_{petal}, and are defined by (2.1). All the petals have the same length and inclination.

Fig. 2.1c also illustrates the angle of incidence and reflection (θ_{in} and θ_{out}) with respect to the normal of the center hexagon ($\hat{n}$). In this study, the two variables equal 15^o (i.e. specular reflection). This choice leads to a symmetric phase distribution in the RA aperture. Consequently, a symmetric multi-faceted aperture can optimally compensate the phase wrapping. In contrast, having anomalous reflection (i.e. different θ_{in} and θ_{out}) causes an assymetric phase distribution in the aperture of the RA. In that case, symmetric multi-faceted RAs can compensate the phase wrapping although an assymetric configuration (petals with different size and inclination angles) might be necessary to optimally compensate the phase wrapping. This case is out of the scope of this thesis. However, the calculations presented are applicable for any multi-faceted aperture. Fig. 2.1d shows the aperture plane of the RA used in full-wave simulations and measurements.

Finally, the RA to horn distance R_{fd-ra} equals 81.9 cm. The feed antenna is a circular polarized, corrugated horn designed by MDA Space working from 37.5 GHz to 51.5 GHz. The selected distance guarantees an edge illumination in the RA of less than -10 dB for all the frequencies.

$$L_{petal} = \frac{L_{RA} - L_{hex}}{2 \times cos(\psi_{petal})} \tag{2.1}$$

2.2.1 Array Approach Analysis

This subsection explains the implementation of the AA theory in multi-faceted RAs. The AA is a well-known methodology to analyze RAs [5]. It calculates the radiation pattern based on the antenna array theory. Although it neglects the field polarization, and mutual coupling

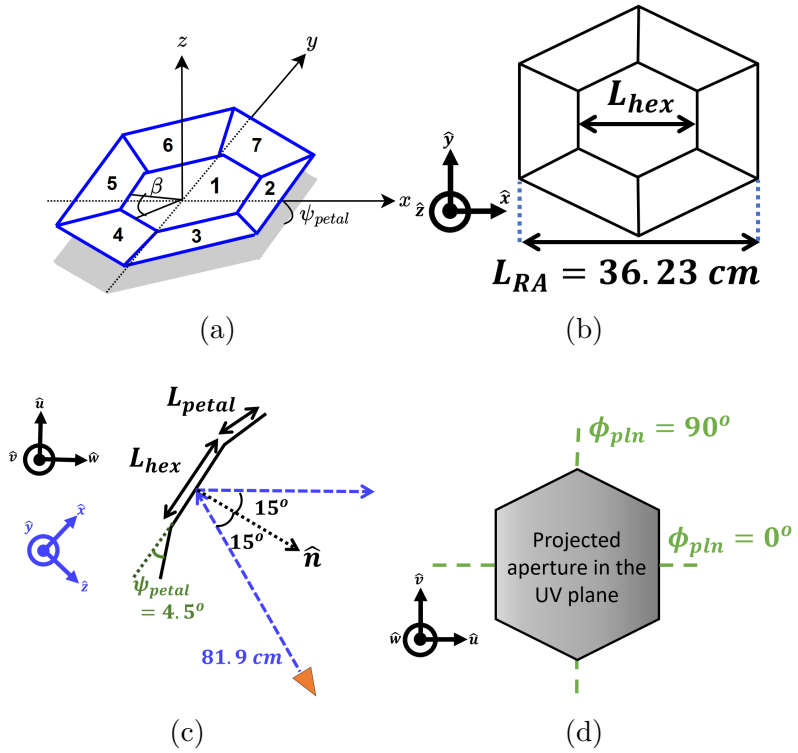

Figure 2.1 Multi-faceted RA, (a) Isometric view, (b) top view, (c) side view including the horn antenna in the bottom-right corner, and (d) UV plane of the RA.

effects, it accurately estimates the radiation pattern and the directivity.

Definition of the faces

Classical RAs define the UC coordinates in the XY plane. However, the multi-faceted configuration in this chapter requires several faces that lay in different planes. Fig. 2.1a shows that only face 1 lays in the XY plane. In contrast, the petals are inclined in different planes and four steps are required to define their coordinates. Fig. 2.2 illustrates the first three. First, one defines the petals' coordinates in the XY plane, then one rotates the face with respect to the z axis, and finally, one rotates the face in the elevation plane. The rotation matrix representing this process is shown in (2.2), where β and ψ_{pet} represent the z and elevation rotation angles. The fourth step is translating the surface position to place them at the respective face 1 edges. The translation coordinates are defined as $\Delta x_{hex} = L_{hex}/(2cos\beta)$ and $\Delta y_{hex} = L_{hex}/(2sin\beta)$, and β equals $60^o \times (f-1)$ with $f = 2, 3, ..., 7$. The four steps are summarized in (2.3).

$$Rot = \begin{pmatrix} cos\psi_{pet}\, cos\beta & sin\beta & sin\psi_{pet}\, cos\beta \\ -cos\psi_{pet}\, sin\beta & cos\beta & -sin\psi_{pet}\, sin\beta \\ -sin\psi_{pet} & 0 & cos\psi_{pet} \end{pmatrix}_{step_{2-3}} \tag{2.2}$$

$$\begin{pmatrix} x_{m,n} \\ y_{m,n} \\ z_{m,n} \end{pmatrix}_{f=2,\ldots,7} = Rot \cdot \begin{pmatrix} x_{m,n} \\ y_{m,n} \\ 0 \end{pmatrix}_{step_1} + \begin{pmatrix} \Delta x_{hex} \\ \Delta y_{hex} \\ 0 \end{pmatrix}_{step_4} \tag{2.3}$$

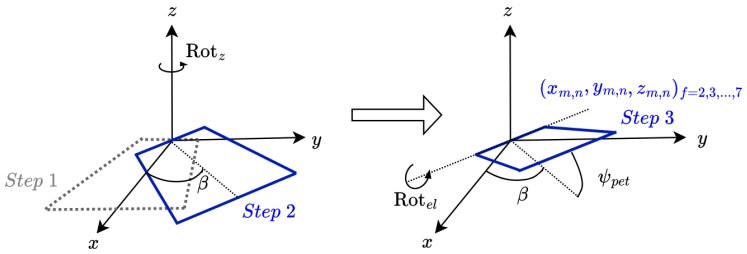

Figure 2.2 Definition of the coordinates of the petals.

Radiation pattern and directivity

Equation (2.4) estimates the radiation pattern using the AA [5]. The subscripts m, n refer to each UC, $I_{m,n}$ stands for the horn illumination, $R_{m,n}$ is the distance from the horn antenna's phase center to each element, and $\phi_{m,n}^{RA}$ is the phase distribution on the surface of the RA (2.5). Note that the phase distribution depends on the wavenumber k_0, the UCs' coordinates, and the reference phase ϕ_{ref}. All these parameters are illustrated in Fig. 2.3. Another remark on (2.4) is a third summation term to add the contribution of each RA face.

$$E(\theta, \varphi) = \sum_{f=1}^{7} \sum_{m=1}^{M_f} \sum_{n=1}^{N_f} \frac{I_{m,n}}{R_{m,n}} e^{-j\phi_{RA}} \tag{2.4}$$

$$\begin{aligned} \phi_{m,n}^{RA} = k_0[R_{m,n} - sin\theta_{out}\,(x_{m,n}cos\varphi_{out} + y_{m,n}sin\varphi_{out}) \\ + z_{m,n}cos\theta_{out}] + \phi_{ref} \end{aligned} \tag{2.5}$$

The AA allows estimating the RA directivity using (2.6) [5]. This equation uses the electric

field calculated in (2.4). However, the denominator requires numerical evaluation. This work uses the technique explained in [74], which is implemented using (2.7). In this equation $E_{i,j} = E(\theta_i, \varphi_j)$, $\theta_i = i\pi/M_\theta$, and $\varphi_j = j2\pi/N_\varphi$. Note that M_θ and N_φ are the total number of infinitesimal discretizations to evaluate $denD$, and $S_{\theta_i} = Sin(\theta_i)$.

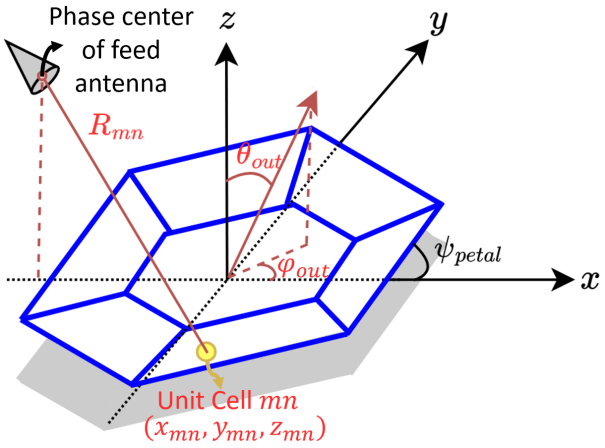

Figure 2.3 Parameters of the multi-faceted RA.

$$D(\theta,\varphi) = \frac{4\pi\left|E(\theta,\varphi)\right|^2}{\int_0^{2\pi}\int_0^{\pi/2}\left|E(\theta_{int},\varphi_{int})\right|^2 sin\theta_{int}d\theta_{int}d\varphi_{int}} = \frac{4\pi\left|E(\theta,\varphi)\right|^2}{denD} \tag{2.6}$$

$$denD = \frac{2\pi}{M_\theta}\frac{\pi}{2N_\varphi}\sum_{i=1}^{M_\theta}\sum_{j=1}^{N_\varphi}\left|E_{i,j}\right|^2 sin\theta_i = \frac{\pi^2}{M_\theta N_\varphi}\cdot$$
$$\sum\left[\begin{pmatrix} |E_{1,1}|^2 & |E_{2,1}|^2 & \cdots & |E_{M_\theta,1}|^2 \\ |E_{1,2}|^2 & |E_{2,2}|^2 & \cdots & |E_{M_\theta,2}|^2 \\ \vdots & \vdots & \ddots & \vdots \\ \left|E_{1,N_\varphi}\right|^2 & \left|E_{2,N_\varphi}\right|^2 & \cdots & \left|E_{M_\theta,N_\varphi}\right|^2 \end{pmatrix}\begin{pmatrix} S_{\theta_1} \\ S_{\theta_2} \\ \vdots \\ S_{\theta_{M_\theta}} \end{pmatrix}\right] \tag{2.7}$$

2.2.2 Unit Cell

The goal of the design is to achieve a pencil beam in both the Q and V bands while maximizing the antenna gain. The proposed UC operates in a single band, allowing optimization for only one band. The choice of which band to optimize is based on the two key figures of merit for

satellite data links: the equivalent isotropic radiated power (EIRP) for transmitting in the Q-band, and the gain-to-noise temperature (G/T) for receiving in the V-band. In a downlink satellite scenario, the G/T is constrained by the performance of the low-noise amplifier and can only be improved by increasing the antenna gain. In contrast, the EIRP is influenced by both antenna gain and radiated power, which can be easily boosted with a power amplifier to compensate the gain. Therefore, optimizing the V-band, which relies solely on the RA's gain, is the more effective strategy. The geometry of the UC is a dual-layer circular patch (shown in Fig. 2.4) with a total thickness of 0.575 mm ($0.095\lambda_0$). The thickness of the substrates corresponds to the standard values provided by the supplier. The circular patches are chosen to keep the simplicity of the UC, and the radius of the top patch is set to be a function of the bottom patch radius ($R_{top} = 0.77R_{bot}$). The relation of the two layers allow to simplify the optimization of the UC using a single parameter to enlarge the phase coverage while keeping smooth curves that minimize the risk of errors caused by fabrication tolerances. The analysis of the reflection performance was run in TICRA-QUPES [75]. An illustration of the simulation setup is shown in Fig. 2.5a. The UC is set to be used in a square lattice with a periodicity of 2.9 mm ($0.48\lambda_0$ at 50 GHz).

The main goal of the design is to maximize the phase coverage in the V-band. Nonetheless, the results show a phase coverage above 300^o up to 37.5 GHz, which allows evaluating the RA in the Q-band as well. Fig. 2.5 shows the reflection response of the UC at normal incidence. Fig. 2.5b shows that the phase coverage in the V-band is between 400^o and 500^o, and between 300^o and 320^o in the Q-band. On the other hand, the reflection magnitude shows losses lower than -0.5 dB (Fig. 2.5c) in all the cases. This performance is stable even for large angles of incidence for both, transverse electric (TE) and transverse magnetic (TM) waves, as shown in Fig. 2.6. These metrics prove that the UC's performance is optimal for the V-band and acceptable for the Q-band.

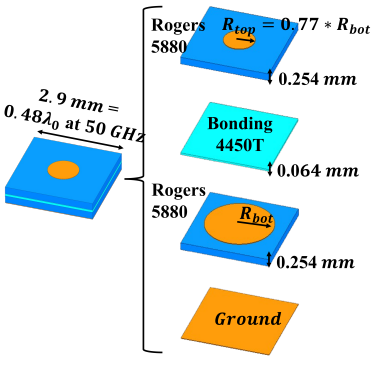

Figure 2.4 Exploded view of the Unit Cell.

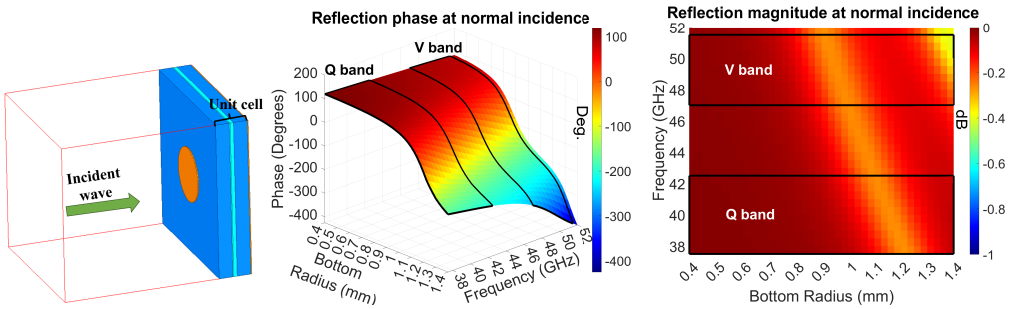

(a) (b) (c)

Figure 2.5 Reflection coefficient of the proposed UC, (a) simulation setup, (b) phase, and (c) magnitude.

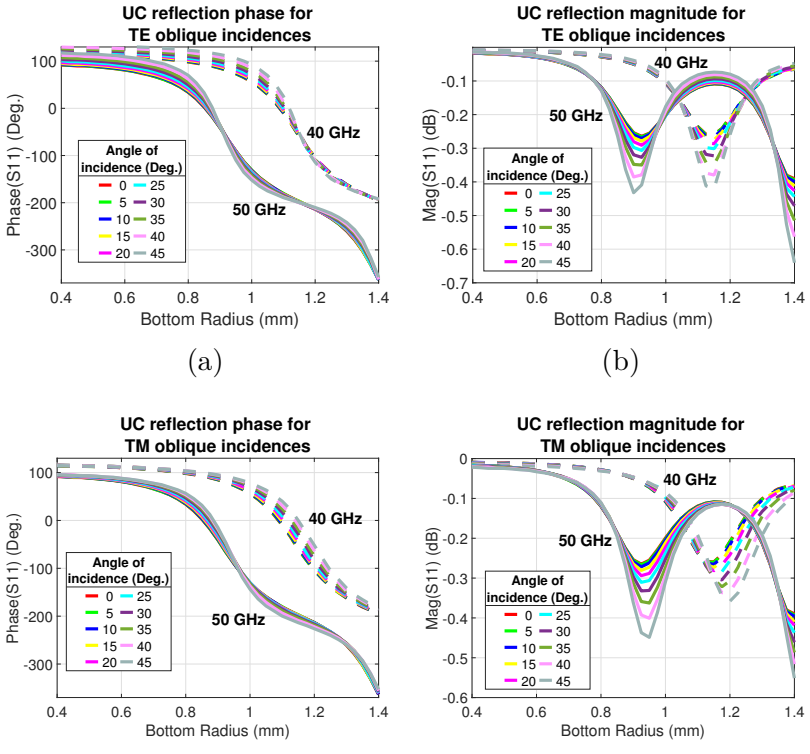

(a) (b) (c) (d)

Figure 2.6 Unit Cell Reflection coefficient for oblique incidences at 40 GHz and 50 GHz. TE wave (a) phase, and (b) magnitude, and TM wave (c) phase, and (d) magnitude.

2.3 Multi-faceted impact on the reflectarray performance

2.3.1 Phase Error

The phase distribution is defined by (2.5). Fig. 2.7 shows the phase distribution at 50 GHz for three cases of the defined multi-faceted aperture. The size of the center face is defined as a constant (L_{hex} = 14.9 cm) to facilitate the analysis. The figures illustrate how changing ψ_{petals} impacts the phase wrapping. Indeed, the planar RA (Fig. 2.7a) and the RA with inclination angle $\psi_{petals} = 10^o$ have several phase wrappings. This effect is one of the main factors limiting the BW of the RA because it increases the phase errors away from the center frequency [5]. Oppositely, when $\psi_{petals} = 4.5^o$, the phase wrapping only happens in the petals' corners. The number of phase wrappings depends on the closeness of the RA aperture to the ideal parabolic reflector as illustrates Fig. 2.8. This example shows that a planar RA or a multi-faceted RA with large petals' inclination (e.g. 10^o) is far from the conformal reflector. Consequently, these configurations require large phase compensation leading to various phase wrappings. On the other side, a proper petal's inclination is closer to the conformal reflector and requires less phase correction. Consequently, the number of phase wrappings decreases as happens for the petals' inclination equal to 4.5^o. It is worth to say that the symmetry of the proposed multi-faceted aperture does not allow to perfectly approach the parabolic reflector. However, the petals' inclination $\psi_{petals} = 4.5^o$ minimizes the phase wrapping, and a parametric study based on the absolute root mean square (RMS) phase error (2.8) and the weighted RMS phase error (2.9) confirms the minimization of the phase error. These equations calculate the difference between the ideal phase distribution profile ($\phi^{RA}_{m,n}$) and the one achievable using the proposed UC ($\phi^{UC}_{m,n}$) for the total number of UCs (T_{uc}). To select $\phi^{UC}_{m,n}$, the oblique incidence of the UC simulations is considered. Moreover, the weighted RMS phase error considers the normalized feed illumination on each UC ($I_{m,n}$). Figs. 2.9a and 2.9b show the results of these calculations. There is no error at 50 GHz, as it is the frequency of design. For any other frequency, the error depends on the petals' inclination. For example, Fig. 2.9a shows that in the planar case ($\psi_{petals} = 0^o$), the absolute phase error increases to 75^o at 52 GHz, and it becomes more than 100^o below 42.5 GHz. A similar behavior happens when $\psi_{petals} = 10^o$. However, the figures show an error minimization within the inclination angles $4^o \leq \psi_{petals} \leq 6.5^o$. In this region, the absolute phase error is less than 66^o.

Fig. 2.9b shows that the weighted error in the V-band is below 50^o on average, and it is mostly uniform for any multi-faceted configuration. This means that the petals' inclination do not have a significant impact on the radiation patterns in the higher band. However, as the frequency decreases, the weighted error increases. Indeed, in the Q-band, the weighted error

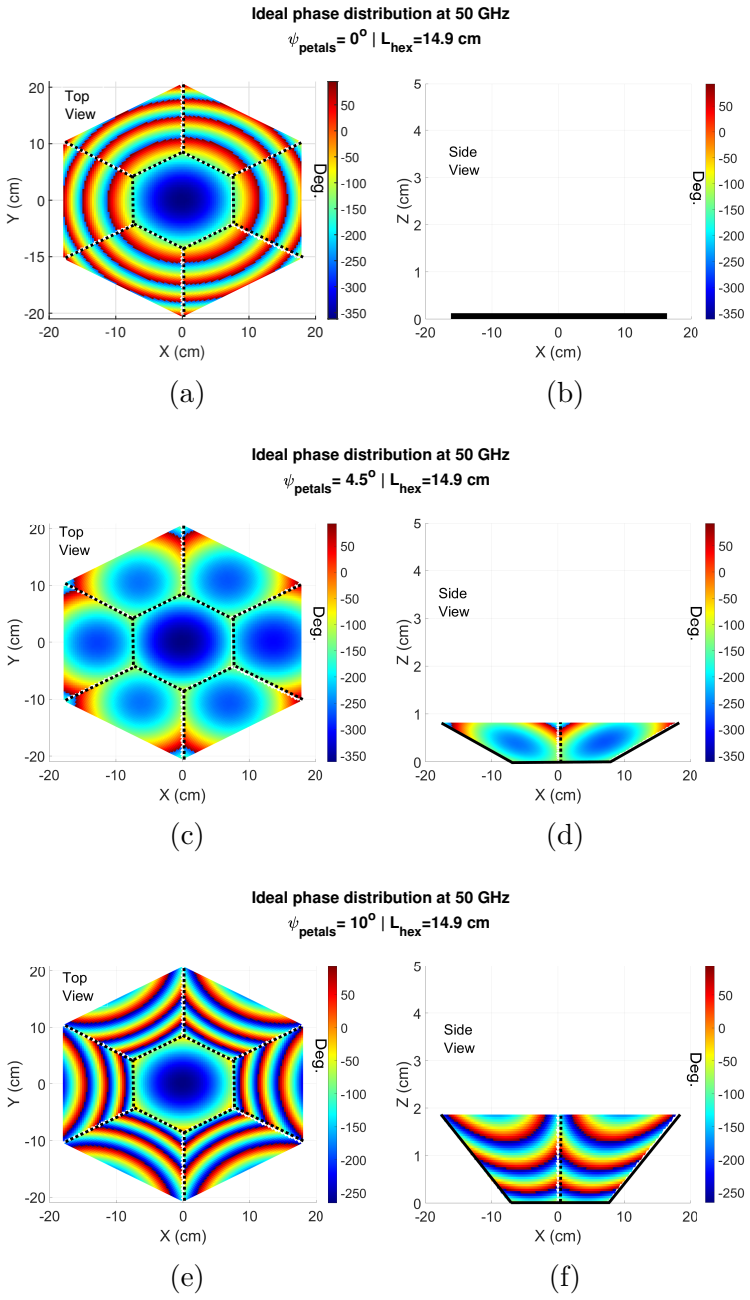

Figure 2.7 Phase distribution at 50 GHz for various petals' inclinations, (a) $\psi_{petals} = 0^o$, top view, (b) $\psi_{petals} = 0^o$, side view, (c) $\psi_{petals} = 4.5^o$, top view, (d) $\psi_{petals} = 4.5^o$, side view, (e) $\psi_{petals} = 10^o$, top view, (f) $\psi_{petals} = 10^o$, side view

is above 80^o for petals inclinations out of the region of minimum error ($4^o \leq \psi_{petals} \leq 6.5^o$). Hence, to achieve a RA with good performance at all frequencies of interest, an inclination angle between 4^o and 6.5^o is optimal. While the minimum weighted and absolute errors happen at 5.5^o, this work presents a RA with $\psi_{petals} = 4.5^o$, which is also within the valley.

The reason of this choice is that the initial RA optimization considered a large step variation for the ψ_{petals} values, skipping most of the points of the valley, and showing 4.5^o as the best option. The next section shows that even though this angle is not the optimal one, this configuration still maintains a good performance.

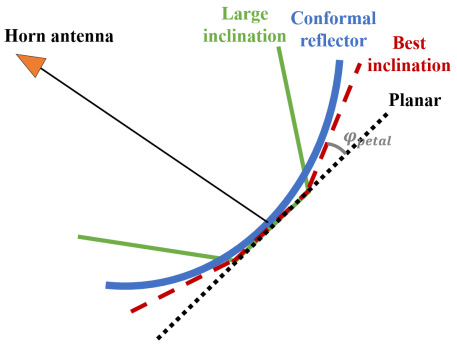

Figure 2.8 Aperture comparison of a conformal reflector with multi-faceted RAs with different petals' inclinations.

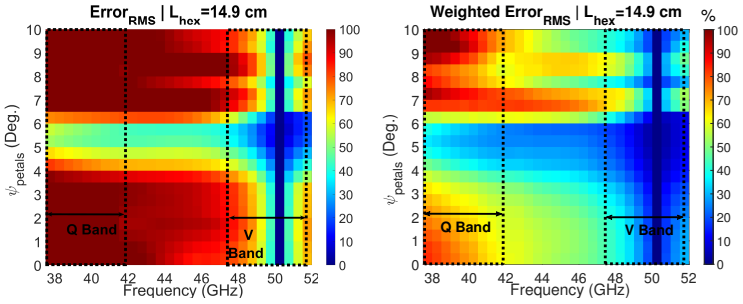

(a) (b)

Figure 2.9 (a) Absolute phase error, (b) Weighted phase error

$$Error_{rms} = \sqrt{\frac{1}{T_{uc}} \sum_{f=1}^{7} \sum_{m=1}^{M_f} \sum_{n=1}^{N_f} (\phi_{m,n}^{RA} - \phi_{m,n}^{UC})^2} \tag{2.8}$$

$$Werror_{rms} = \sqrt{\frac{1}{T_{uc}} \sum_{f=1}^{7} \sum_{m=1}^{M_f} \sum_{n=1}^{N_f} [I_{m,n}(\phi_{m,n}^{RA} - \phi_{m,n}^{UC})]^2} \tag{2.9}$$

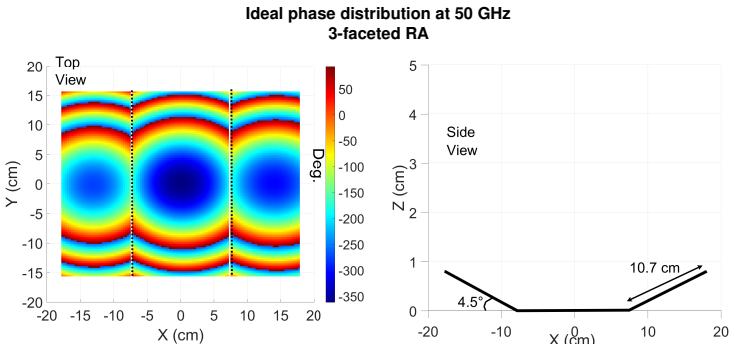

(a) (b)

Figure 2.10 Phase distribution at 50 GHz for a three-faceted RA with inclined faces to 4.5^o, (a) top view, (b) side view

2.3.2 Radiation Pattern

The AA allows comparing the radiation pattern of the apertures shown in Fig. 2.7 and of a three-faceted RA. The latter configuration is illustrated in Fig. 2.10, whose aperture area equals that of the seven-faceted RA, and the inclination angle equals $\psi_{petals} = 4.5^o$. Fig. 2.12 shows the radiation patterns for various frequencies and inclination angles, wherein all patterns are normalized such that the maximum of the radiation pattern for $\psi_{petals} = 4.5^o$ RA is at 0 dB. The phase distribution of each case is defined according to (2.5) for the frequency of design (i.e. 50 GHz). For any other frequency, the phase distribution follows the dispersive performance of the chosen UCs. All cases are illustrated in Fig. 2.7 and Fig. 2.10 at 50 GHz. The calculations also consider the simulated reflection response of the UC with respect to the frequency. The results at 50 GHz (Fig. 2.12b) are very similar for all the RAs. The patterns at 51.4 GHz and 47.2 GHz (Figs. 2.12a and 2.12c) only show slight variations, notably a difference of less than 1 dB in the main beam at 47.2 GHz. Oppositely, at the edges of the Q-band (42.5 GHz and 37.5 GHz), the patterns change significantly. Fig. 2.12d shows that the sidelobe levels (SLLs) remain close in all the cases, but the main lobe decreases by 2.4 dB for the three-faceted RA, 4.7 dB for the planar RA, and 7.1 dB for the RA with $\psi_{petals} = 10^o$. The degradation is worse at 37.5 GHz as the main beams of the planar and RA with $\psi_{petals} = 10^o$ vanish, and the main beam of the three-faceted RA decreases by 7.4 dB. These results confirm the performance improvement of the seven-faceted RA with $\psi_{petals} = 4.5^o$.

2.3.3 Gain Bandwidth

The final analysis compares the gain of the seven-faceted RA with $\psi_{petals} = 4.5°$ (Fig. 2.7c) to the three-faceted RA with the same petals' inclination angle (Fig. 2.10a), and the planar RA (Fig. 2.7a). This study was conducted using full-wave simulations in TICRA-QUPES. Each design has a gain of 43.5 dB at 50 GHz. Fig. 2.11a illustrates the gain as a function of frequency for each design, and Table 2.1 lists the 1- and 3-dB gain BWs for all designs. Both the seven- and three-faceted RAs show a modest 0.5% enhancement in the 1-dB gain BW compared to the planar RA. For the 3-dB gain BW, the seven-faceted RA shows a 3% improvement compared to the three-faceted RA and 5% compared to the planar RA.

In addition to the bandwidth increase, Fig. 2.11a shows that the gain decreases more gradually for the seven-faceted RA. This observation aligns with the pattern degradations seen in Figs. 2.12d and 2.12e, as well as the radiation patterns at 40 GHz obtained from QUPES (shown in Fig. 2.11b). This last plot also reveals that the half-power beamwidth and sidelobe levels of the three-faceted RA increase significantly in the $\phi_{pln} = 90°$ plane at lower frequencies. These pattern degradations occur due to the effect of the phase wrappings, explaining the faster gain decline of the three-faceted RA. In contrast, the seven-faceted RA maintains a pencil-beam pattern throughout the analyzed frequency range. The simulation results demonstrate that the seven-faceted RA enhances both the bandwidth and radiation pattern characteristics compared to the other two configurations.

Table 2.1 Gain BW comparison

	Gain BW between 37.5 GHz - 51.5 GHz		
	Seven-faceted	**Three-faceted**	**Planar**
1-dB	10.4%	10.4%	9.1%
3-dB	20.3%	17.3%	15.0%

2.4 Experimental validation

The fabricated prototype of the RA is shown in Fig. 2.13a. Each surface has been fabricated separately, and all pieces have been assembled together in a plastic 3D-printed base that guarantees the specific petals' angle inclination. The 3D- printed base is shown in Fig. 2.13b. The RA is attached to a metallic structure that also holds the circularly polarized horn antenna at the distance defined in Section 2.2. The horn antenna is corrugated and circular polarized, with a BW from 37.5 GHz to 51.4 GHz. This horn antenna was designed and provided by MDA Space. The selected focal distance guarantees an edge illumination

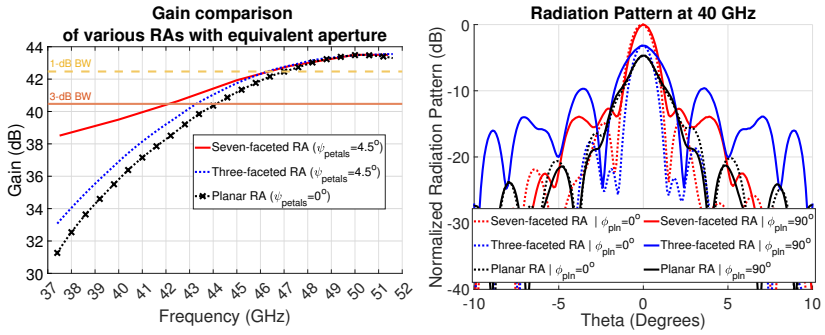

(a) (b)

Figure 2.11 Comparison of the seven-faceted, three-faceted, and planar RAs (a) Gain, and (b) radiation pattern at 40 GHz.

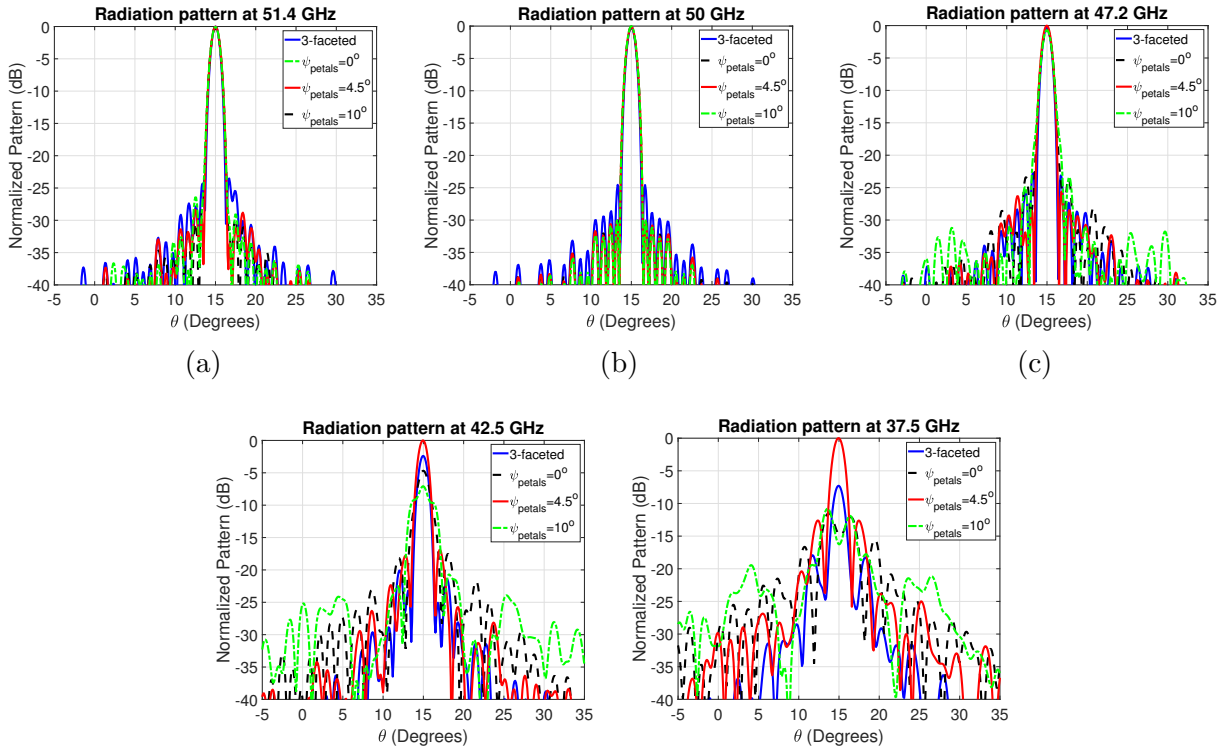

(a) (b) (c)

(d) (e)

Figure 2.12 Normalized radiation pattern for $\psi_{petals} = 0^o$ (planar) , 4.5^o 10^o at (a) 51.4 GHz, (b) 50 GHz, (c) 47.2 GHz, (d) 42.5 GHz, and (e) 37.5 GHz.

lower than -10 dB at all frequencies.

The RA was tested in the Compact Antenna Test Range (CATR) chamber of the Poly-Grames research center of Polytechnique Montreal, and the measurement setup is depicted in Fig.

2.13c. This CATR allows measuring the far field radiation pattern in any plane of interest, and calculating the RA gain using reference measurements of a standard-gain horn antenna. Nonetheless, the laboratory only disposes of linear polarized sources at these frequencies. Thereby, the experiment requires two sets of measurements using orthogonal polarizations. The two sets of measurement data are then post-processed to calculate circularly polarized results [76]. Another constraint is the mixer BW in the CATR system, which covers the range of 40 GHz to 60 GHz. While it it is possible to push the measurement frequencies a few GHz below 40 GHz, we cannot cover the complete Q-band. This constraint limits the gain calculation below 40 GHz. Nonetheless, the normalized far field radiation pattern can be measured to give an insight into the performance of the RA.

All the measurements are compared to the AA calculations from (2.4), and to the simulations from TICRA-QUPES. This tool is specialized in full-wave analysis of quasi-periodic structures using the method of moments [75].

2.4.1 Radiation Pattern measurements

Fig. 2.14 shows the normalized radiation patterns at the Q and V bands' center frequencies and near their limits. All the figures show the Co-polarization (RHCP) and cross-polarization (LHCP) patterns. It is worth mentioning that the AA neglects the calculation of cross-polarization. Thereby, only the Co-polarization is depicted for this approach.

The results for the higher frequencies are presented in Figs. 2.14a-2.14c. It must be noted that the angular (i.e. θ) range in these plots has been narrowed down so that the details of the main beam and the SLLs are well visible. Additionally, Table 2.2 summarizes the main antenna parameters. It can be observed that the QUPES results and the AA calculations match well. Also, the measured main beam points to the expected direction at the lowest frequency and has beam squint of 0.5^o and 0.4^o at 50 GHz and 51.6 GHz. The measured half-power beamwidths (HPBWs) are 0.1^o larger than the theoretical ones. Overall, the measured response is in agreement with the theoretical calculations and simulations. However, the SLL and the cross-polarization levels have discrepancies. The measured SLLs are between 5 and 8 dB above the ones predicted by the theory. Nonetheless, the values remain below -14 dB in all the cases. The cross-polarizations are also higher in the measurements. Nonetheless, the axial ratio (AR) remains below 0.96 dB at all frequencies.

The measurement results at the frequencies located in the lower band are presented in Figs. 2.14d - 2.14f. As for the higher frequencies, the main lobes match well in the three cases. Fig. 2.15 displays the measured radiation patterns and the simulated counterparts from QUPES for the $\phi_{pln} = 0°$, 45°, and 90° planes at 50 GHz and 40 GHz. The results are consistent at

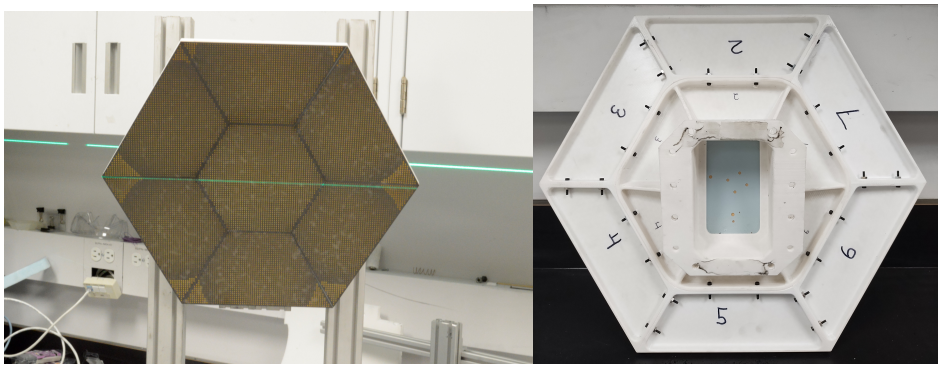

(a) (b)

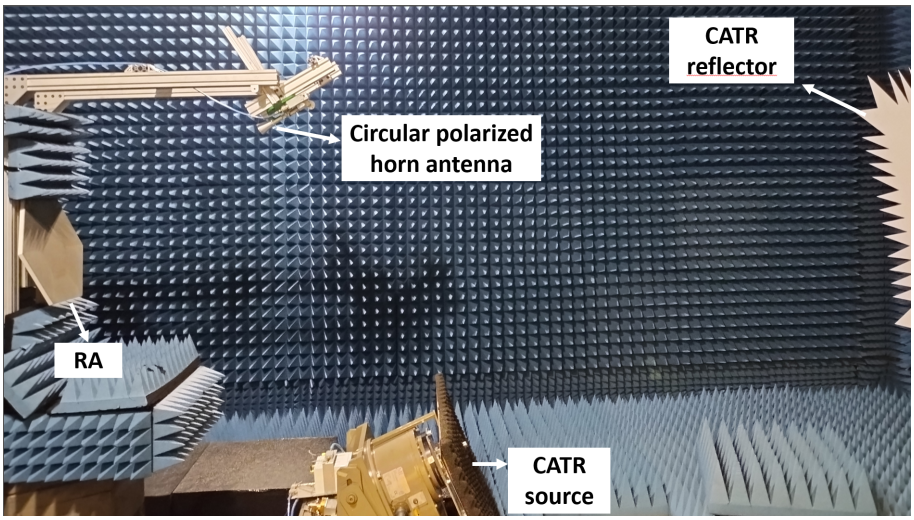

(c)

Figure 2.13 Photos of the measurement setup, (a) frontside of the multi-faceted RA, (b) backside of the multi-faceted RA, and (c) complete measurement setup in the CATR.

both frequencies, demonstrating that the pencil beam is maintained in each case. Similarly, cross-polarization at broadside remains consistent across all planes. However, the SLLs in the $\phi_{pln} = 90°$ plane are worse than those in the $\phi_{pln} = 0°$ plane. Table 2.2 summarizes these findings across all frequencies, and shows that the SLLs remain below -12.9 dB in all measurements for the $\phi_{pln} = 90°$ plane, which is higher than the predictions by the simulations. The discrepancy between the simulated and measured SLLs is further discussed in Section 2.4.3.

In addition to the SLLs, Table 2.2 highlights the key parameters of the RA and compares the measurements with the predictions made by QUPES and the theoretical AA calculations. Overall, the HPBW predictions are consistent in all methods. The SLLs from the measurements differ by no more than 1.2 dB from the QUPES simulations in the $\phi_{pln} = 0°$ plane.

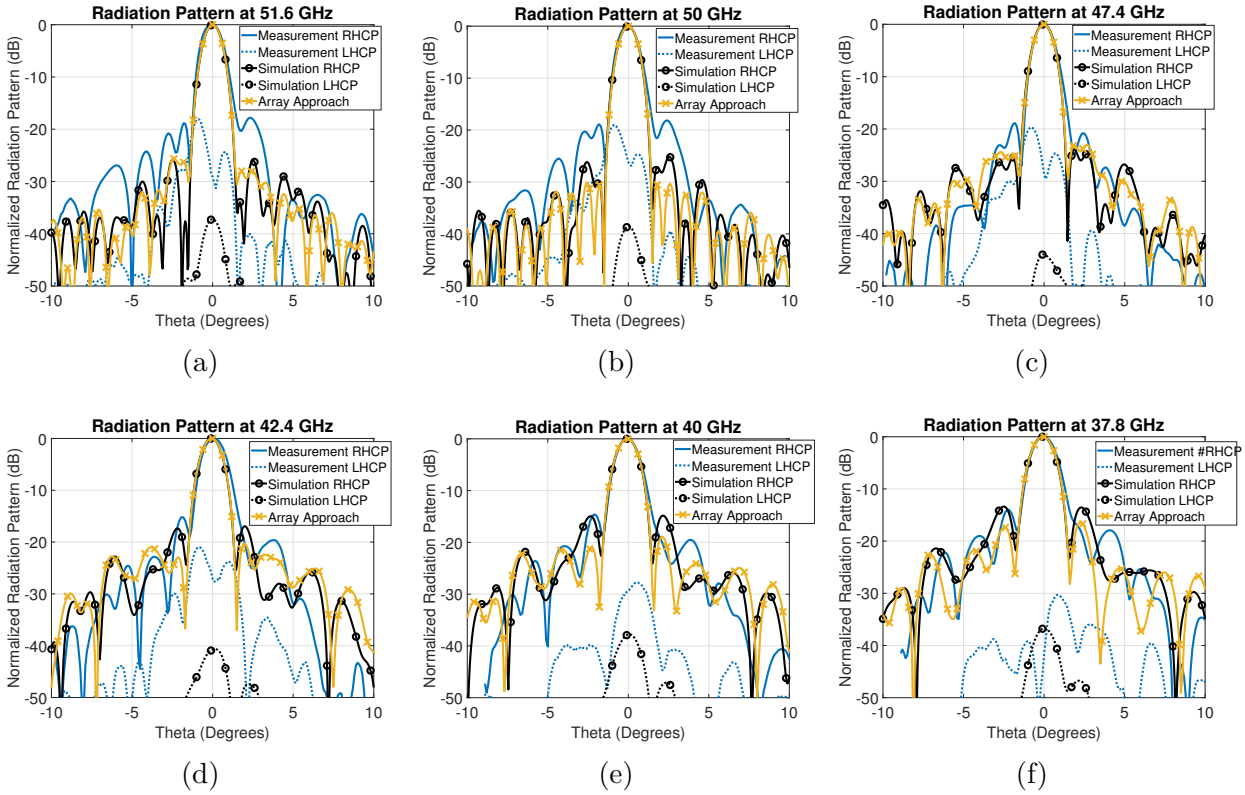

Figure 2.14 Radiation pattern in the plane $\phi_{pln} = 0^o$ (a) 51.6 GHz, (b) 50 GHz, (c) 47.4 GHz, (d) 42.4 GHz, (e) 40 GHz, and (f) 37.8 GHz

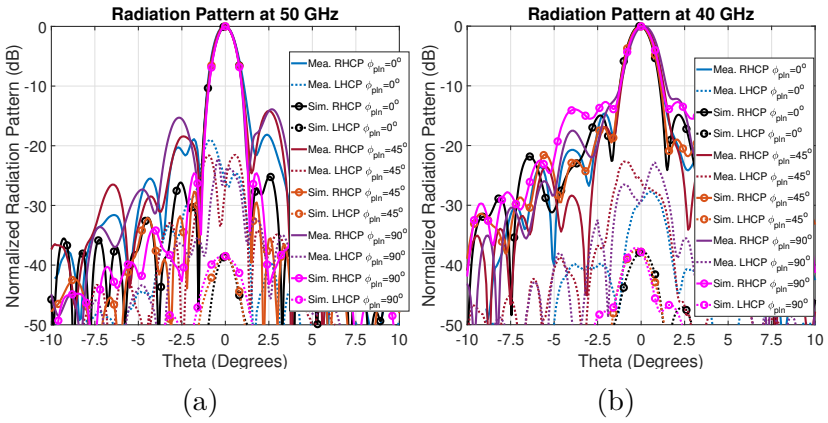

Figure 2.15 Measurement and simulations of the radiation pattern in the planes $\phi_{pln} = 0^o$, 45^o, and 90^o at (a) 50 GHz, and (b) 40 GHz.

The AR remains below 0.76 dB, indicating minimal degradation of circular polarization by the RA. Further details on the gain and AR of the antenna are provided in the following section.

Table 2.2 comparison of the simulations, array approach calculations and measurements from raw data of the Reflectarray

		HPBW (^{o})	**SLL (dB)** ϕ_{pln} 0^o	**SLL (dB)** ϕ_{pln} 90^o	**AR (dB)**	**Gain (dB)**	**Ap. eff. (%)**
37.8 GHz	**Sim.**	1.4	-13.4	-12.0	0.25	38.5	36.2
	AA	1.4	-16.4	-	-	39.8	48.5
	Meas.	1.5	-14	-12.9	0.14	-	-
40 GHz	**Sim.**	1.35	-14.9	-12.9	0.23	39.5	40.7
	AA	1.35	-18.9	-	-	40.7	54.3
	Meas.	1.4	-14.6	-12.2	0.58	39.2	38.0
42.4 GHz	**Sim.**	1.3	-17.4	-14.0	0.16	40.6	46.7
	AA	1.3	-20.4	-	-	41.7	60.9
	Meas.	1.4	-15.2	-13.3	0.72	39.3	34.6
47.4 GHz	**Sim.**	1.15	-23.9	-21.2	0.11	43.2	68.0
	AA	1.15	-23.1	-	-	43.6	75.3
	Meas.	1.2	-19	-18.2	0.64	43.2	68.0
50 GHz	**Sim.**	1.1	-26.2	-24.6	0.21	43.5	65.5
	AA	1.1	-30.6	-	-	44.1	76.1
	Meas.	1.2	-18.2	-13.9	0.96	40.7	34.4
51.6 GHz	**Sim.**	1.1	-25.9	-27.1	0.24	43.5	61.5
	AA	1.1	-25.7	-	-	44.1	71.3
	Meas.	1.3	-17.8	-13.1	0.67	39.5	24.5

2.4.2 Gain and Axial Ratio

Fig. 2.16 presents the gain and axial ratio (AR) obtained from measurement data and QUPES simulations, as well as gain calculations derived from the AA method. The AA calculations incorporate the directivity (2.6) while considering the material loss, spillover and illumination efficiencies, and insertion loss in the feed horn antenna. This insertion loss is about 0.2 dB, and arises from the transition between the horn antenna and the polarizer waveguide, which allows the excitation of orthogonal polarizations. Fig. 2.16a shows the measured gain data obtained through normalization of the measured far-field with respect to that of the standard horn antenna. Below 40 GHz, the curve has an abnormal drop and gain above the simulations. These results are due to the BW limitation of the CATR mixer. Above 40 GHz, the measurements have various ripples, which is usual in mm-wave measurements (e.g. [2]). The measured gain is close to the simulations. This agreement is more clear after averaging the raw data, as shows Fig. 2.16b. This averaging approach is based on a regression method to establish the 3rd-degree polynomial that best fits the raw data from 38 GHz to 51.6 GHz, which is then used to estimate the gain at the remaining frequencies. Fig. 2.16b

shows that the AA calculations, simulations, and averaged measurement curves follow nearly the same trend. However, the gain calculated from the AA is between 0.3 and 1.0 dB above the simulations. This overestimation is usual in the AA [5]. Overall, the measured gain follows the theoretical curve up to 47.8 GHz with an average drop of 1 dB with respect to the QUPES simulation data. Then, the gain drops until it reaches a difference of 3.5 dB at 51.5 GHz. The reasons for this discrepancy is discussed in the next section. The measurements show a maximum gain of 41.8 dB at 47.6 GHz and a 1-dB gain BW of 13.4% (44 GHz to 50.4 GHz). The results also show that the gain remains above 38.8 dB from 39.8 GHz to 51.5 GHz, indicating a 3-dB gain BW of 25.6%. The aperture efficiency in the 1-dB BW remains between 35% and 50%, and the minimum aperture efficiency equals 24.5% at 51.6 GHz. This efficiency considers the scan loss (0.15 dB), which takes the effective aperture area of the RA for the off-broadside radiation at $\theta_{out} = 15^o$.

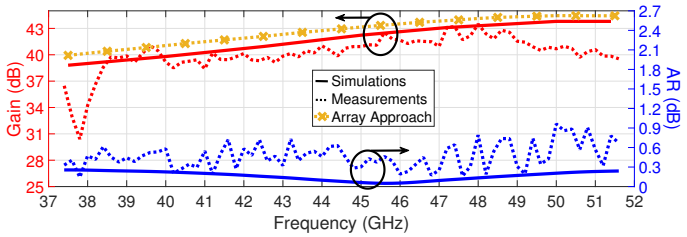

(a)

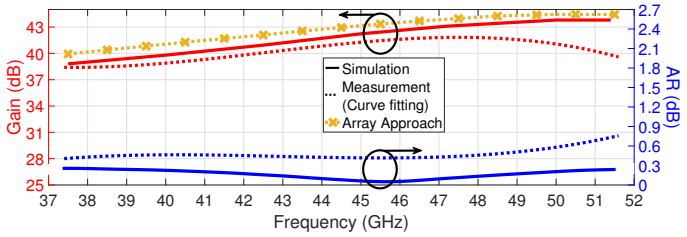

(b)

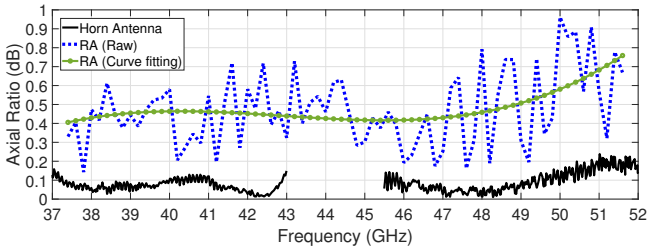

(c)

Figure 2.16 Gain and AR from simulations, AA and measurements (a) from raw data, (b) averaging the raw data, and (c) AR comparison of the horn antenna and the RA.

Fig. 2.16c presents a comparison between the AR of the horn antenna (data provided) and the RA. The RA introduces depolarization of approximately 0.35 dB in the Q-band and 0.4 dB in the V-band. The measured AR is around 0.5 dB higher than the simulated values. Nonetheless, the low depolarization levels and the AR below 1 dB across the frequency range demonstrate that the RA performs effectively for circular polarization, achieving a 1-dB AR bandwidth of 31.4%.

2.4.3 Analysis of the discrepancies

The two main factors affecting the measured RA response are the limitations of the CATR and the fabrication errors. The CATR at the Poly-Grames Research Center of Polytechnique de Montréal has a quiet zone of approximately 30 cm, which is smaller than the aperture of the RA. Additionally, its reflector is slightly misaligned with the platform where the antenna under test is attached. This misalignment has a significant impact when measuring the gain for antennas with pencil-beam patterns. To demonstrate this, Figs. 2.17a and 2.17c show the normalized radiation patterns from AA calculations in the UV plane at 50 GHz and 40 GHz. Each plot includes two lines representing the measurement plane (main plane) and a misaligned plane. The misaligned plane is randomly chosen at U=0.007. Projecting the RA aperture to the UV plane (see Figs. 2.1c and 2.1d), and considering that the limits of UV plane match with the edges of the projected RA aperture, the physical misalignment in the RA corresponds to 2.5 mm. Figs. 2.17b and 2.17d show the corresponding radiation patterns. It is observed that this small misalignment causes SLLs at 50 GHz to increase by 4 dB, while at 40 GHz they remain mostly unchanged. This behavior is consistent with the results shown in Fig. 2.14. A similar effect is seen in the main beam, which drops by 1.5 dB at 50 GHz but only by 1 dB at 40 GHz.

Some of the effects of fabrication errors are addressed in [2], which has shown that undesired gaps and errors in the inclination of the petals cause the maximum gain to shift to a lower frequency. An inspection of the proposed RA prototype in this work revealed errors in the petal inclination between 0.1° and 0.5°, as well as gaps in some surfaces of up to 1 mm. This contributes to the shift of the maximum gain to 47.6 GHz. However, the factor that most affects the RA's performance is the tolerance of the UCs. Fig. 2.18 illustrates how the gain curve degrades when an error is introduced in the UCs radius. These curves are obtained from full-wave simulations in TICRA-QUPES. Three levels of fabrication tolerance were studied by introducing a random, normally distributed error in the bottom radius of the UCs throughout the surface of the RA. The error ranges are ±0.20 mm, ±0.25 mm, and ±0.3 mm. The radius of the top layer is also affected, as it is bound to the bottom radius by

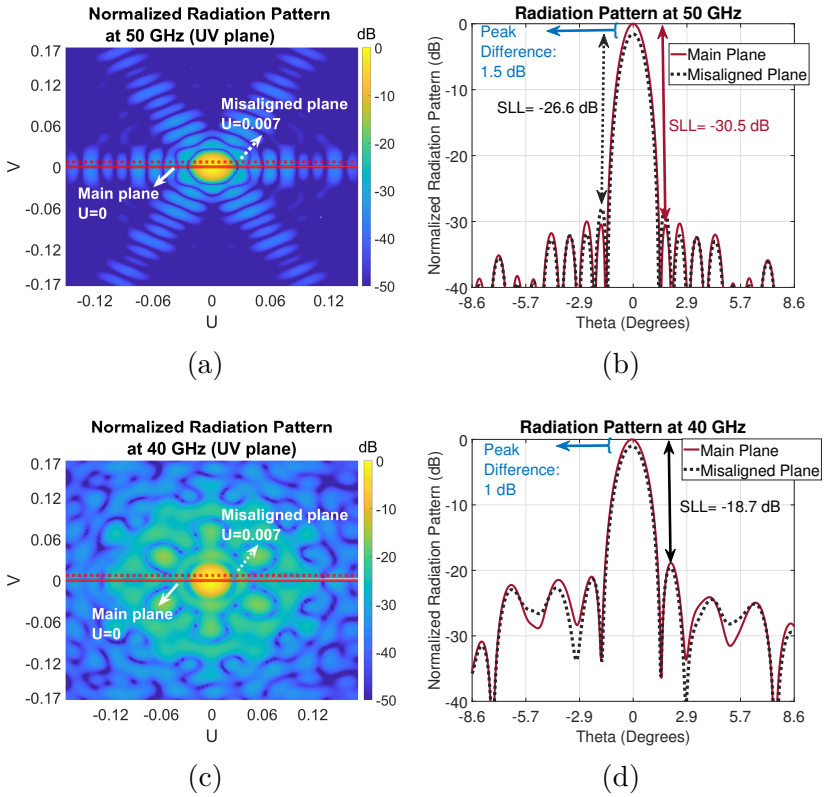

Figure 2.17 Study of the misalignment in the radiation patterns. Illustration of the center and misaligned planes in the radiation patterns at (a) 50 GHz, and (c) 40 GHz, and normalized 2D radiation patterns at the center and misaligned planes at (b) 50 GHz, and (d) 40 GHz.

a ratio of 0.77. Fig. 2.18 shows that while tolerance slightly affects the gain in the Q-band, it impacts the V-band gain by up to 3 dB. The figure also includes a region of uncertainty highlighted in blue. This region is defined between the maximum possible gain (from full-wave simulations of the RA without errors) and the worst-case scenario, defined by the tolerance that produces the lowest gain, plus a 1 dB reduction caused by the misalignment. Fig. 2.18 shows that the measured gain curves are mostly within this uncertainty region, highlighting the correlation between the identified uncertainties and the measured data.

Finally, it is important to note that the antenna has several parameters whose variations impact the gain. While it is impossible to precisely determine the tolerance of each UC or reproduce all the gaps and errors in petal inclination, the analysis in this section demonstrates how the main uncertainties affect the performance of the RA, showing that the measurements fall within the expected range.

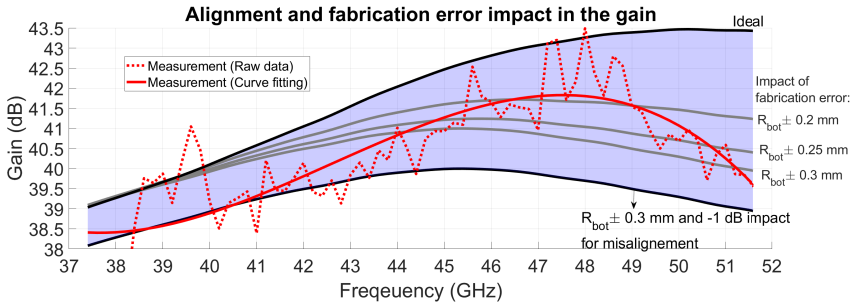

Figure 2.18 Gain incertitude caused by the misalignment and fabrication errors.

2.5 Discussion of the results

The measured 1-dB gain BW above 10% and AR BW of 31.5% allow qualifying the design as wideband in both aspects. Table 2.3 summarizes the performance of this design in contrast with previous reports. As the design resembles various unique characteristics (multi-faceted, large aperture, circular polarization), the other works are selected to be comparable in at least one aspect. The table shows that:

- The only multi-faceted RA reporting measurements is [2], which is a 3-faceted RA similar to the one shown in Fig. 2.10. The design is for the Ka band, and its aperture measures less than half of that presented in this work. While the 1-dB BW and aperture efficiency are higher than the ones presented in this work, the analysis in Sections 2.3.2 and 2.3.3 shows that the seven-faceted RA improve the 3-dB gain by 3%, and maintains a pencil beam in all the planes.
- A planar, large aperture is presented in [32]. It is only evaluated at 35.75 GHz. In contrast, the design presented in this work is wideband while having a large apreture.
- The RA in [32] covers the K and V bands. This design is one of the few covering the V-band, although they consider a frequency higher than this work. The reported RA has an aperture of less than half and a 1-dB BW 3% higher than the one presented in this investigation.
- The work in [26] presents a planar, circular polarized RA with a 1-dB AR BW of 16.9%. This result is 14.6% below that of the design in this work.
- [40] shows a hexagonal foldable aperture RA. While the design has various faces, it is a planar RA when deployed. The design has a small aperture and a low 1-dB gain BW of 9%.

Various designs in Table 2.3 have a higher 1-dB BW. Nonetheless, these designs have apertures that are less than half of the aperture of the RA in this chapter. This remark is critical because the BW is relative to the electrical size of the aperture. Indeed, if all the designs were to have a comparable aperture size, the seven-faceted geometry is expected to have a larger gain BW. This was proved in the analysis presented in Section 2.3.3.

Table 2.3 Comparison with other works

Ref.	**Multi-faceted (MF) Planar (P)**	**Frequency Range (GHz)**	f_0 **(GHz)**	**Aperture Size**	**Polarization**	**BW**	
						1dB Gain	**1 dB AR**
[**2**]	MF	27 - 40	28	18 λ_0 x 18 λ_0	Dual-Linear	21.4%	-
[**1**]	P	35.75	35.75	596 λ_0 x 18 λ_0	Dual-Linear	Single frequency	-
[**32**]	P	18-27.5 60-75	24 65	17 $\lambda_{0,high}$ x 17 $\lambda_{0,high}$	Linear	32% 15.7%	-
[**26**]	P	16-21 25-32	18.95 28.5	10 $\lambda_{0,high}$ x 10 $\lambda_{0,high}$	Circular	16.7% 12.4%	16.9%
[**40**]	P	14.5-17.5	16	7.6 λ_0 x 7.6 λ_0 *	Linear	9%	-
This Work	MF	37.5-51.5	47.6	55.2 λ_0 x 55.2 λ_0 *	Circular	13.4%	31.4%

*** RA with hexagonal aperture. The size is expressed as a square to facilitate the comparison**.

2.6 Conclusions

A seven-faceted, large aperture, circular polarized, and wideband RA was presented. Initially, the chapter shows a methodology for choosing a configuration that leads to a decrease in the phase error. As a result, a seven-faceted RA with petals' inclination angle of 4.5^o is studied. The RA decreases the phase error by tens of degrees compared to the planar and other multi-faceted configurations, leading to a more directive radiation pattern. The fabricated RA has a peak gain of 41.8 dB at 47.6 GHz, giving a 1-dB gain BW of 13.4% (44 GHz to 50.4 GHz) and a 3-dB gain BW from 39.8 GHz to 51.5 GHz (25.6%) covering the V-band and the upper portion of the Q-band. Although the lower Q-band falls 0.4 dB below the 3-dB gain BW limit, the proposed RA maintains a pencil beam directed towards the desired direction at these frequencies as well. This feature offers a distinct advantage over planar RAs, whose main beam vanishes, and over an equivalent 3-faceted RA, which experiences more than a 5 dB reduction in the main beam at the lower edge of the Q-band. The measurements also show that the RA's SLLs remain between -12 dB and -20 dB, and the axial ratio remains below 1-dB across the entire frequency range. The reported RA covers two bands rarely found in the literature and has a large aperture while keeping a large BW for both gain and axial ratio.

Multi-faceted RAs, as the proposed in this chapter, offer versatility for deployment in satellite applications. Although the prototype presented was assembled in a 3D printed plastic platform, some information on the use of hinges have been explored in [39]. Hinges allow

to achieve better accuracy in the petals' alignment. Nonetheless, its inclusion in the design requires deep study as explained in [39]. The impact of the hinges in the design, and other alternatives for deployment remain as future work.

CHAPTER 3 A DUAL-BAND, LARGE MULTI-FACETED REFLECTARRAY USING A FREQUENCY SELECTIVE SURFACE-BASED UNIT CELL

3.1 Introduction

The rapid advancement of telecommunications has led human civilization into a new space exploration and utilization era. Tens of satellites are launched each year to support the ever-growing global telecommunication network. Satellite technology has predominantly relied on the X, K_a, and K_u frequency bands in recent decades. However, these bands are nearing their capacity limits [46,47]. The satellite industry is investigating higher frequency bands to meet the increasing data demands. Specifically the Q and V bands (37.5–42.5 GHz and 47.2–51.4 GHz, respectively). Although these higher frequencies allow for greater data throughput, they also experience more significant atmospheric losses, necessitating antennas with high gain, leading to larger apertures to achieve reliable performance.

Reflectarrays (RAs) have emerged as a promising technology for space applications in recent years. However, most existing RAs designs are for CubeSats, are limited to single/narrow-band operation, and need more efficiency [38,39]. Notable examples of launched RAs include ISARA (Integrated Solar Array & Reflectarray Antenna), which operates at 26 GHz with an efficiency of 26%, and OMERA (One Meter Reflectarray), which achieves 42% efficiency at 37.75 GHz. Besides CubeSats, RAs are also considered a viable solution for telecommunications gateway links. Although extensive research has been conducted on X, K_a, and K_u band RAs, resulting in a wealth of literature and design examples [5,6,8], RAs operating in the Q and V bands remain largely unexplored. The limited existing research in these bands primarily focuses on designs with small apertures, linear polarization, and single-band operation. For instance, the design reported in [13] features an aperture size of $19.89\lambda_0$ x $19.89\lambda_0$ at a center frequency of 42.5 GHz. Another example in the Q-band is presented in [14] with an aperture size of $18\lambda_0$ x $18\lambda_0$, centered at 45 GHz. Similarly, [32] discusses a K/V-band RA with an aperture size of $16.7\lambda_0$ x $16.7\lambda_0$, and [77] explores designs at higher frequencies around 73 GHz.

Large aperture sizes are essential for high-gain performance in the Q/V bands, but they have been rarely studied. One notable example is the 5-meter RA design in [1], with an aperture size of $596\lambda_0$ x $18\lambda_0$, which demonstrates the fundamental limitation of narrow bandwidth (BW) in such large RAs. To address this limitation, Chapter 2 and reports [73,78] proposed a multi-faceted RA using a single-band unit cell (UC). The RA has an equivalent aperture

size of $55.2\lambda_0$ x $55.2\lambda_0$. This study demonstrated that a multi-faceted setup enhances the gain BW compared to planar RAs. Moreover, the multi-faceted configuration provides a pencil beam in both the Q and V bands with peak gain at 50 GHz. However, a more optimal design for gateway links requires independent control in each of the two bands, leading to gain peaks at the center of each band.

This chapter introduces a novel dual-band UC that enables the design of a circularly polarized, multi-faceted RA with peak gains in both the Q and V bands. The main contributions of this chapter are:

- Proposal of a novel dual-band UC that offers independent phase control in the Q and V bands. The UC incorporates a frequency-selective surface (FSS) that acts as a reflector in the V band and a band-pass filter in the Q band. While similar concepts have been explored previously [33–36], the proposed UC is more compact and provides independent phase coverage exceeding 400° in both bands.
- To the best of the author's knowledge, this is the first demonstration of a dual-band, multi-faceted RA that has been experimentally measured. Previous multi-faceted RA designs in the literature are single-band, with most reporting only simulation results [42, 43]. Only the designs in [2] and Chapter 2 present measurement data.

The rest of the chapter is organized as follows. Section 3.2 details the performance of the novel FSS-based UC. Section 3.3 shows the RA prorotype, outlines the measurement setup, compares simulation and measurement results of the radiation pattern, and analyzes the gain bandwidth (BW) and axial ratio (AR). Section 3.4 compares the dual-band, multi-faceted RA's performance with previous works. Finally, the chapter concludes in Section 3.5.

3.2 Novel dual-band Unit cell

The proposed dual-band unit cell (UC) consists of a stack of layers with three functionalities, as illustrated in Fig. 3.1. The first layer, labeled as the *V-band*, comprises a dual-layer patch identical to the one proposed in Chapter 2. This layer is responsible for controlling the phase in the V-band. The second function is a dual-layer frequency selective surface (FSS), which serves as a ground for the V-band while allowing transmission in the Q-band. Finally, the third layer, labeled as *Q-band*, controls the phase within this frequency range. Once all the layers are stacked, the three functionalities are related by the inter-layer coupling. However, the overall impact of this effect is negligible as will be shown in Sections 3.2.1, 3.2.2, and 3.2.3.

Indeed, the FSS performs as a pass-band filter, and as a ground in the desired frequencies, and the V-band and Q-band layers are isolated in most of the cases.

Fig. 3.2 illustrates the simulation setup, and the oblique incidence tested for the circular polarized (CP) incident waves. The results of each functionality is detailed in the following subsections.

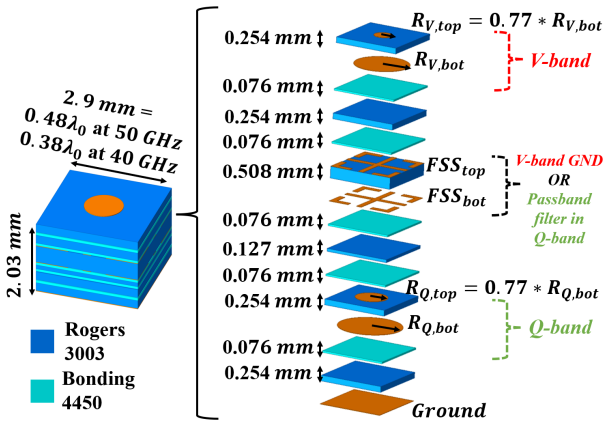

Figure 3.1 Exploded view of the Unit Cell.

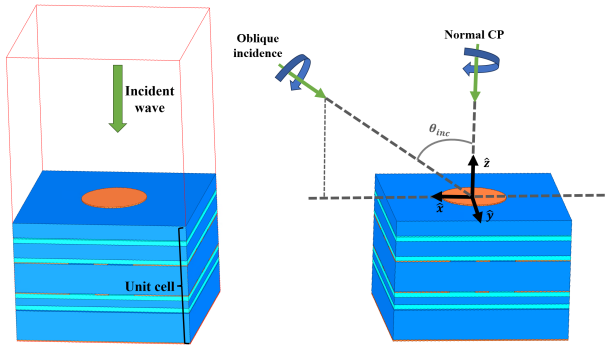

(a) (b)

Figure 3.2 (a) Simulations setup, and (b) representation of the oblique incident waves in the simulation.

3.2.1 Frequency Selective Surface

The objective of the FSS is to separate the Q and V bands by acting as a reflector in the V-band and as a passband filter in the Q-band. The FSS comprises two layers with identical grid lines and crosses, as shown in Fig. 3.3a. The magnitude of the simulated S-parameters

for an incident field circularly polarized is depicted in Fig. 3.3b. The FSS is reflective in the V-band with a magnitude higher than -0.55 dB for any oblique incidence below 35°. On the other side, the FSS allows the flow of the incoming waves in the Q-band with a magnitude above -1.7 dB for any oblique incidence. The matching in this band is better than -10 dB with an increase up to -5 dB near 42.5 GHz. This matching is sufficient to ensure the phase control in the Q-band as will be shown later. Although the FSS performs as a passband filter in the Q-band, the bottom of the UC has a metallic ground as shown in Fig. 3.1 to ensure the reflection of the energy.

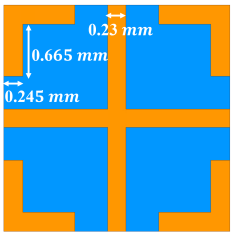

(a)

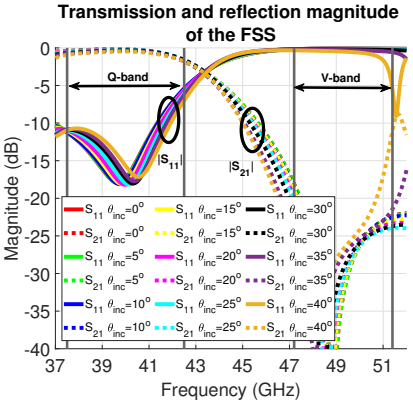

(b)

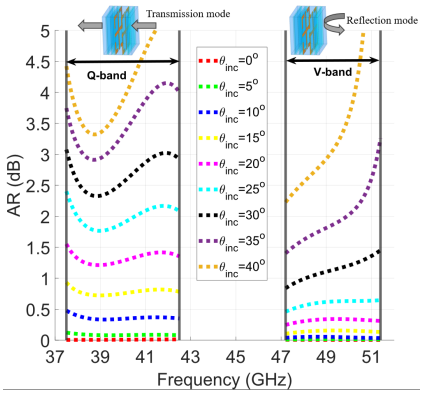

(c)

Figure 3.3 FSS (a) geometry, (b) magnitude of the simulated S-parameters, and (c) axial ratio.

Finally, Fig. 3.3c shows the axial ratio (AR) of the FSS for transmission in the Q-band and reflection in the V-band at various oblique incidences. The results indicate that the AR is better in the V-band than in the Q-band. Specifically, for V-band reflection, the AR remains below 1.5 dB for oblique incidences up to 30°, while for Q-band transmission, the AR at 30° is approximately 3 dB. These values provide insight into how the FSS affects the circular polarization of the RA. Further analysis of this topic will be done in the chapter.

3.2.2 V-band performance

The analysis in the V-band was done at 47 GHz, 49.5 GHz, and 52 GHz. The boundary frequencies are slightly outside the V-band range, as the UC was optimized at these points to ensure adequate performance across the actual band.

The reflection coefficient shown in Fig. 3.4 demonstrates that the FSS successfully isolates the V-band layers from the Q-band ones. Specifically, the phase control depends solely on $R_{V,bot}$, as illustrated in Figs. 3.4a, 3.4d, and 3.4g, which exhibit phase coverage of 409°, 477°, and 505° at 47 GHz, 49.5 GHz, and 52 GHz, respectively. Additionally, the amplitude of the reflection coefficient reveals insertion losses of less than 1 dB in most cases. Finally, Figs. 3.4c, 3.4f, and 3.4i display the AR, indicating that at 49.5 GHz, the AR remains below 3 dB for oblique incidences up to 20°. However, the AR rises above 5 dB in certain instances further from the center frequency.

3.2.3 Q-band performance

Similar to the V-band, the analysis conducted in this section extended consider the center frequency of the Q-band (40 GHz) and border frequencies out of it (37 GHz and 43 GHz). Figure 3.5 presents the reflection coefficient for a normally incident, circularly polarized wave. The reflection coefficient at the center frequency (Figs. 3.5d and 3.5e) mostly depends on $R_{Q,bot}$, though $R_{V,bot}$ also exerts some influence. The minimum amplitude is approximately -1 dB, and regardless of $R_{V,bot}$, the minimum phase range reaches 416° when $R_{V,bot} = 1$ mm. By contrast, the UC at 37 GHz and 43 GHz exhibits lower sensitivity to the V-band layers (Figures 3.5a, 3.5b, 3.5g, and 3.5h), covering phase ranges of over 335° and 406°, respectively. Additionally, while losses are reduced at 37 GHz compared to the center frequency, a region of insertion loss between 1 dB and 2 dB occurs at 43 GHz, remaining within acceptable limits for RA design.

The results for the reflection coefficient validate the mechanism's functionality in phase control within the Q-band. However, the effect of the oblique incidence in the FSS causes a deterioration of the AR. Figs. 3.5c, 3.5f, and 3.5i prove that the AR is 0 dB at normal incidence, below 3 dB for an incidence of 10°, and it increases to more than 5 dB in certain cases for an incidence of 20°. A more detailed analysis of this effect will follow in the discussion of the RA radiation patterns.

The primary advantage of the proposed dual-band UC is its capability for independent phase control in each band. This feature allows for independently optimizing the gain in each band. However, using the proposed FSS introduces AR degradation and increases the insertion loss.

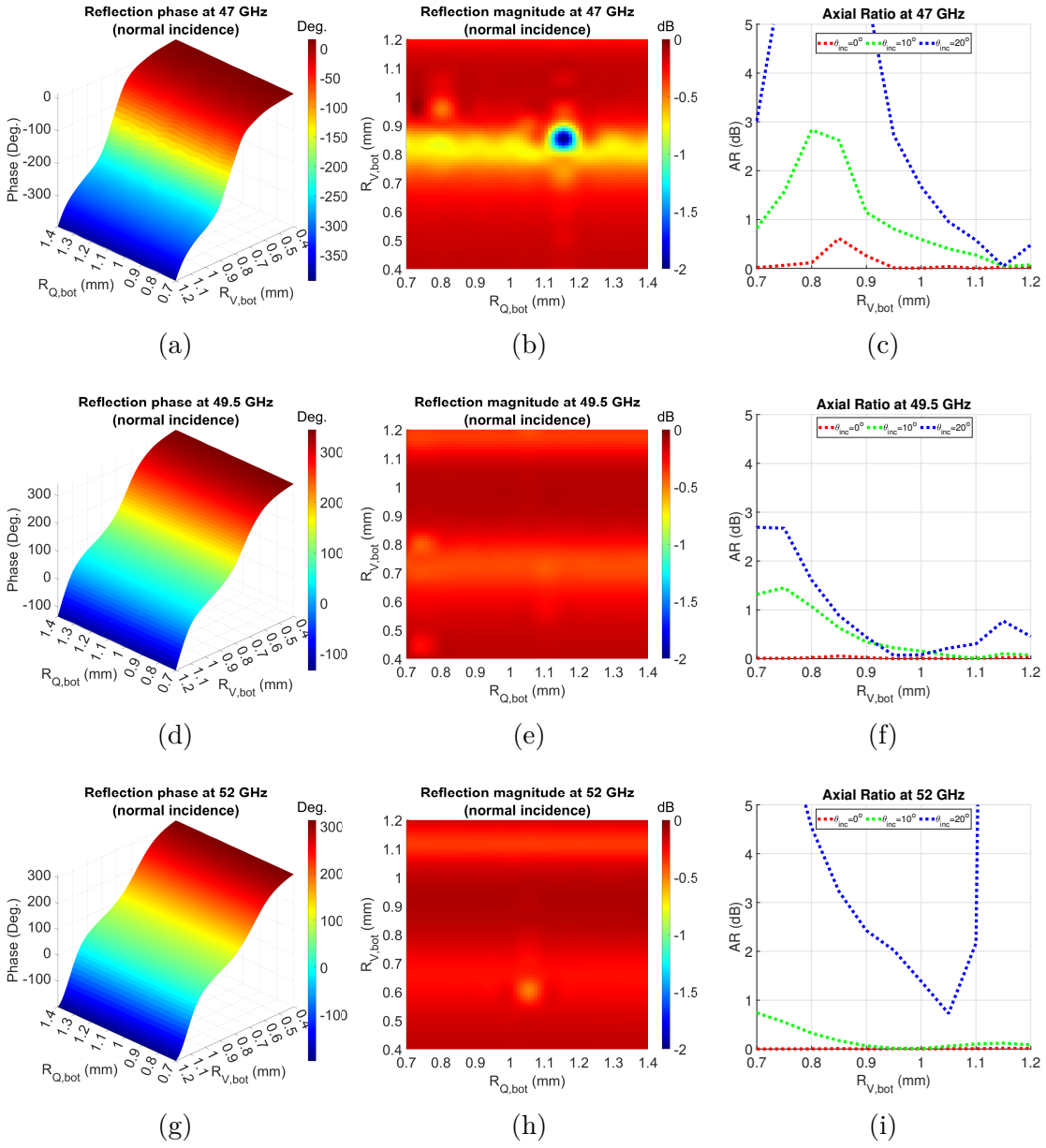

Figure 3.4 Reflection coefficient and axial ratio of the UC in the Q-band at 47 GHz (a), (b), and (c), at 49.5 GHz (d), (e), and (f), and at 52 GHz (g), (h), and (i).

These constraints must be considered in the RA optimization to mitigate their effects. The design and performance of the RA are discussed in the following section.

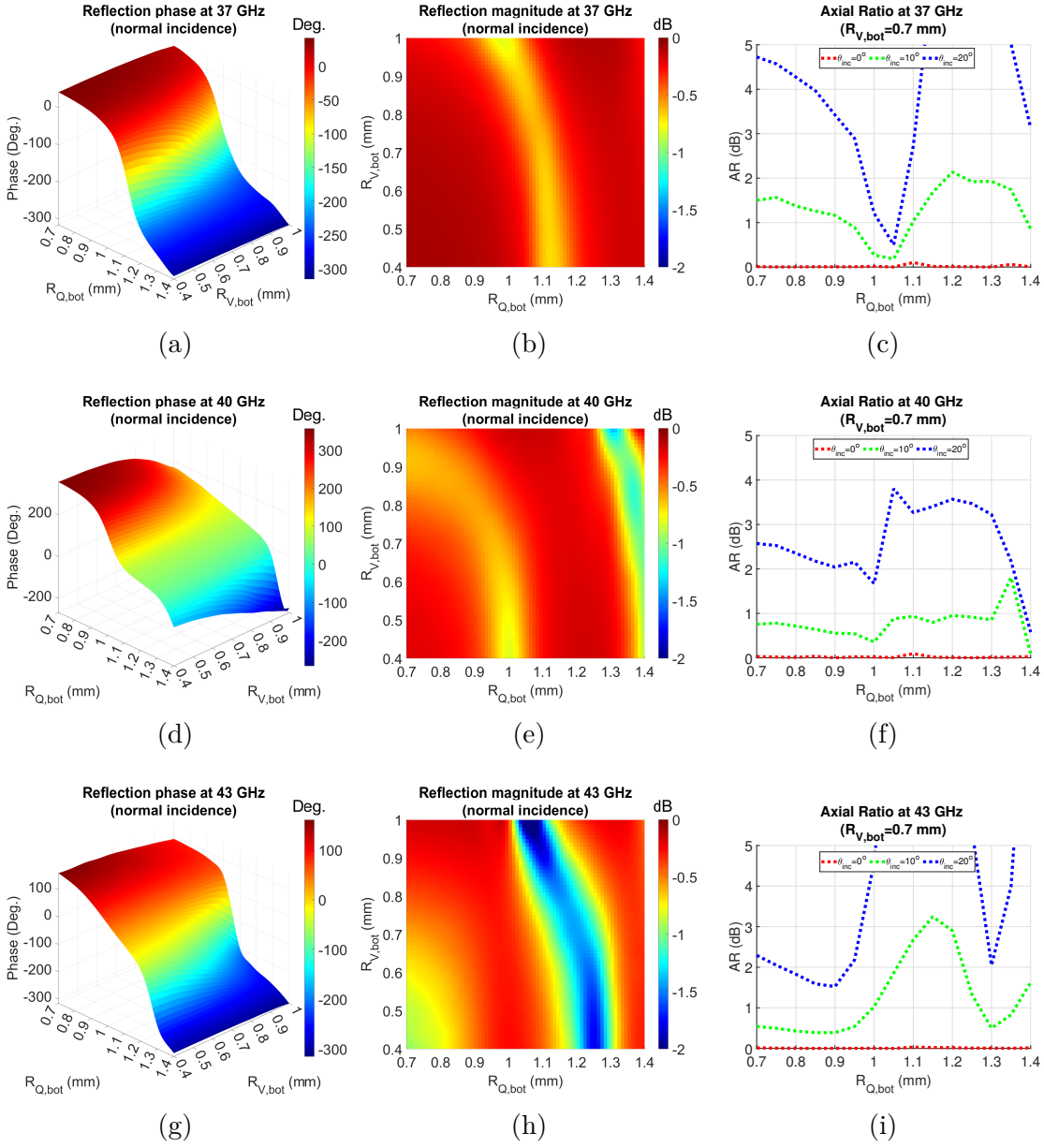

Figure 3.5 Reflection coefficient and axial ratio of the UC in the Q-band at 37 GHz (a), (b), and (c), at 40 GHz (d), (e), and (f), and at 43 GHz (g), (h), and (i).

3.3 Reflectarray performance

The RA setup is identical to the one presented in Chapter 2. For clarity, Fig. 3.6 reproduces the illustrations of the proposed offset RA. Fig. 3.6a shows the multi-faceted RA, which consists of a central hexagon and six petals inclined at an angle (ψ_{petal}). Fig. 3.6b displays the physical aperture of the RA, which measures 36.23 cm ($60.4\lambda_{50GHz}$ or $48.3\lambda_{40GHz}$). The

edge-to-edge length of the regular center hexagon (face 1) is defined by (3.1). Figs. 3.6c and 3.6d present the position of the horn antenna and its angle of incidence to the RA. The plot indicates that most incidences are below 20°, although some UCs at the corners of petals 2, 3, and 7 reach up to 24°. Finally, Fig. 3.6e illustrates the antenna's UV plane, which is the reference plane for presenting the radiation patterns.

$$L_{petal} = \frac{L_{RA} - L_{hex}}{2 \times cos(\psi_{petal})} \tag{3.1}$$

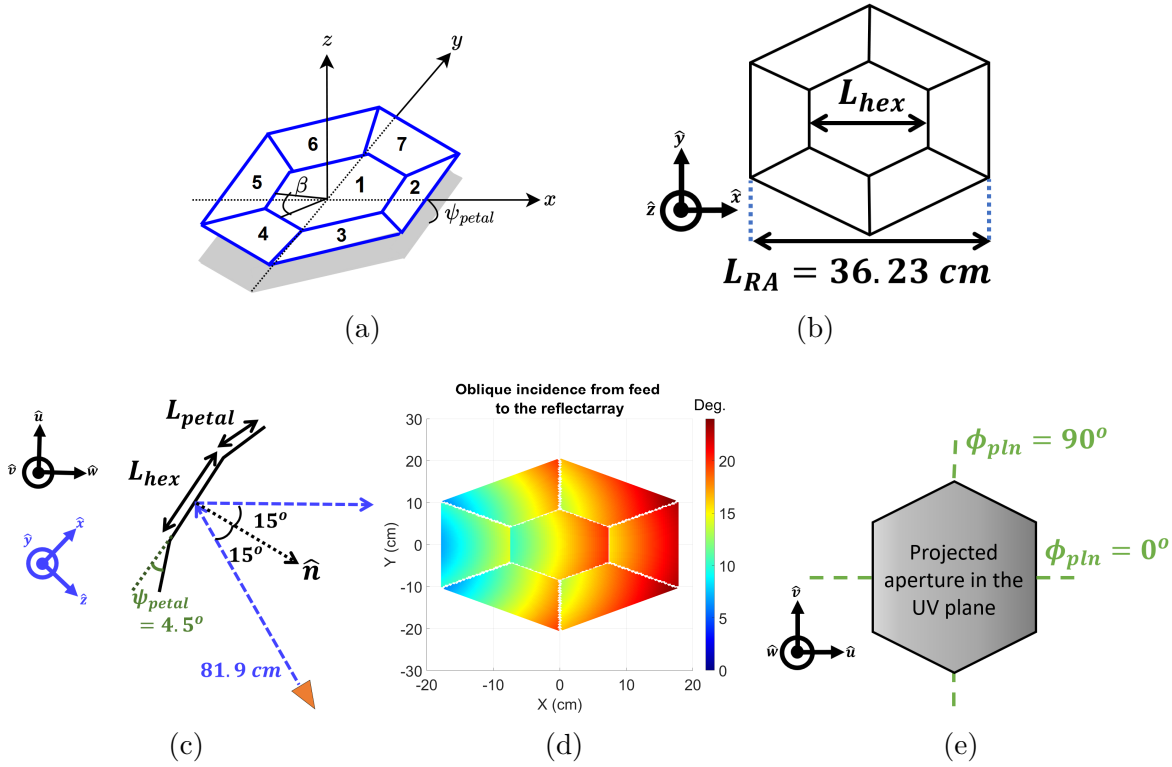

Figure 3.6 Multi-faceted RA, (a) Isometric view, (b) top view, (c) side view including the horn antenna in the bottom-right corner, (d)oblique incidence from the horn antenna to the reflectarray, and (e) UV plane of the RA.

Chapter 2 presented the equation for calculating the phase distribution of a reflectarray (2.5). The tunability of the proposed UC in the Q and V bands enables separate control of 40 GHz and 49.5 GHz, whose phase distributions are illustrated in Fig. 3.7. The phases and UC parameters $R_{Q,bot}$ and $R_{V,bot}$ are related as shown in Figs. 3.5 and 3.6. The radii of the V-band UCs are chosen first, as they are independent of the other layers. In contrast, the radii of the Q-band UCs are coupled with the other layers and must be selected accordingly. This approach maximizes gain at the center frequencies of the Q and V bands. Fig. 3.8a

shows the Gerber file of the center hexagon, and Fig. 3.8b displays a photo of the fabricated RA.

The RA was measured in a compact antenna test range (CATR). The faces were mounted on a 3-D printed base, which was then attached to a metallic structure, as shown in Figs. 3.8c and 3.8d. The horn antenna used is a circularly polarized model provided by MDA. Besides the antenna, the setup includes a feed chain polariser.

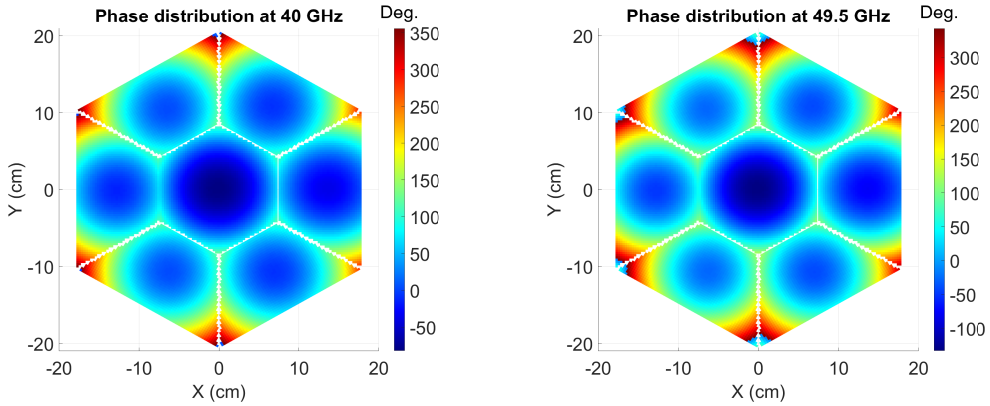

(a) (b)

Figure 3.7 Phase distribution at (a) 40 GHz, and (b) 49.5 GHz.

The CATR in the Poly-Grames facilities does not have a circularly polarized standard gain horn for the measurements. Instead, measurements of orthogonal, linear polarizations are taken and post-processed using the methodology proposed in [76]. In this work, we selected right-handed circular polarization (RHCP) as co-polarization and left-handed circular polarization (LHCP) as cross-polarization. The radiation pattern, gain, and AR are discussed in the following section.

3.3.1 Performance

The performance of the RA is evaluated by comparing simulated and measured radiation patterns, as well as analyzing the measured gain and AR. Simulations are done in TICRA-QUPES. Due to the number of layers and the resonance of the UC, significant computational resources are required. Consequently, the simulation accuracy is set to *Normal* rather than the recommended *Enhanced* or *High* settings. The simulations required several weeks to complete, even with *Normal* accuracy.

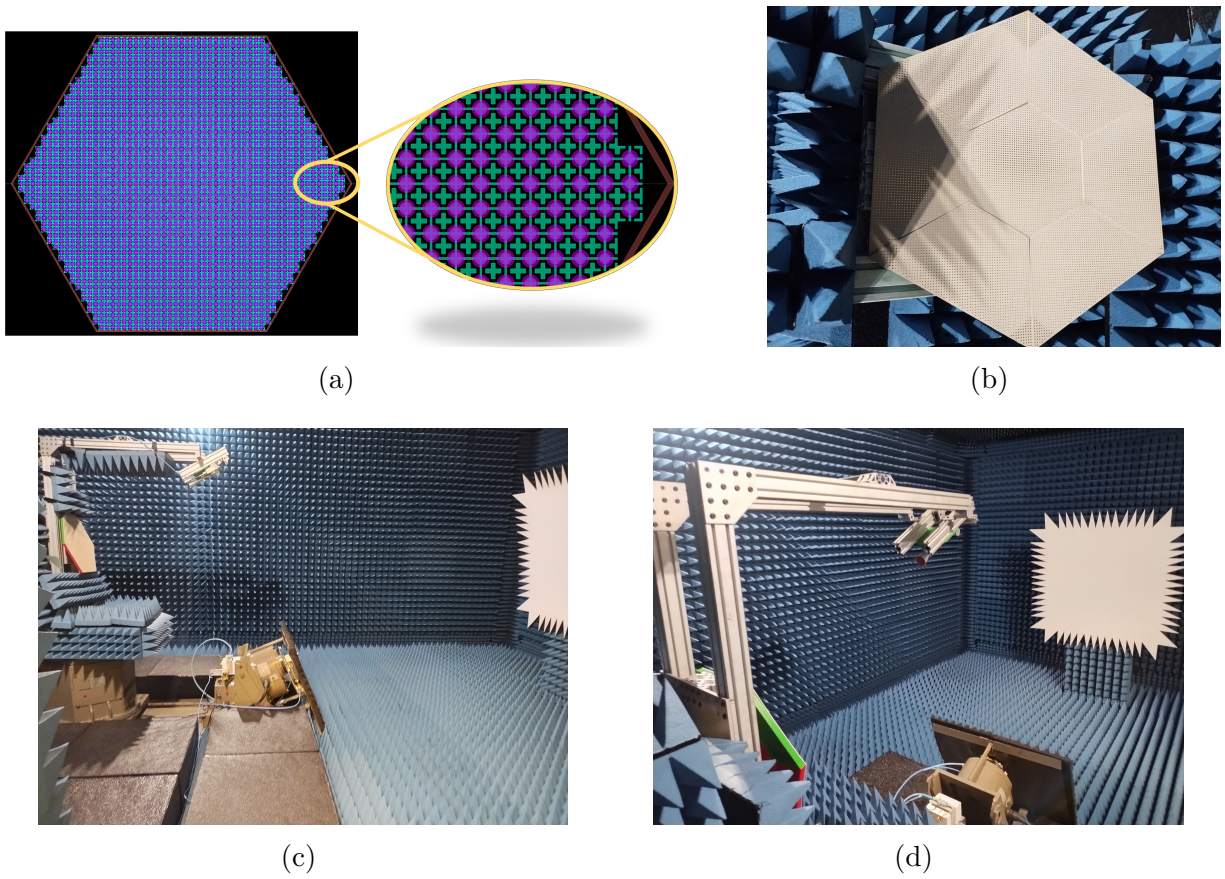

Figure 3.8 Fabrication of the antenna, (a) gerber file of the center hexagon (face 1), and photos of the complete RA in the compact antenna test range from the (b) front, (c) side, and (d) back.

Radiation pattern

Fig. 3.9 shows the normalized radiation patterns for the border and center frequencies of the Q and V bands. Fig. 3.10 shows the measured radiation pattern for 40 GHz and 50 GHz in the planes $\phi = 0°$, 45° and 90°. The main parameters of the patterns are provided in Table 3.1. Results indicate that the RA successfully reflects a pencil beam across all frequencies. In both simulations and measurements, the main beam is in agreement, as proven by the half-power beamwidth (HPBW), which is between 1.15° and 1.4° with a discrepancy of less than 0.15° between the two. The measured sidelobe levels are higher than in the simulations but remain below -12 dB (except for the pattern at 42.5 GHz). Similarly, cross-polarization levels differ in the measurements, showing higher values in most cases. This increase in cross-polarization leads to an AR between 0 dB and 3.8 dB in most cases. However, the AR reaches 5 dB at 42.5 GHz, as shown in Table 3.1. The reason for the high AR is the

performance of the UC for oblique incident waves, as explained in Section 3.2. The results show a considerable deterioration at 42.5 GHz. This performance is because the radius of the Q-band UCs in the center hexagon ranges between 0.96 mm and 1.08 mm, and the axial ratio for these cases is more than 5 dB, as shown in Fig. 3.5i. These radii were selected to maximize the gain at 40 GHz, neglecting the performance at the border frequencies.

Table 3.1 Comparison of measurements and simulations

	37.5 GHz		**40 GHz**		**42.5 GHz**		**47.2 GHz**		**50 GHz**		**51.4 GHz**	
	Sim.	**Meas.**	**Sim.**	**Meas.**	**Sim.**	**Meas.**	**Sim.**	**Meas.**	**Sim.**	**Meas.**	**Sim.**	**Meas.**
HPBW (°)	1.3	1.4	1.25	1.4	1.24	1.2	1.17	1.14	1.13	1.25	1.15	1.27
SLL (dB)	-16.63	-12	-22.76	-14.63	-18.46	-5.46	-14.52	-13.86	-26.88	-15.06	-18.38	-14.6
AR (dB)	0.46	0.33	0.99	1.92	2.82	8.11	2.46	2.15	0.56	3.83	1.76	2.69

Gain and axial ratio bandwidth

Table 3.2 shows the measurements of the gain and aperture efficiency of the RA. The maximum aperture efficiencies are observed at the center frequencies: 15.5% in the Q-band and 17.24% in the V-band. The decrease in the efficiency compared to the single, wide-band design of Chapter 2 is due to the high axial ratio, and the insertion loss associated to the FSS resonance in the Q-band. Table 3.2 also shows the results of the full-wave simulations done in TICRA-QUPES, due to the complexity of the simulation, just six points in frequency were calculated. The results show discrepancies among 8 dB and 5 dB compared to the measurements. In addition to the limitations of misalignment and fabrication errors explained in Chapter 2, the difference is related to the accuracy limitation of the simulations with the proposed UC.

The gain and AR curves in que Q and V bands are depicted in Fig. 3.11. The trend curves are derived from a polynomial regression based on the raw data from the measurements. The curves indicate that the gain reaches a peak in each band, demonstrating the dual-band functionality of the proposed UC. Moreover, the 1-dB gain BW is 6.5% in the Q-band and 5.6% in the V-band, while the 3-dB gain BW is 10.7% in the Q-band and >8.9% in the V-band. The plot also shows that the AR remains below 3.8 dB across most of the targeted frequency range.

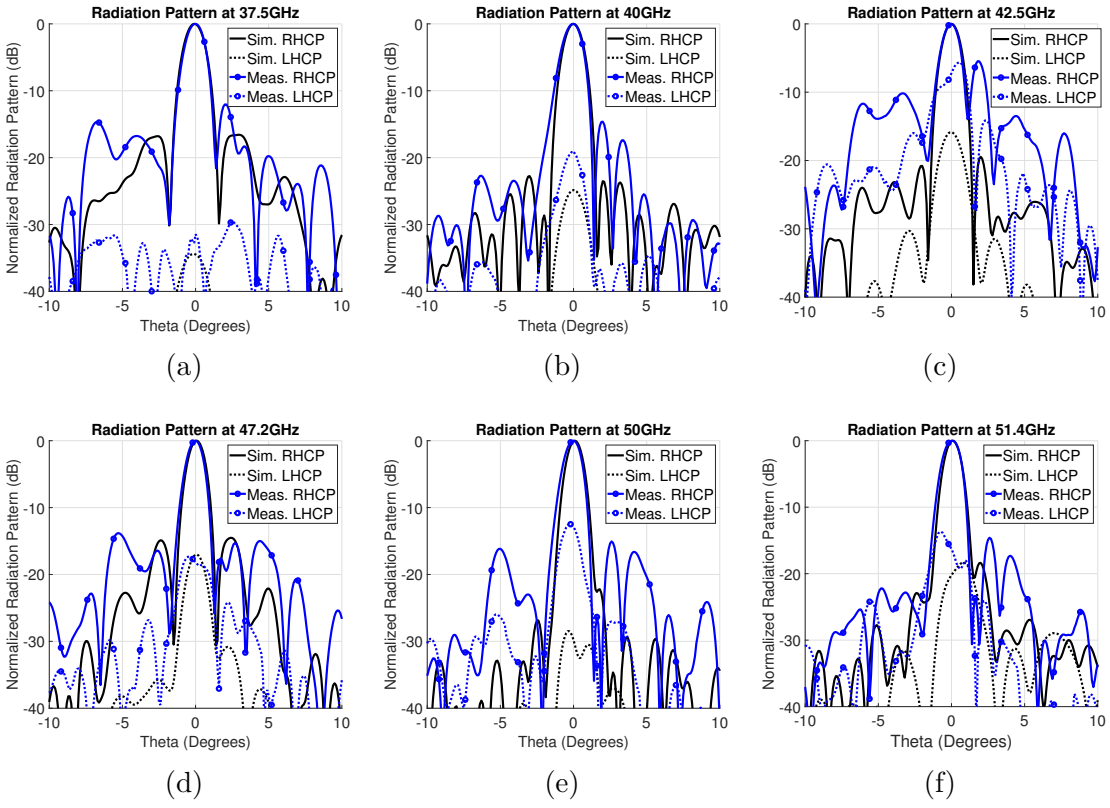

Figure 3.9 Simulations and measurements of the radiation pattern at (a) 37.5 GHz, (b) 40 GHz, (c) 42.5 GHz, (d) 47.2 GHz, (e) 50 GHz, and (f) 51.4 GHz.

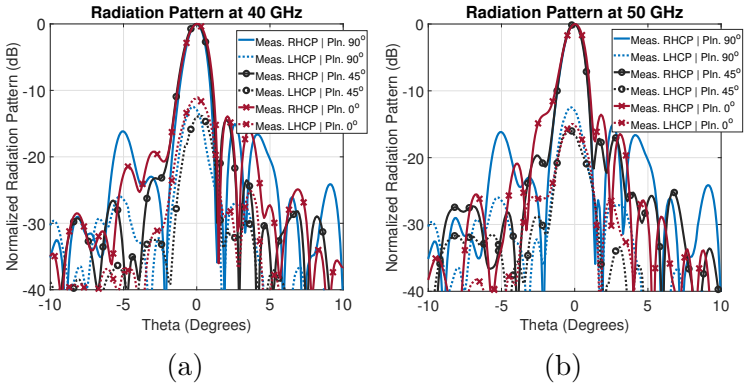

Figure 3.10 Measurements of the radiation patterns at three planes in (a) 40 GHz, (b) 50 GHz.

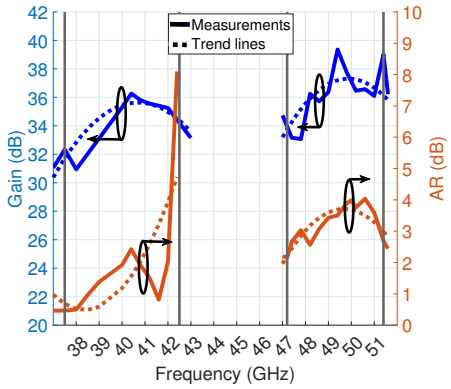

Figure 3.11 Gain and axial ratio of the RA.

Table 3.2 Gain and aperture efficiency

		37.5 GHz	**40 GHz**	**42.5 GHz**	**47.2 GHz**	**50 GHz**	**51.4 GHz**
Meas.	**Gain (dB)**	32.94	35.3	34.1	34	37.7	36.2
	Ap. eff.	10.24%	15.5%	10.41%	8.25%	17.24%	11.55%
Sims.	**Gain (dB)**	40.33	40.9	41.1	42.07	43.04	42.2
	Ap. eff.	50.05%	50.15%	46.52%	47.16%	52.54%	40.97%

3.4 Discussion

The proposed dual-band RA can be evaluated from two perspectives: through comparison with the equivalent single-band design presented in Chapter 2 and through comparison with other FSS-integrated RAs. Table 3.3 presents the main parameters for analyzing the first perspective. The comparison shows improvement in the phase coverage of the dual-band UC due to the integration of the FSS. As shown before, the newly added layers allow independent control of the Q and V bands. However, this enhancement comes at the expense of increased insertion loss and AR. Both of these deteriorations are due to the resonances of the FSS, which also make the UC more sensitive to oblique incidences. These changes in the dual-band UC directly impact the RA gain, which is lower at 40 and 50 GHz than the single-band design. The advantage of the dual-band UC lies in its ability to maximize gain in each band, achieving two 1-dB bandwidths of 6.5% and 5.6%. In contrast, the single-band RA has a single gain peak and a broader 1-dB gain BW (13.4%), but its gain drops around 4 dB from the V to the Q-band. While the measured gain is less in the dual-band RA than in the single-band one, a dual-band UC with better response for oblique incidences could solve this limitation and overcome the single-layer performance.

For the second perspective, Table 3.4 compares different features of the proposed RA with

Table 3.3 Comparison of the multi-faceted reflectarray using a single and dual band unit cell

	Unit Cell performance				**Reflectarray performance**			
	Phase coverage		**Insertion loss (dB)**	**AR (dB)**	**Gain (dB)**		**1-dB Gain**	**AR (dB)**
	40 GHz	**50 GHz**			**40 GHz**	**50 GHz**		
Single band UC	306°	464°	≤ 0.5 dB	~ 0	39.2	40.7	13.4%	< 0.9
Dual band UC	$\sim 439°$	475°	≤ 2 dB	Variable	35.3	37.7	6.5% 5.6%	< 3.8

previous works. The selected studies include multi-band RAs with FSSs integrated into the UCs. Some key characteristics of the proposed RA that are deduced from the table are:

- Most previous works cover frequency bands up to 31 GHz (K_u-band) with aperture sizes below $45.8\lambda_{f_0}$. This study is one of the first to explore the Q and V bands using a dual-band UC with an aperture size of more than $48\lambda_{f_0}$.
- Previous designs based on FSSs required large air spacers between the bands. In contrast, the UC proposed here does not require spacers, resulting in a lower profile and easier fabrication. This reduction in profile is due to the double-layer used for each band in the UC. Other designs use single-layer UCs with large air spacers to achieve a smooth, wide-phase range coverage, whereas the proposed UC achieves this with a binded, double-layer configuration.
- The proposed RA uses a single horn antenna as the feeder, a preferable configuration for satellite applications. In contrast, most other designs use multiple feeds positioned at variable distances.

The table also compares gain and AR. Results show that the AR in the proposed RA is higher than in the other works, indicating increased cross-polarization, directly impacting the gain. Nevertheless, the proposed RA has a comparable 1-dB gain bandwidth to those reported in [34, 36] and outperforms the bandwidths in [33, 35]. This gain BW is a noteworthy result, given that the RA aperture size is larger than in the other works, demonstrating the benefit of using a multi-faceted configuration. Moreover, the design has space for improvement by using a UC with a more stable performance for oblique incidences.

Table 3.4 Comparison with other works

Ref.	Multi-faceted (MF) Planar (P)	Frequency Range (GHz)	Aperture size	Thickness	Air Spacers	Polarization	Gain BW	AR (dB)	Number of feeds
[33]	P	12.25 - 12.75 29.5 - 30.5	$14.17\lambda_{12.5}$ $34\lambda_{30}$	$0.52\lambda_{12.5}$ $1.25\lambda_{30}$	Yes	Circular	3-dB 7.2% 5.8%	< 3	1
[34]	P	19.5 - 20.5 29.5 - 30.5	$12\lambda_{20}$ $18\lambda_{30}$	$0.3\lambda_{20}$ $0.4\lambda_{30}$	Yes	Dual-linear	1-dB ∼5% ∼3.3%	N/A	2
[35]	P	12.25 - 12.75 14 - 14.5 19.6 - 21.2 29.4 - 31	$16.7\lambda_{12.5}$ $19\lambda_{14.3}$ $27.2\lambda_{20.4}$ $40.3\lambda_{30.2}$	$0.38\lambda_{12.5}$ $0.43\lambda_{14.3}$ $0.62\lambda_{20.4}$ $0.92\lambda_{30.2}$	Yes (x2)	Circular	3-dB ∼23% ∼7.8% ∼5.3%	< 3	3
[36]	P	7.25 - 7.75 7.9 - 8.4 20.2 - 21.2 30 - 31	$11.3\lambda_{7.5}$ $12.2\lambda_{8.15}$ $31.1\lambda_{20.7}$ $45.8\lambda_{30.5}$	$0.44\lambda_{7.5}$ $0.48\lambda_{8.15}$ $1.22\lambda_{20.7}$ $1.79\lambda_{30.5}$	Yes (x5)	Circular	1-dB Not given ∼6.8% ∼5.76%	< 1	3
This work	MF	37.5 - 42.5 47.2 - 51.4	$48.3\lambda_{40}$ $60.4\lambda_{50}$	$0.27\lambda_{40}$ $0.34\lambda_{50}$	No	Circular	1-dB 6.5% 5.6%	< 3.8	1

3.5 Conclusion

This chapter described an FSS-based UC and presented the simulations and measurements of a dual-band reflectarray (RA) that enables independent phase control in the Q- and V-bands. The proposed UC enhances phase coverage, increasing it by 10° at 50 GHz and 133° at 40 GHz compared to the equivalent single-band UC presented in Chapter 2. However, the analysis showed that integrating the FSS introduces resonances, affecting the UC's stability for oblique incidences. As a result, the UC exhibits up to 1.5 dB more insertion loss in certain cases and an axial ratio of up to 3.8 dB across most of the Q/V bands. Despite these limitations impacting the RA gain, the dual-band configuration achieves gain peaks at 40 and 50 GHz, resulting in 1-dB gain bandwidths of 6.5% and 5.6% at the Q- and V-bands, respectively. The proposed design is also more compact, eliminating the need for air spacers in the UC and using a single feed. Furthermore, the multi-faceted configuration allows for a superior 1-dB gain bandwidth, even with a larger RA aperture size than previous works. Future improvements could focus on enhancing the UC's stability to oblique incidences, further improving its axial ratio and gain.

CHAPTER 4 DESIGN AND CHARACTERIZATION OF A UNIT CELL WITH WIDE-ABGLE RECONGFIGURABILITY BASED ON ANISOTROPIC AND BIANISOTROPIC HUYGENS METASURFACES

4.1 Introduction

Metasurfaces have opened a limitless avenue to engineer electromagnetic waves, ranging from negative refraction index [3] to the multiple material transformations offered by the susceptibility and impedance synthesis [59, 60]. The development of these methodologies has led to a major interest in reconfigurable metasurfaces. Indeed, various examples have been reported for control of the transmission behaviour in recent years: planar Fresnel lenses using pin/varactor diodes [48,65–67], beam tilting using phase-gradient structures employing varactor diodes [49, 68, 69] or mechanical rotation [79], and a few studies on active Huygens' metasurfaces [70, 71, 80].

Impedance modeling is the most common methodology to design Huygens metasurfaces [56, 60]. Using this approach, one can design unit cells (UCs) for beam tilting using a phase gradient design approach [50]), as well as wide-refraction-angle applications where bianisotropic metasurfaces prove advantageous due to their potential to compensate for impedanc mismatch effects [51]. In passive designs, the impedances are achieved using geometries with multiple degrees of freedom. In contrast, active UCs often have one degree of freedom per layer (implemented through tunable elements such as pin/varactor diodes). Consequently, active designs necessitate more complex geometries to achieve comparable impedance tuning capacilities. For instance, a previous work presents simulations of a metasurface, each layer of which achieves an impedance range of more than $j500\ \Omega$ [70]. However, the study lacks physical insights into the UC synthesis, and does not provide experimental validations. Additionally, a Flip Chip DIE package is used, which offers a good relationship between the losses and the capacitance range, but requires special equipment for soldering which becomes challenging to use in surfaces with tens or hundreds of elements. Other studies have presented UC characterization using waveguides focusing on the magnitude and phase reconfigurability [50, 61–64]. However, they do not characterize the layers' reactances and do not validate the UCs as a supercell or full metasurface. A recent work introduces mathematical and physical approaches to calculate reactances for an optimized bianisotropic metasurface response [54]. Nonetheless, the theoretical nature of these approaches lacks an insight into the challenges of physically designing the UCs. This Chapter presents the characterization of an active, three-layer UC by proposing a methodology to increase its tunability, stud-

ies the impact of the inter-layer coupling on the reactances, and evaluates anisotropic and bianisotropic UCs for beamsteering applications. The three axes of the Chapter are:

- To present a design methodology for wide reactance tunability, meeting the requirements for bianisotropic applications through impedance synthesis, and for phase gradient applications using anisotropic UCs (i.e. three-layers with identical top and bottom layers). Unlike conventional active designs [49, 68, 69], our approach employs miniaturized, double-resonant geometries to enhance reactance tunability. The effectiveness of the proposed geometries is validated through waveguide measurements.
- To characterize the inter-layer coupling and its impact on the reactance of each layer. Typically, multi-layer UCs are optimized post-synthesis to account for these coupling effects [49, 51, 52, 68, 69]. A previous work has proposed a model that incorporates mutual coupling effects into the analysis, and has tested this method in simulations a fabrication of a passive metasurface [53, 81]. This Chapter examines the impact of mutual coupling on the synthesized reactance of each layer using equations that inherently consider these effects. The analysis reveals the limitations that coupling imposes on reactance tunability. Furthermore, the study demonstrates that the impact varies for different geometries by examining two distinct UC families to address these limitations. The coupling effects on reactance are also validated through waveguide measurements.
- To validate the response through simulations of a supercell. In contrast to previous works that focus exclusively on phase gradient design techniques [49, 68, 69], this work introduces a UC that can be tuned for beam tilting applications using the phase gradient approach, or design to address wide refraction angles using bianisotropic metasurfaces through the use of impedance synthesis techniques.

The rest of the Chapter is organized as follows. Section 4.2 demonstrates the unit cell and its reactance requirements and explores the reconfigurability for the proposed dual-resonant metasurface layers. Section 4.3 studies the complete UC and presents the reactance calculations considering the inter-layer coupling effects. Next, Section 4.4 validates the single-layer and inter-layer coupling characterizations through waveguide measurements. Following this, Section 4.5 shows the performance of the proposed reconfigurable UC through the design and simulation of a supercell switching between a bianisotropic design for wide refraction, and an anisotropic design for beam tilting applications. Next, Section 4.6 shows a comparison of this work with relevant previous works from the literature. The Chapter concludes in Section 4.7.

4.2 Unit Cell Design

Fig. 4.1 shows a representation of the UC under study, which consists of a stack of three layers embedded within a radome. The number of layers meets the minimum requirement to achieve a phase coverage of 360^o with high transmission efficiency [58] and to implement bianisotropic metasurfaces [56]. The design frequency is 2.45 GHz ($\lambda_0 = 12.24\ cm$), and the physical parameters of the UC are $t_r = 1.58\ mm$, $t_s = 5.1\ mm$ (total thickness equals $0.11\lambda_0$), and $p = 24\ mm$ ($0.196\lambda_0$). This section shows the study of the impedance of all the three layers and their tunability using varactor diodes. All studies in this section considers lossless impedances.

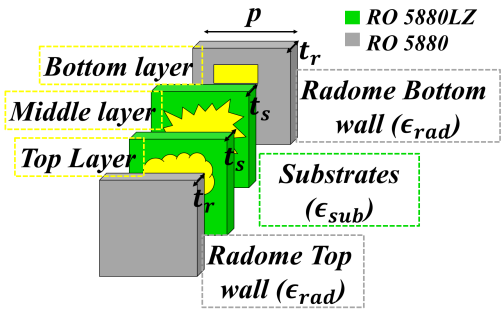

Figure 4.1 Representation of a three-layer metasurface UC.

4.2.1 Impedance Requirements

The analysis of this section relies on the two-port network methodology proposed in previous work [51, 59, 82]. Fig. 4.2 depicts the network representing the UC. The transmission lines represent the substrates, which are defined by their thicknesses (t_{diel}), their characteristic impedances (η_{diel}), and their wavenumbers (k_{diel}) (the subscript *diel* stands for either the radome or the substrates). On the other hand, the metallic layers are defined by their impedances ($Z_{top,mid,bot}$). Finally, the input and output impedances (η_0) equal 377 Ω. The ABCD parameters of each element are given in (4.1) and (4.2) [83]. This method is a simplification and neglects the high order modes which are attenuated by 2.23 dB/mm in free space. This leads to an attenuation of more than 11 dB in the substrate between the layers.

The cascade of all the ABCD parameters gives the overall network representation as shown in (4.3). This expression facilitates the calculation of the theoretical UC transmission coefficient by inserting (4.3) in (4.4). This parameter serves to characterize the anisotropic UC, which has identical top and bottom layers. This configuration is usual for beam tilting applications

using the phase gradient methodology [58]. Fig. 4.3 shows the transmission map as a function of the layers' reactances. The magnitude plot (Fig. 4.3a) shows three transmission regions with transmission levels above -3.5 dB. However, the phase map in Fig. 4.3b shows that the 360^o phase coverage can be achieved using reactance combinations of the two regions identified by the dashed lines. The required reactances are $-240\ \Omega \leq X_{top/bot} \leq 0\ \Omega$, and $-80\ \Omega \leq X_{mid} \leq 80\ \Omega$.

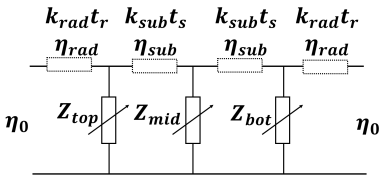

Figure 4.2 Network representation of the proposed three-layer UC.

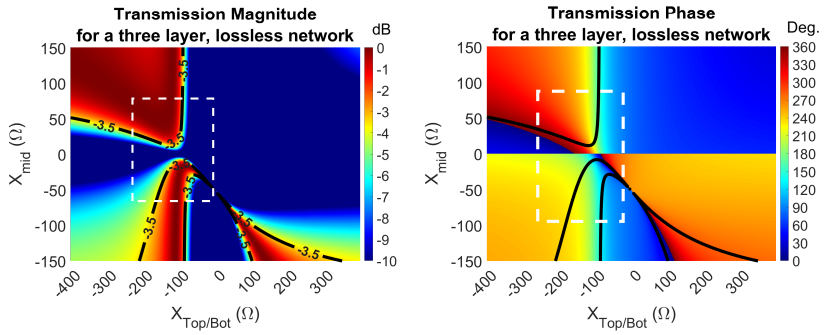

(a) (b)

Figure 4.3 Transmission of a three-layer, lossless network: (a) magnitude, and (b) phase.

$$M_{diel} = \begin{pmatrix} \alpha_{diel} & \beta_{diel} \\ \gamma_{diel} & \alpha_{diel} \end{pmatrix} = \begin{pmatrix} cos(k_{diel}t_{diel}) & j\eta_{diel}sin(k_{diel}t_{diel}) \\ jsin(k_{diel}t_{diel})/\eta_{diel} & cos(k_{diel}t_{diel}) \end{pmatrix} \tag{4.1}$$

$$M_{Y_n} = \begin{pmatrix} 1 & 0 \\ 1/Z_n & 1 \end{pmatrix} \tag{4.2}$$

$$M_{3lay} = M_{rad}M_{Ytop}M_{sub}M_{Ymid}M_{sub}M_{Ybot}M_{rad} \tag{4.3}$$

$$S_{21} = \frac{2}{A_{3lay} + B_{3lay}/\eta_0 + C_{3lay}\eta_0 + D_{3lay}} \tag{4.4}$$

The next study case is an asymmetric UC (i.e. different top and bottom layers) for synthesizing a bianisotropic metasurface [51, 56, 57]. In this methodology one considers a material modelled as an infinitely thin sheet with electric and magnetic currents that are associated to their respective electric impedance (Z_{se}) and magnetic admittance (Y_{sm}) (Fig. Fig. 4.4a). The particularity of this methodology is the introduction of the magnetoelectric coupling (K_{em}), which establishes a correlation between the electric and magnetic fields. The process described in [51] shows how to relate these three physical parameters of a bianisotorpic surface, to the Z-parameters of an equivalent three-layer metasurface using (4.5). The three-layer metasurface is represented by the red, black, and blue dash lines in Fig. 4.4a. Each layer has an impedance that is calculated from the Z-parameters. The impedances Z_{top}, Z_{mid}, and Z_{bot} are represented by the dash lines in Fig. 4.4a.

The case of study in this chapter aims to refract an normal transverse electric (TE) wave to 58°. In such a case, the required reactance for each layer is depicted in Fig. 4.4b. Each subplot corresponds to a different layer, and the x-axis illustrates the length of the hypothetical metasurface. The result show that the reactance distribution along the length is periodic. Moreover, the reactance distribution requires values within a range of various hundreds of Ohms. However, because the UCs discretize the reactances one can consider a smaller range that allows the implementation of the metasurface. In this case, the ranges for different layers are highlighted in Fig. 4.4b, requiring that $-200\ \Omega \leq X_{top} \leq 0\ \Omega$, $-80\ \Omega \leq X_{mid} \leq 80\ \Omega$, and $-200\ \Omega \leq X_{bot} \leq 0\ \Omega$. These values are within the same range of the first case of study. Thereby, the layer's reactances must be tunable within the ranges of $-200\ \Omega \leq X_{top/bot} \leq 0\ \Omega$, and $-80\ \Omega \leq X_{mid} \leq 80\ \Omega$ to allow the implementation of the metasurface in both cases.

$$\begin{pmatrix} Z_{11} & Z_{12} \\ Z_{22} & Z_{22} \end{pmatrix} = \frac{1}{4Y_{sm}} \begin{pmatrix} 4Y_{sm}Z_{se} + (1+2K_{em})^2 & 4Y_{sm}Z_{se} - (1+2K_{em})(1-2K_{em}) \\ 4Y_{sm}Z_{se} - (1+2K_{em})(1-2K_{em}) & 4Y_{sm}Z_{se} + (1-2K_{em})^2 \end{pmatrix} \tag{4.5}$$

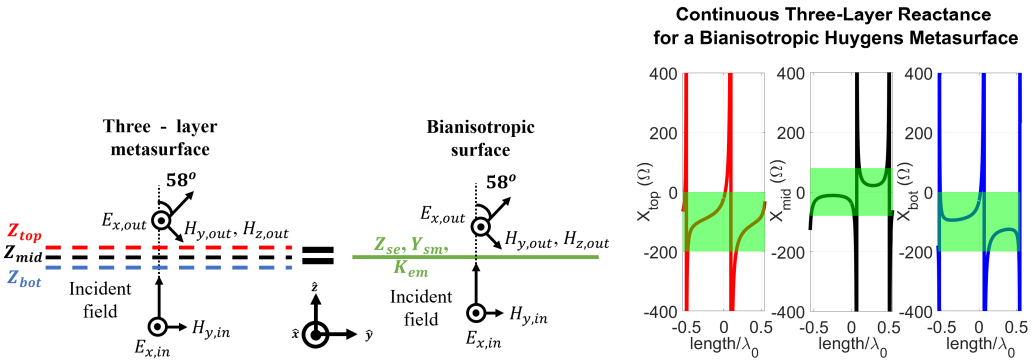

(a) (b)

Figure 4.4 Bianisotropic metasurface synthesis for wide refraction angles, (a) equivalence between a three-layer metasurface and a bianisotropic surface for wide refraction, and (b) continuous three-layer reactances for the metasurface illustrated in (a).

4.2.2 Single-Layer Characterization

With the reactances defined, the next step is designing each layer. The ABCD parameters presented in (4.3) may be used for characterization purposes, while considering only the layer of interest. This work explores the use of variable capacitors (varactor diodes).

Single-resonant geometries

We first consider a regular dogbone loaded with a varactor in the top layer, as shown in Fig. 4.5a. This geometry is single-resonant as show in Fig. 4.5b. In the frequency of resonance, the currents are concentrated in the vertical leg flowing form the top to the bottom horizontal leg. This physical behavior corresponds to an electric dipole. In this state, all the incident energy is reflected because the layer's reactance is zero, as illustrated in Fig. 4.5c. This state represents a transition point between capacitive and inductive reactances. Fig. 4.5c also shows how the varactor diode controls the reflection behavior, shifting it in frequency and thereby changing the reactance. Fig. 4.5d illustrates the reactance variation at 2.45 GHz. It shows that the regular dogbone requires a large variation in the capacitance of the varactor to achieve the previously defined reactance tunability. Nonetheless, varactors with these characteristics and low losses (below 1 Ω) are not easily found in the market. For example, [84] shows a non-exhaustive list of varactor diodes. From this list, the reference SMV 1275 has a capacitance range between 0.83 pF and 4.74 pF and a parasitic resistance of 0.8 Ω. However, this varactor diode reduces the reactance range of the regular dogbone to 100 Ω, as is marked in Fig. 4.5d. This constraint proves that single-resonant geometries do

not cover the required reactance ranges.

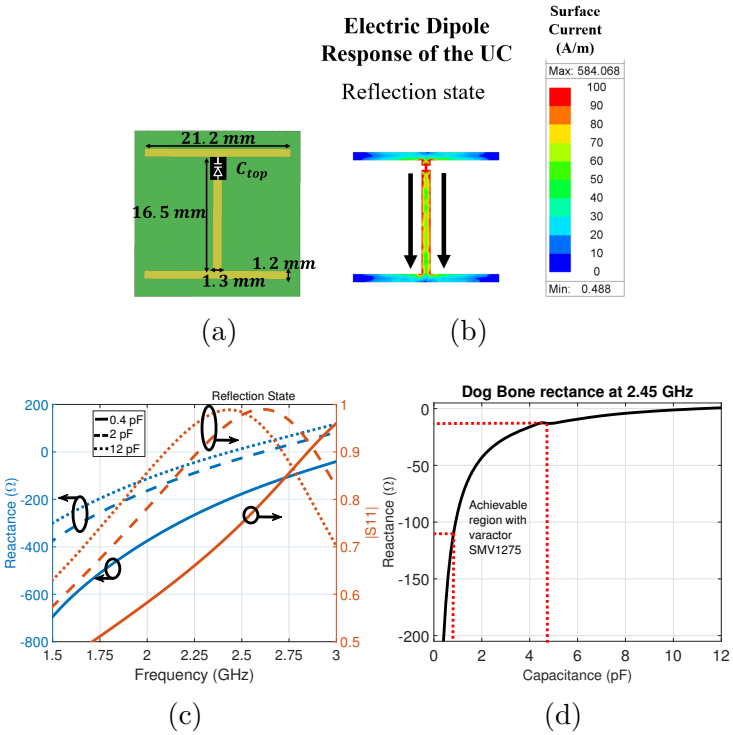

Figure 4.5 Regular dogbone as top layer (radomes and other substrates hidden for illustration), (a) geometry, (b) electric currents at 2.56 GHz with $C_{top} = 2$ pF, (c) S11 magnitude and reactance for different varactors, and (d) reactance at 2.45 GHz as a function of the varactor capacitance.

Dual-resonant geometries

Adding a meander line to the regular dogbone (Fig. 4.6a) splits the geometry into two electric dipoles (Fig. 4.6b). The first dipole appears in state 1, demonstrating a resonance at 1.9 GHz, induced between the bottom horizontal leg and the meander line. The second dipole is induced between the top horizontal leg and the meander line (state 3 as labeled in Fig. 4.6b), and can be shifted between 2.49 GHz and 2.9 GHz by changing the capacitance of the varactor diode. Both states are resonances, with corresponding reactances of zero (Fig. 4.6c). State 2 occurs between these two resonances, wherein the reactance increases to hundreds of ohms. This abrupt change in reactance over a small frequency range enhances reactance tunability. A magnified view near state 3 in the frequency range of interest (Fig. 4.6d) shows that the varactor tunes the reactance within a range of 250 Ω at 2.45 GHz. This new range presents an enhancement of 162 Ω (274%) compared to the regular dogbone, as shown in Fig. 4.9. Although the current distributions illustrated in Fig. 4.6b correspond to the case

when the varactor diode equals 2 pF, the current distributions are valid for any other value. Indeed, the three states are always present and the states 1 and 3 always occur at 1.9 GHz and 2.05 GHz respectively. On the other side, just the state 3 is shifted as the capacitance changes, but the current distribution in the frequency of resonance remains equal.

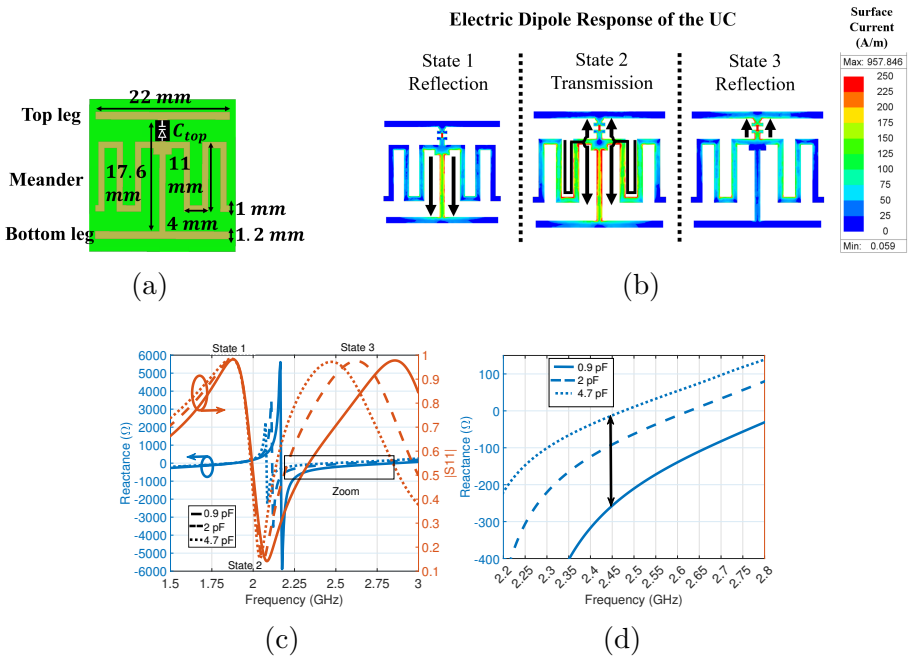

Figure 4.6 Meander dogbone as top layer (radomes and other substrates hidden for illustration), (a) geometry, (b) electric currents, (c) S_{11} magnitude (right axis) and reactance (left axis) plotted versus frequency, and (d) a zoomed-in view of reactance variations with frequency.

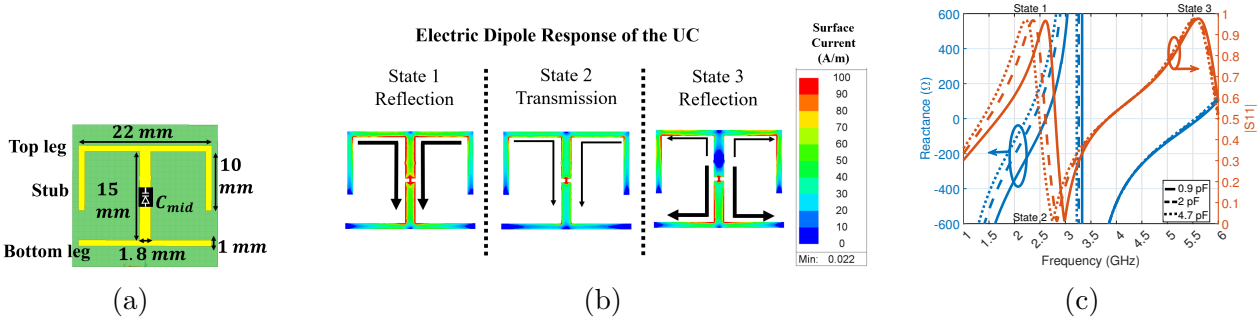

Figure 4.7 T dogbone as middle layer (radomes and other substrates hidden for illustration), (a) geometry, (b) electric currents, and (c) S_{11} magnitude (right axis) and the extracted reactance (left axis) plotted versus frequency.

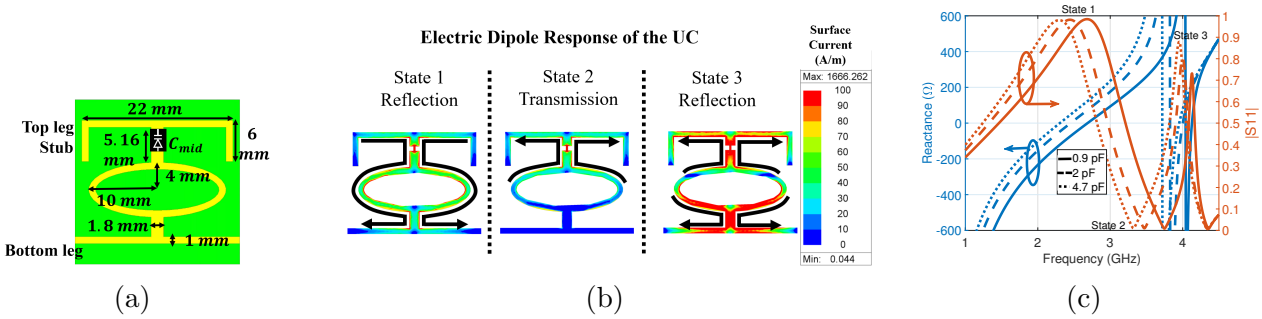

Figure 4.8 T-ring dogbone as middle layer (radomes and other substrates hidden for illustration), (a) geometry, (b) electric currents, and (c) S_{11} magnitude (right axis) and the extracted reactance (left axis) plotted versus frequency.

While the meander dogbone satisfies the top and bottom reactance requirements, the middle layer requires a different design. Two possible geometries are the T dogbone (Fig. 4.7a) and the T-ring dogbone (Fig. 4.8a). The two geometries are proposed to allow comparative studies of the inter-layer coupling effects, as will be explained in the next section. It must be noted that these geometries have various dipole resonances that lead to the same three states as for the meander dogbone as shown in Figs. 4.7b and 4.8b. These figures show the current distribution when the varactor diode equals 2 pF, but the three cases are identical for any other capacitance.

Oppositely to the meander dogbone, the varactor diode in the T and T-ring dogbones controls the state 1 as shown in Figs. 4.7c and 4.8c. The main difference between these two geometries is the proximity in frequency between states 1 and 2 for the T dogbone (~ 0.6 GHz) compared to the T-ring dogbone (~ 1.1 GHz). This difference causes a smoother change in the reactance for the T-ring dogbone. Thereby, at 2.45 GHz, the reactance tunability of the T dogbone is 166 Ω, while for the T-ring dogbone this value is 130 Ω as shown in Fig. 4.9. It can be observed that the two layers shift between inductive and capacitive reactances and that from the single-layer perspective, only the T dogbone accomplishes the middle layer reactance requirements. However, this behavior changes when the inter-layer coupling effects are included, as will be shown in the next section.

4.3 Impact of the inter-layer coupling on the reactance

This section studies the impact of inter-layer coupling on the reactances of different layers upon integration. The methodology to characterize the coupling comprises running full wave simulations of the complete UC and then calculating the layers' reactances using (4.6a) and

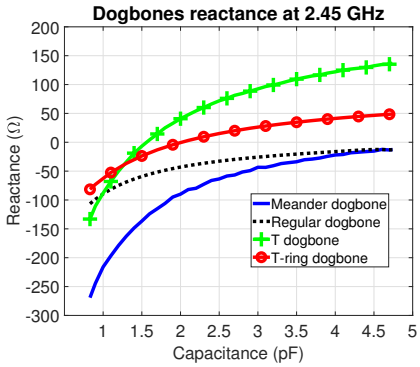

Figure 4.9 Comparison of reactances of various dogbones elements.

(4.6b). These equations come from (4.3). It should be noted that these formulation is an approximation since the inter-layer coupling is intrinsically considered in the full-wave simulations, but the ABCD parameters consider only the first order mode. The high order modes have a decay of more than 11 dB in the substrates between the layers, and its impact is neglected by the ABCD formulation. Additionally, this study considers identical top and bottom layers for practicality which is not as versatile as bianisotropic UCs, but has a simpler biasing network. Two UC families are explored: one by cascading Meander-T-Meander dogbones (Fig. 4.10a) and another one by cascading Meander-T_{ring}-Meander dogbones (Fig. 4.11a)).

$$Z_{mid} = \left[\frac{-A\alpha_r\beta_r + B\alpha_r^2 + C\beta_r^2 - D\alpha_r\beta_r + 4\alpha_r^2\beta_r\gamma_r\alpha_s\beta_s - 2\beta_r^2\gamma_r^2\alpha_s\beta_s - 2\alpha_r^4\alpha_s\beta_s}{\beta_s^2(\alpha_r^2 - \beta_r\gamma_r)^2}\right]^{-1} \tag{4.6a}$$

$$Z_{top} = Z_{bot} = \left[-\frac{\beta_r\gamma_r\left(-A + \beta_r\gamma_r\alpha_s^2 + \beta_r\gamma_r\beta_s\gamma_s + Z_{mid}^{-1}\beta_r\gamma_r\alpha_s\beta_s\right) + \alpha_r\left(B\gamma_r + C\beta_r\right)}{\beta_s\left(\alpha_r^2 - \beta_r\gamma_r\right)^2\left(2\alpha_s + Z_{mid}^{-1}\beta_s\right)}\right.$$
$$\left.+\frac{-\alpha_r^2\left(D + 2\beta_r\gamma_r\alpha_s^2 + 2\beta_r\gamma_r\beta_s\gamma_s + 2Z_{mid}^{-1}\beta_r\gamma_r\alpha_s\beta_s\right) + \alpha_r^4\left(\alpha_s^2 + \beta_s\gamma_s + Z_{mid}^{-1}\alpha_s\beta_s\right)}{\beta_s\left(\alpha_r^2 - \beta_r\gamma_r\right)^2\left(2\alpha_s + Z_{mid}^{-1}\beta_s\right)}\right]^{-1} \tag{4.6b}$$

4.3.1 Family 1: Meander-T-Meander Dogbones

Fig. 4.10b shows the map of the top/bottom layers' (meander dogbones) reactances at 2.45 GHz when the layers are integrated and mutual coupling effects are present. It can be

observed that the middle layer does not considerably impact the top/bottom reactance values. Hence, the main impact here comes from the mutual coupling effects between the top and bottom layers, which leads to a decrease of 40 Ω in the reactance tunability range compared to the single-layer calculations. The dispersive reactance in Fig. 4.10d gives insight into the reason for this effect. It shows that the reactance keeps the three (previously defined) states of the single-layer design but is shifted in frequency. This shift causes a slightly less abrupt reactance change at 2.45 GHz, which explains the tunability loss of 40 Ω. Nonetheless, this impact is negligible as the reactance remains within the required range defined in section 4.2.

Fig. 4.10c depicts the reactance map of the middle layer (T dogbone) at 2.45 GHz. In this case, the inter-layer coupling has an important impact on the reactance. The dashed lines outline a region where the middle layer loses its tunability due to the mutual coupling effects. Outside this region, the layer is tunable only within a limited range. Additionally, the reactance becomes a function of the top and bottom layers' reactances, and the tunability range is under that calculated for the single-layer design. Fig. 4.10e shows the dispersive reactance of the T dogbone. It is observed that the coupling distorts the curve by introducing random peaks, which cause abnormal dispersive behavior. Hence, the three states observed in the single-layer design vanish. However, the new behavior is usable under certain conditions. The magnified view around the frequency of interest in Fig. 4.10f shows that the middle layer follows the pattern of the single-layer design over a small range of frequency. However, the tunability range is limited to ± 50 Ω. This range is below the required range for bianisotropic metasurface design. Therefore, exploring another geometry that allows for covering the rest of the reactance range is necessary.

4.3.2 Family 2: Meander-T_{ring}-Meander Dogbones

This UC retains the same parameters as the UC of family 1, except for utilizing a new middle layer geometry, as shown in Fig. 4.11a. The reactances of the top and bottom layers (meander dogbones) are equal to those of the UC of family 1, as illustrated in Figs. 4.11b and 4.11d. In contrast, the effect of the inter-layer coupling on the reactance of the middle layer (T-ring dogbone) has changed significantly compared to the respective behavior of family 1. The middle-layer reactance map in Fig. 4.11c shows that the capacitances of the top and bottom varactors only slightly impact the reactance of the middle layer. In fact, the middle layer's reactance only depends on its respective varactor's capacitance. However, the inter-layer coupling effects still impact the tunability range compared to that presented for the single-layer case. Fig. 4.11e compares the reactance of the middle layer with and without coupling across the frequency range. It is observed that in the presence of mutual coupling,

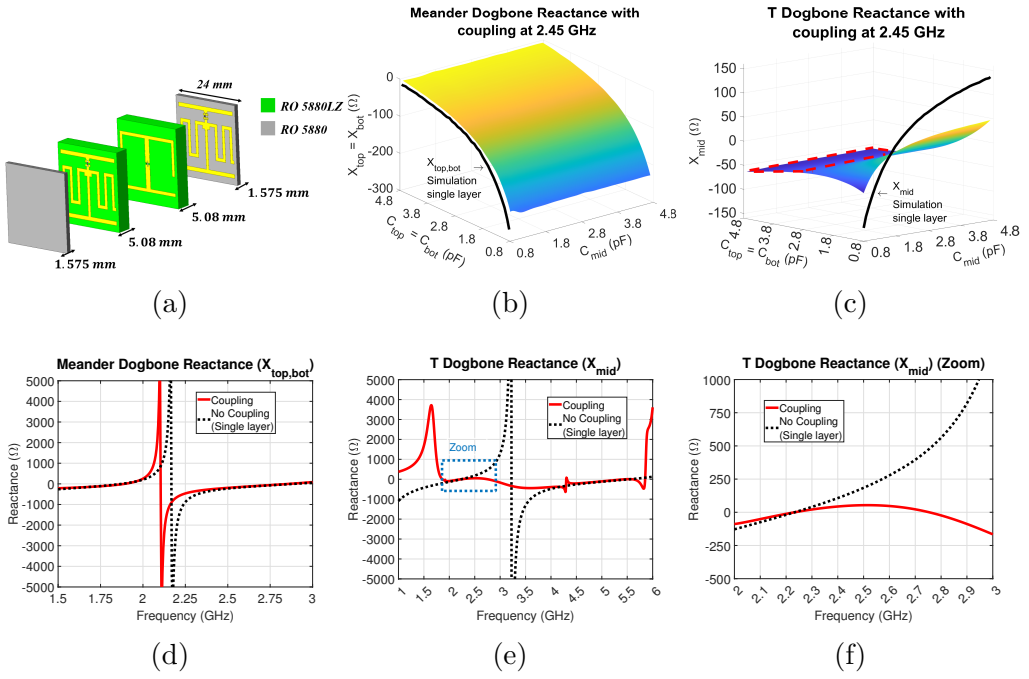

Figure 4.10 Meander-T-Meander dogbone UC (a) geometry, (b) reactance at 2.45 GHz for the top/bottom layers, and (c) reactance at 2.45 GHz for the middle layer. Dispersive reactances using $C_{top,bot} = 0.83$ pF, and $C_{mid} = 4.74$ pF for (d) top/bottom layers, (e) middle layer, and (f) middle layer with magnified view in frequency.

the three states of the single-layer element disappear, and various abrupt peaks appear. One of the peaks causes a quick reactance variation near the frequency of interest (2.45 GHz), as shown in Fig. 4.11f. In this frequency range, the reactance varies from capacitive to inductive, while it remains close to the single-layer values before this peak. The difference between the reactance map of the middle layer, and the reactance curve for the single-layer counterpart in Fig. 4.11c occurs because the reactance is tuned close to the peak. The plot shows that the peak shifts towards 2.45 GHz as C_{mid} increases. This shift explains the larger range of reactance tunability compared to the single-layer calculations. This explanation is valid in the smooth region of the map. In contrast, the region outlined by the dashed lines presents abrupt variations that make the reactance tunability range unstable, and the UC lossy. Hence, the UC of the family 2 is utilized outside the outlined region, and its tunability range is between -70 Ω and 82 Ω, which is close to the established requirement.

The calculations in this section show that the single-layer analysis gives a good approximation for the top and bottom layers, but not for the middle layer, which becomes unpredictable without a detailed analysis of the mutual coupling effects. Consequently, two UC families are presented, each with a different impact of mutual coupling effects on the middle layer.

The results show that the UC of family 2 has a middle layer (T-ring dogbone) easily tunable as its reactance depends only on the capacitance of the middle-layer varactor. However, it also has an unstable, lossy region. In such case, the UC of family 1 is more suitable, even though its tunability range is somewhat limited. The following section presents experimental validations of all reactance characterizations, while Section 4.5 gives more details on the UC selection for the design of the supercell.

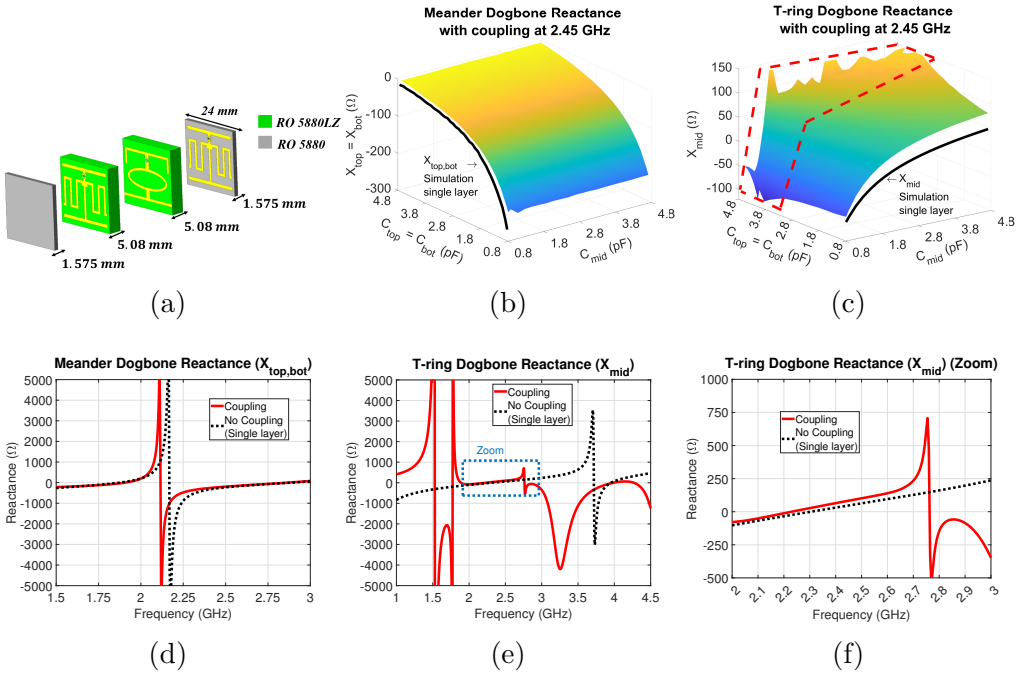

Figure 4.11 Meander-T-ring-Meander dogbone UC (a) geometry, (b) reactance at 2.45 GHz for the top/bottom layers, and (c) reactance at 2.45 GHz for the middle layer. Dispersive reactances using $C_{top,bot} = 0.83$ pF, and $C_{mid} = 4.74$ pF for (d) top/bottom layers, (e) middle layer, and (f) middle layer with magnified view in frequency.

4.4 Measurement of the unit cell

The reactances of the proposed UCs are validated by waveguide measurements. This methodology is widely used in the literature [50, 61, 62, 85]. Nonetheless, in most cases, only the amplitude and phase control are characterized. In contrast, this work focuses on characterizing the reactance of the UC layers using the ABCD parameters (4.1) - (4.3) with the respective wavenumber (4.7a) and impedances (4.7b) for a material in a waveguide.

The profile of the waveguide is illustrated in Fig. 4.12a, wherein the coaxial to waveguide transition corresponds to the aperture WR340. Two steps are cascaded as transitions to

match the waveguide aperture to the UC samples. Fig. 4.12b shows the S-parameters from simulations and measurements. The ports in the simulations are in the aperture of the WR340 section. For this reason, the effect of the coax to waveguide transition was de-embedded in the measurements. The results show well agreement and a reflection coefficient magnitude of less than -20 dB.

The UC samples consist of four columns and two rows (96 mm × 48 mm). Therefore, the apertures of the two steps measure 90.12 mm × 48 mm and 96 mm × 48 mm, respectively. The transmission of the fundamental mode in the complete waveguide falls in the frequency range 1.74 GHz to 3.13 GHz. The lower frequency corresponds to the cutoff frequency of the aperture WR340 (f_{cut}), and the upper limit indicates the frequency where the second propagating mode appears in the step 2.

A picture of the fabricated UC samples is depicted in Fig. 4.13a. The UCs are connected through RF resistor chokes of 1 $k\Omega$, and have slotted walls on the sides to guarantee electric continuity within the walls of the waveguide. The samples are assembled in a holder (Figs. 4.13b and 4.13c) that is screwed in the waveguide. The complete measurement setup is shown in Fig. 4.13e. Likewise, the biasing network is detailed in Fig. 4.13d. This illustration shows that the samples contain additional chokes of 100 $k\Omega$ between the DC voltage source and the geometries (in the bottom of the boards). This chokes cause a drop in the voltage from the source to the geometries as shown in Table 4.1. In contrast, the 1 $k\Omega$ chokes have negligible effect in the biasing voltage and all the geometries are equally biased.

$$\beta_{diel} = \frac{\omega\sqrt{\varepsilon_r}}{c_0}\sqrt{1-\left(\frac{f_{cut}}{f}\right)^2} \tag{4.7a}$$

$$\eta_{diel} = \frac{\eta_0}{\sqrt{\varepsilon_r} \quad * \quad \sqrt{1-\left(\frac{f_{cut}}{f}\right)^2}} \tag{4.7b}$$

4.4.1 Single-Layer Characterization

This characterization consists of keeping only one of the geometries to extract its reactance from the measured S-parameters. Fig. 4.14 shows the reactances measured for each of the layers compared to their two simulated counterparts obtained using Floquet and waveguide boundary conditions. The samples are fabricated in the facilities of the Poly-Grames Research Center of Polytechnique Montréal. As in any fabrication, the uncertainties lead to some differences between the measured and simulated data. In this case, the reactances predicted

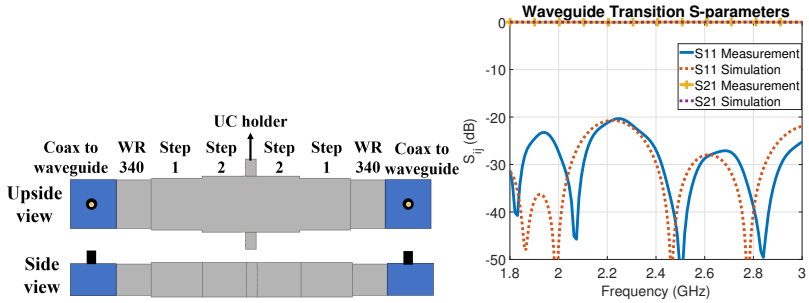

(a) (b)

Figure 4.12 Waveguide setup, (a) illustration of the profile, and (b) simulated and measured S-parameters.

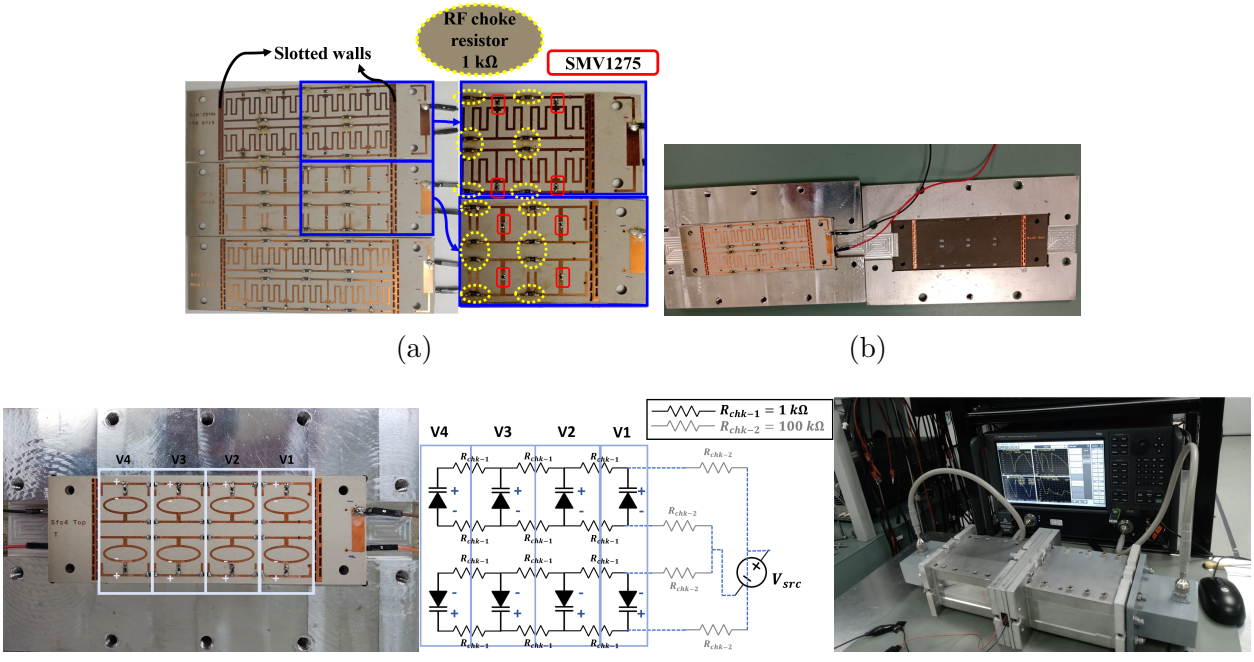

(a) (b)

(c) (d) (e)

Figure 4.13 (a) Photo of the meander and T dogbone samples, (b) top meander dogbone in the UC holder, (c) T-ring dogbone in the UC holder, (d) schematic of biasing network, and (e) the complete measurement setup.

by the simulations at 2.45 GHz shift to 2.58 GHz in the measurements, as shown in Fig. 4.14. The results show that the predicted reactances are in agreement with the measurements, proving the functionality of the dual-resonant geometries to increase the reactance tunability.

Table 4.1 DC biasing voltage in the varactor diodes of the samples

V_{src} (v)	V1 (v)	V2 (v)	V3 (v)	V4 (v)
0.5	0.48	0.48	0.48	0.48
1	0.97	0.97	0.97	0.97
2	1.94	1.94	1.94	1.94
4	3.9	3.9	3.9	3.9
8	7.79	7.78	7.78	7.78
16	15.58	15.58	15.57	15.57
16.4	15.97	15.97	15.96	15.96

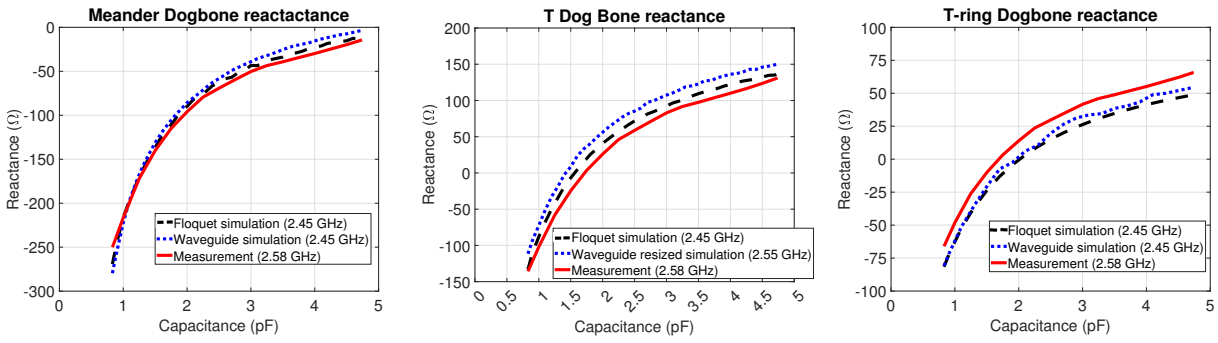

(a) (b) (c)

Figure 4.14 Measurements of the single-layer reactances (a) meander dogbone, (b) T-dogbone, and (c) T-ring dogbone.

4.4.2 Inter-Layer Coupling

Studies in the previous sections show that each layer has a broad and tunable reactance. Nonetheless, the complete characterization of the UC requires considering the inter-layer coupling effects. One method for doing this is measuring in the waveguide the S-parameters of the UC with all the layers and de-embedding the impedance using ABCD parameters. The use of S to ABCE-parameters was also used in [86] and gives unique equations for each layer while intrinsically considering the coupling effects. For the proposed UC, the equations are given by (4.6a) and (4.6b), which are deduced from (4.8). These equations consider identical top and bottom layers for simplicity.

$$M_{rad}^{-1} M_{3lay} M_{rad}^{-1} = M_{Ytop} M_{sub} M_{Ymid} M_{sub} M_{Ybot} \tag{4.8}$$

Two families of UCs are characterized. Family 1 has the T dogbone as middle layer and family 2 uses the T-ring dogbone as middle layer. In both cases, the meander dogbone is

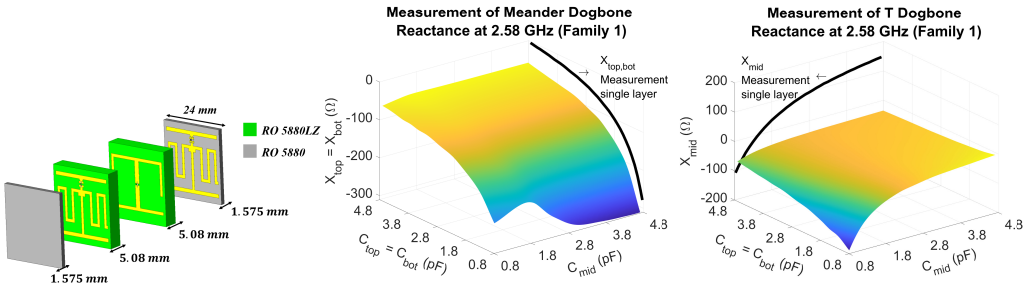

(a) (b) (c)

Figure 4.15 (a) UC of family 1, reactances at 2.58 GHz considering the inter-layer coupling: (b) Top and bottom layers (meander dogbone in the UC of family 1), and (c) middle layer (T dogbone in UC from family 1).

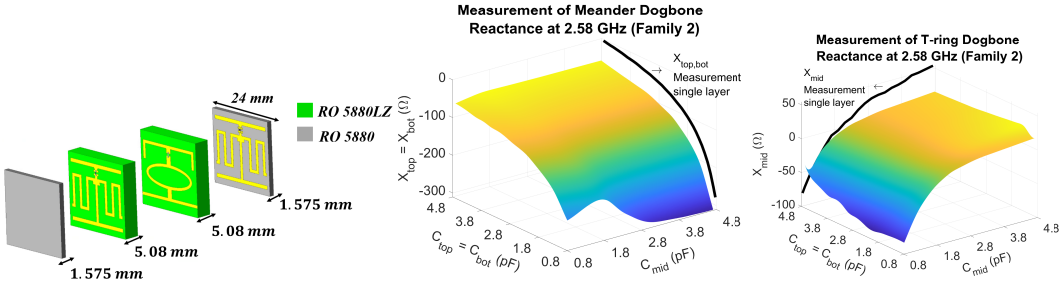

(a) (b) (c)

Figure 4.16 (a) UC of family 2, reactances at 2.58 GHz considering the inter-layer coupling: (b) Top and bottom layers (meander dogbone in the UC of family 2), and (c) middle layer (T-ring dogbone in UC from family 2)

placed as top and bottom layers. Figs. 4.15a and 4.16a show these families, while Figs. 4.15b, 4.15c, 4.16b and 4.16c present their reactance maps at 2.58 GHz, plotted against the layers' capacitances. The maps are compared to the respective single-layer measurement. The main impacts of the inter-layer coupling effect are listed below.

1. The meander dogbone performs identically in the two families. The respective map is depicted in Figs. 4.15b and 4.16b. The reactance is mostly independent of the middle layer. However, the tunability range decreases by 20 Ω compared to the respective single-layer prediction. Moreover, the reactance has an offset towards more capacitive values.

2. The T dogbone losses its reactance tunability in most of the cases. Fig. 4.15c shows that the reactance remains close to -50 Ω with exception of a small region close to

the lowest capacitances. However, the tunability depends on both the top/bottom and middle capacitances. This co-dependence indicates a strong coupling of the meander dogbone towards the T dogbone.

3. The T-ring dogbone retrieves the tunability of the middle layer, and it is independent of the other layers, as shown in Fig. 4.16c. However, the range of tunability decreases by 34 Ω.

These three statements show that the meander dogbone remains close to the reactance requirements established in Section 4.2.1 for the top and bottom layers. On the other hand, the T-ring dogbone covers the range between ± 50 Ω, and the T dogbone can cover values below -50 Ω. The addition of the two ranges is close to the conditions defined for the middle layer. Consequently, it serves to design the proposed Huygens metasurface as shown in the next section.

Effect of resistances in the transmission

The two main sources of losses in the experimentation are the parasitic resistances of the varactor diodes, and by the choke resistances. While the resistance of the varactor diodes is usually underestimated in simulations (in this work it has been considered as 0.8 Ω, according to the datasheet), the $1k\Omega$ choke resistors are the main cause of the losses. Nonetheless, this chokes are necessary to avoid undesired resonances. Figs. 4.17 and 4.17 show the transmission coefficient in the waveguide for the two families of UCs. The result shows that under metallic boundary conditions, and using choke resistors, the UC of family 1 covers around 330° with transmission better than -8 dB. On the other side, the UC of the family 2 does not have a good transmission.

A study of the transmission under Floquet boundary conditions, and without chokes is presented in the section 4.5.

4.5 Supercell Simulations of the reconfigurable Huygens metasurface

This section presents simulations of a supercell of the Huygens metasurface. First, the UCs are tuned to implement a bianisotropic metasurface, as illustrated in Fig. 4.4a. Next, the capacitance of the varactors is reconfigured to investigate an anisotropic UC for beam tilting through a phase-gradient design approach. In both cases, the UCs are designed according to the previously shown reactance characterizations. These methodologies are rarely integrated in the literature due to the extensive reactance reconfigurability required by the UCs.

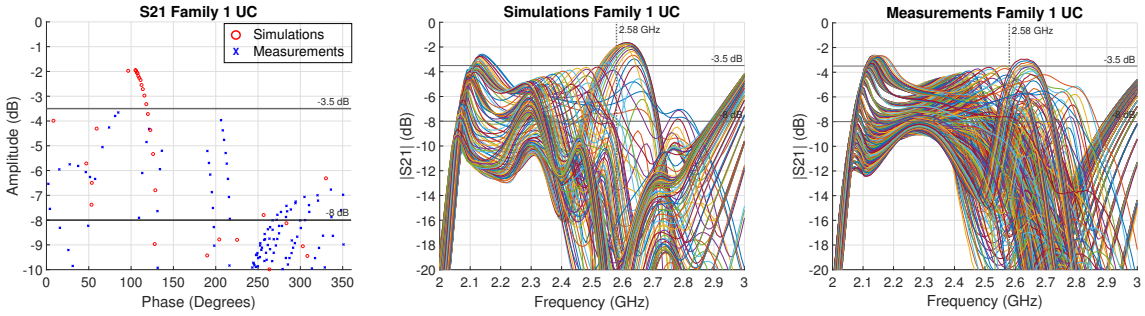

(a) (b) (c)

Figure 4.17 Transmission coefficient of family 1 UC (a) at 2.58 GHz, magnitude along the frequency (b) simulations, and (c) measurements.

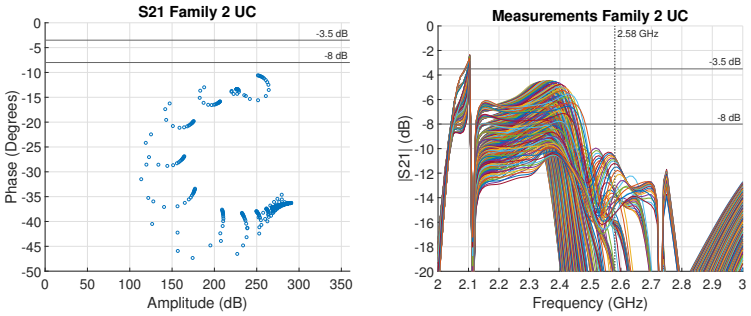

(a) (b)

Figure 4.18 Transmission coefficient measurements of family 2 UC (a) at 2.58 GHz, and (b) magnitude along the frequency.

However, the proposed dual-resonant UC families meet these requirements.

In both scenarios, the simulations are conducted on a supercell comprising six UCs: four from family 2 and two from family 1 as depicted in Fig. 4.19. The order of the families is chosen to optimize the bianisotropic performance. The simulations successfully demonstrate the proposed bianisotropic and beam tilting capabilities of the metasurface supercell.

4.5.1 Bianisotropic Metasurface Design: Wide-Angle Refraction

Classical methodologies for beam tilting, as phase gradient, are limited by the impedance mismatch for refracting wide-angles. This constraint can be overcome by bianisotropic metasurfaces. As explained in Section 4.2.1, a metasurface is considered as bianisotropic when its synthesis starts by modelling a bianisotropic surface (i.e. with electric impedance, magnetic admittance, and magnetoelectric coupling) to the Z-parameters of a three-layer metasurface

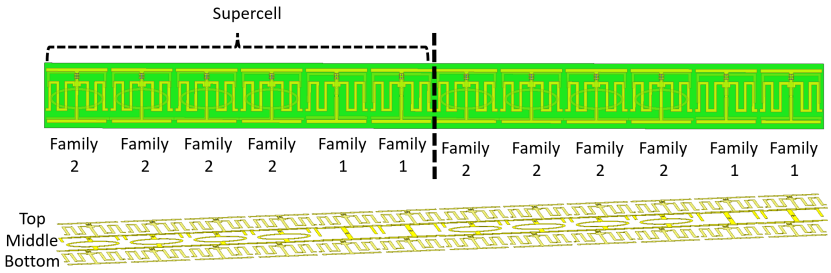

Figure 4.19 Supercell representing a Huygens metasurface.

using (4.5). Such a metasurface is capable of matching normal incident waves to wide-angle refraction, as has been proved in [51,56,57]. The case of study in this Chapter is to configure the proposed supercell as bianisotropic to refract a normally incident TE wave to 58.25° (Fig. 4.4a). This angle was selected because it corresponds to the first Floquet mode of the supercell [87], which makes can be calculated in full-wave simulations.

Fig. 4.20 shows the required continuous three-layer reactances and the achievable discretizations with the proposed UCs. The reactances are calculated from the conversion of the Z-parameters to ABCD-parameters using (4.1)-(4.3). The selection of the UCs to the discretization is done evaluating the two families and selecting the best one for each case. The result is the supercell shown in Fig. 4.19. The corresponding varactor capacitances of each UC are depicted in Table 4.2.

Table 4.2 Capacitances for the bianisotropic metasurface supercell

	Family 2				**Family 1**	
	UC1	**UC2**	**UC3**	**UC4**	**UC5**	**UC6**
C_{top} **(pF)**	1.08	1.41	0.99	1.82	1.8	2.1
C_{mid} **(pF)**	2.24	1.92	0.83	1.2	1.92	2.1
C_{bot} **(pF)**	0.93	1.51	2.21	1.75	2.15	4.7

While the achievable reactance discretization closely matches the ideal design, the generalized parameters (Gpar) are necessary to quantify the supercell's performance. While the Gpar are conceptually equal to the S-parameters, the Gpar allow to consider any impedance for the input and output. Therefore, Gpar allows for the study of the matching between any input and output medium impedances [51, 56, 57, 88]. Fig. 4.21 depicts the Gpar for the supercell, showing that the achieved phase aligns well with the ideal design values. However, the magnitude shows some differences, especially for UCs 3, 4, and 6.

For UC 3, the reactances of the top and bottom layers are mismatched by 8 Ω and 40 Ω respectively (Fig. 4.20), resulting in higher reflection. Although UC 4 has the required

reactances, it experiences high current flow in the varactor, leading to increased losses from the varactor due to parasitic ohmic effects and hence lower transmission level. Finally, UC 6 requires low top/bottom reactances (near $-20\ \Omega$). Figs. 4.6c and 4.6d show that lower reactances lead to higher reflection levels. This constraint explains the higher than expected reflection for UC 6. Even with these constraints, the Gpar values of the supercell are acceptable, with an average transmission of 0.8 and an average reflection of 0.13.

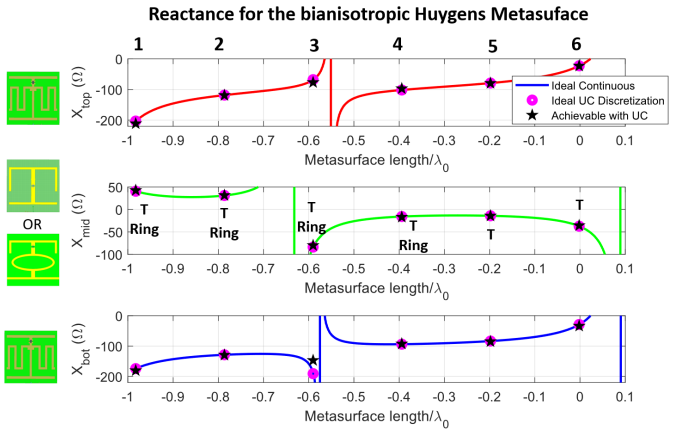

Figure 4.20 Layers' reactances for the proposed bianisotropic metasurface supercell.

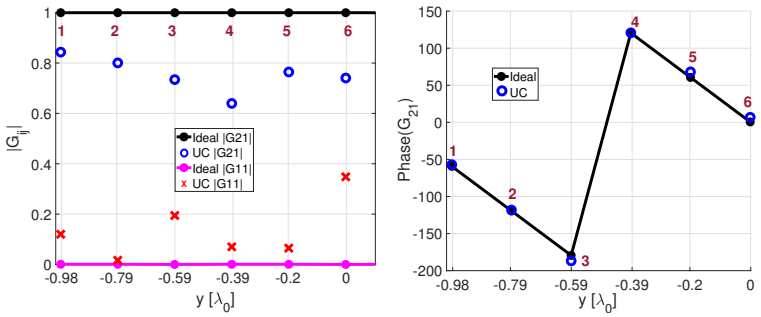

Figure 4.21 Generalized scattering parameters: (a) magnitude, and (b) phase.

Simulation of the supercell using Floquet boundary conditions and Floquet ports as excitation are shown in Fig. 4.22. Between 2.43 GHz and 2.46 GHz, all the excited modes are below -10 dB except for T_{-1}, corresponding to a beam tilting direction of 58.25^o. This confirms that the originally stated wide refraction angle is achieved following the proposed theoretical synthesis approach and practical UC limitations, and using fully reconfigurable UC models. T_{-1} remains above -4.7 dB in the bianisotropic region, measuring -3.93 dB at 2.45 GHz and a maximum of -3.73 dB at 2.44 GHz. The losses are studied in simulations by removing the

varactor's parasitic resistance. The results at 2.44 GHz (Fig. 4.22) show that the transmission levels for T_{-1} increase to -2.45 dB, but the undesired modes increase too. Nonetheless, they remain below -10 dB at all frequencies in the bianisotropic region. Another simulation replaces the dielectrics and conductors by lossless materials. In this case, T_{-1} increases to -1.59 dB, and R_0 increases from -20 dB to -11.24 dB. This high reflection is a consequence of the imperfections of UCs 3 and 6.

Studying the supercell efficiency provides a better insight into the losses and the performance of the proposed bianisotropic metasurface. Two efficiencies are considered in Fig. 4.22c: the total efficiency, defined as the ratio between the total scattered power and the total input power in the simulation, and the refraction efficiency, defined as the ratio between the power scattered in the desired direction and the total scattered power [51]. The total efficiency for the lossy UC is 75%, which means that the surface absorbs 25% of the incident power. This percentage is nearly the same as that in [51]. When the varactors' resistances are disabled in simulations, the efficiency rises to 88%. This increase reveals that the varactors absorb 13% of the energy. Finally, when the UC is lossless, all the energy is scattered. The refraction efficiency, on the other hand, remains above 75% in the bianisotropic region with a peak of 86% at 2.44 GHz in all cases. This high refraction efficiency of the proposed supercell proves its applicability for the design of reconfigurable bianisotropic Huygens metasurfaces. Indeed, Fig. 4.23 shows the transformation of the electric and magnetic fields using the proposed supercell to refract the wavefront towards the desired direction.

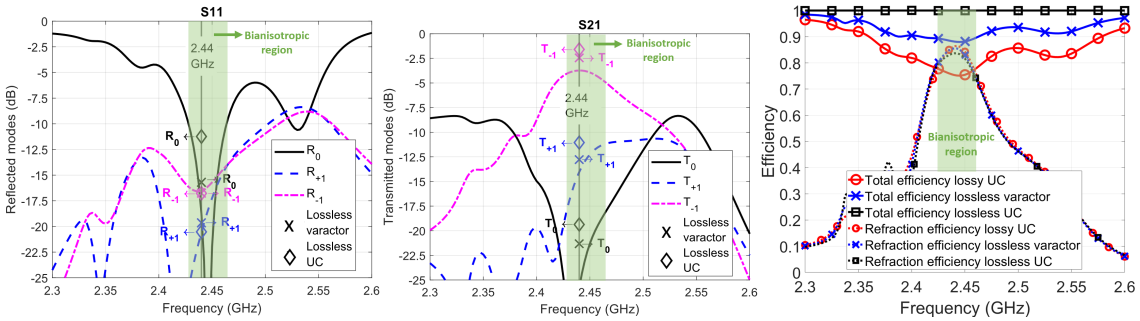

(a) (b) (c)

Figure 4.22 S-parameters of the supercell for all the Floquet modes (a) transmission, (b) reflection, and (c) efficiency. All parameters are compared with and without the effect of losses from the varactor diodes as well as dielectric/conductive losses.

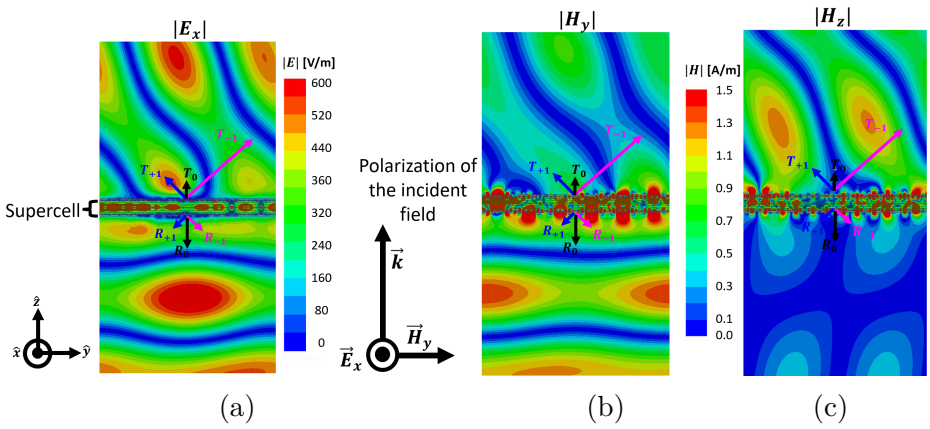

Figure 4.23 Simulated fields for the proposed supercell: (a) $\hat{x}$ component of the electric field, (b) $\hat{y}$ component of the magnetic field, and (c) $\hat{z}$ component of the magnetic field.

4.5.2 Anisotropic Metasurface Design: Beam Tilting Using the Phase Gradient Design Approach

The phase gradient methodology aims to use the controlability of the UCs to tilt the beam in different directions by creating a phase shift between adjacent elements. To implement phase-gradient metasurfaces, highly transmissive UCs covering a phase range near 360^o are required. For this design approach, the top and bottom layers are in identical states, whereas the assymetry between the top and bottom layers is a requirement for bianisotropic metasurface design, as was discussed in the preceding sections.

The calculated reactances in Section 4.3 allow the tuning of the two proposed families of UCs to obtain the required phase coverage. Fig. 4.24 shows the transmission coefficient of both UCs. It is must be noted that family 2 covers a transmission phase range of 250^o with an amplitude higher than -5 dB, and the UC from family 2 covers the desired 360^o phase range with an amplitude higher than -3 dB.

The simulation setup consists of a finite array of two supercells along the $\hat{y}$ axis. Perfect magnetic boundary conditions are applied in the $\hat{x}$ direction to emulate an infinite array along the $\hat{x}$ axis, while open boundary conditions are applied in the other directions. An illustration of the complete setup is shown in Fig. 4.25. The waveguide port exciting a planar wave is defined by the perfect magnetic walls (Fig. 4.25c) and the perfect electric conductor walls labelled in Fig. 4.25a. The phase of each UC is calculated using (4.9), wherein p stands for the UC periodicity, λ_0 is the wavelength at 2.45 GHz, and ϕ_{ref} is an arbitrary reference phase. Three beam tilting angles are tested: $\theta_{tilt} = 0^o$, 15^o, 30^o. The incident planar wave is induced by a waveguide with magnetic and electric walls, and the varactor capacitances for

each UC are listed in Table 4.3.

$$\Delta\phi = \frac{2\pi p}{\lambda_0} sin(\theta_{tilt}) + \phi_{ref} \tag{4.9}$$

The simulated near- and far-field behaviours are presented in Fig. 4.26. It is observed that the supercell successfully tilts the beam to the desired directions, proving the suitability of the proposed reconfigurable UC for the design of tunable phase-gradient metasurfaces.

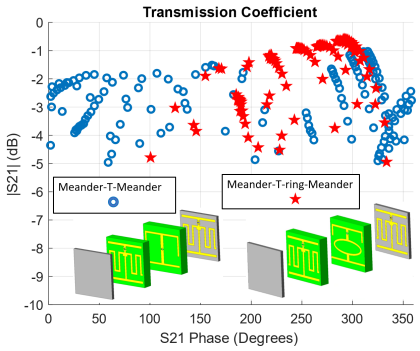

Figure 4.24 Transmission coverage of the two types of UCs.

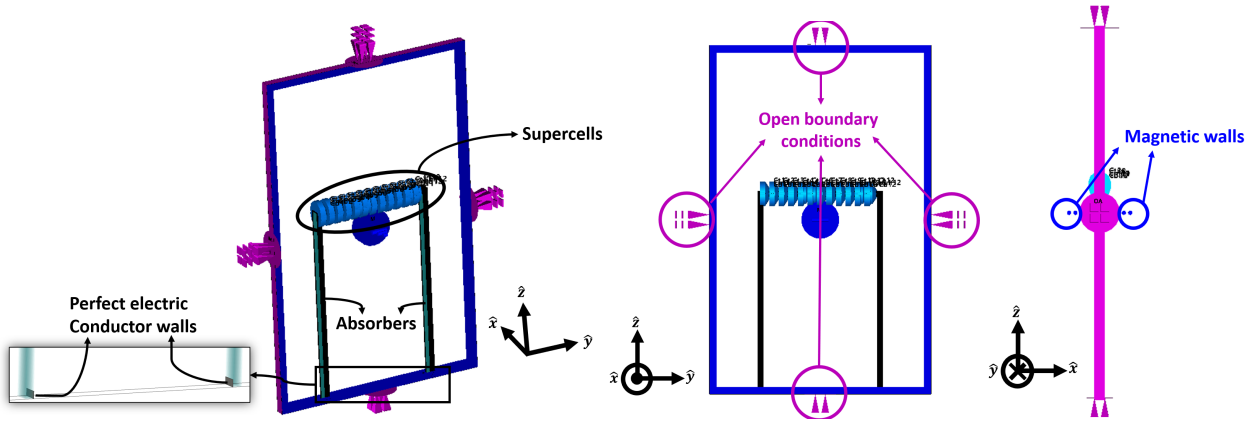

Figure 4.25 Simulation setup for the anisotropic supercell (a) isometric view, (b) view of the open boundary conditions, and (c) view of the magnetic walls boundary conditions.

4.6 Literature Comparison

Table 4.4 presents a comparative analysis of this study with previous works, focusing on the UC design and its applications. The table highlights that while most previous works

Table 4.3 Layers' capacitances for the phase gradient design method

		$\theta_{tilt} = 0^o$		$\theta_{tilt} = 15^o$		$\theta_{tilt} = 30^o$	
		C_{top} C_{bot} **(pF)**	C_{mid} **(pF)**	C_{top} C_{bot} **(pF)**	C_{mid} **(pF)**	C_{top} C_{bot} **(pF)**	C_{mid} **(pF)**
Fam 1	**UC1**	1.09	2.5	1.73	1.1	1.5	2.5
	UC2	1.09	2.5	1.7	0.9	1.29	2.3
	UC3	1.09	2.5	1.7	4.5	0.83	3.9
	UC4	1.09	2.5	1.43	0.83	0.84	2.1
Fam 2	**UC5**	1.29	4.3	1.21	0.83	3.83	1.9
	UC6	1.29	4.3	1.53	4.74	3.12	1.7
Fam 1	**UC7**	1.09	2.5	1.29	2.3	2.32	1.1
	UC8	1.09	2.5	1.1	2.7	2.01	1.1
	UC9	1.09	2.5	0.83	3.9	1.87	0.9
	UC10	1.09	2.5	0.9	2.3	1.52	1.1
Fam 2	**UC11**	1.29	4.3	0.9	2.7	1.23	0.83
	UC12	1.29	4.3	4.74	1.9	1.51	4.74

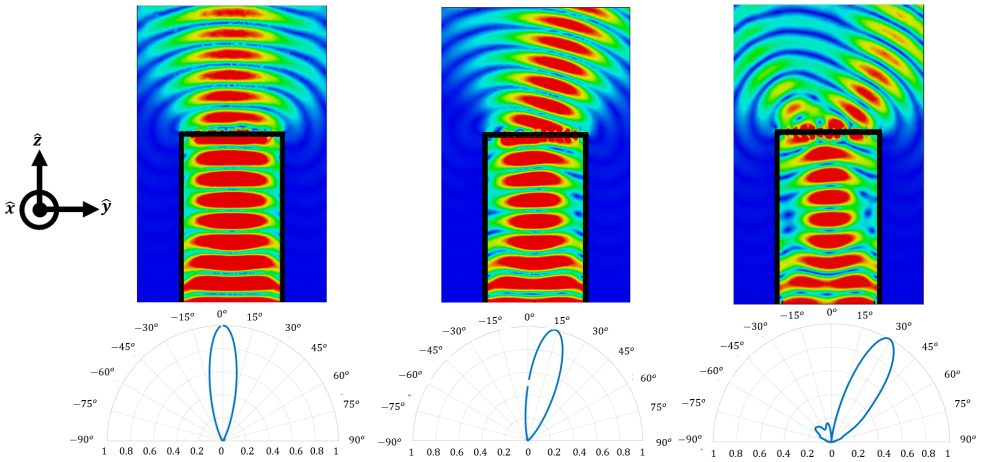

Figure 4.26 Simulations of the beam tilting for the metasurface supercells designed using the phase gradient method. Near field and absolute normalized radiation patterns at (a) the broadside, (b) 15^o, and (c) 30^o.

target one specific type of metasurface, the UC proposed in this Chapter can be used for both anisotropic and bianisotropic metasurface design. Notably, none of the previous studies have investigated bianisotropic metasurfaces incorporating electronically tunable components, which was demonstrated in this research. Related topics are discussed in [53, 89], which explore UCs for anomalous reflection and refraction. Among these, only [89] mentions

reconfigurability, although the design uses non-tunable lumped capacitors and resistors. The metasurface in [53] is passive and one of the few to consider inter-layer coupling in the design procedure. However, the proposed methodology in [53] relies on iterative adjustments to compensate for inter-layer coupling effects by altering the UC geometry. The analysis shown in this Chapter demonstrates that such compensation is not always feasible and emphasizes the need for an in-depth analysis to identify the reactance tunability limitations imposed by inter-layer coupling effects.

Other works listed in the table are non-bianisotropic metasurface UCs. For instance, the active UC in [80] features three layers separated by $\lambda_0/6$, reducing inter-layer coupling effects but resulting in a thickness of $0.45\lambda_0$. In contrast, the profile of the UC proposed in this study equals $0.11\lambda_0$. Decreasing the profile facilitates the integration of the design in certain applications. Additionally, the UC in [80] offers a broader reactance range due to the low capacitance of its selected varactors. However, the type of packaging of this varactor (Flip Chip Die) poses technical challenges for soldering. As such, this work proposes an alternative methodology to increase the reactance tunability range with a different varactor packaging (SC-79) through the use of dual-resonant geometries. Although the resulting tunability range is still less than that offered by Flip Chip Die varactors, the UC remains efficient for the design of reconfigurable bianisotropic and anisotropic metasurfaces.

Finally, the studies in [50,63] present single-resonant geometries using varactors similar to the one presented in this Chapter. Although their obtained reactance values are not reported, their scattering parameters exhibit limitations in magnitude and phase coverage, suggesting a behavior comparable to the one illustrated by the regular dogbone. Moreover, these UCs do not meet the requirements for bianisotropy. This reinforces the alternative of the dual-resonant geometries as proposed in this Chapter.

4.7 Conclusions

This study introduces a reconfigurable three-layer UC designed for anisotropic and bianisotropic Huygens Metasurfaces. Through a detailed methodology, it was demonstrated that the proposed dual-resonant geometries increase the tunability of reactances in 274% compared to the single-resonant counterparts. Waveguide measurements validate the design approach.

Moreover, an in-depth analysis of inter-layer coupling effects was presented, revealing that single-layer models are inadequate for predicting the middle layer's reactance after the layers are integrated in the multi-layer UC, as inter-layer coupling effects are stronger on this layer. Consequently, in some cases the middle layer loses its tunability, as was confirmed

through additional waveguide measurements. To address the limitations imposed by the inter-layer coupling effects, we proposed a hybrid design approach with two families of UCs: one offering independent layer tunability with limited transmission efficiency, and another providing limited middle-layer tunability but higher transmission efficiency. Simulations confirm the effectiveness of the proposed hybrid design approach, demonstrating a wide-refraction angle of 58.25^o with an efficiency of 86% using a bianisotropic supercell. Finally, a fully reconfigurable anisotropic metasurface supercell was presented, achieving beam tilting angles of 0^o, 15^o, and 30^o. These findings validate the potential of the proposed continuously tunable UC for advanced bianisotropic and phase-gradient beam tilting applications, paving the way for future research and development in this area.

Table 4.4 Comparison of the proposed Unit Cell with other works from the literature

Ref.	**UC geometry**	**Metasurface Application**	**Coupling analysis**	**Passive/ Active**	**Reactance Range (Ω)**	**Diode Characteristics**	**Tests**
[89]	Dual resonant: Square ring + Dogbone	Anomalous reflection	N/A	Passive with three lumped elements	Not reported	N/A	- UC/Supercell simulations. - Surface measurements.
[53]	Single resonant: Regular dogbone	Anomalous refraction	Yes	Passive	N/A	N/A	- Supercell simulations. - Surface measurements.
[80]	Dual resonant: Square ring + Split ring resonator	Leaky-waveguide with non-bianisotropic metasurface	No	Active	920*	MAVR-000120-1411** C_{var} = 0.07 pF to 0.9 pF L_p and R_p not specified	- UC simulations. - Surface measurements.
[63]	Single resonant: Square patch and rectangular slot	Transmission phase and magnitude control	No	Active	Not Specified	MA46H201-1088 C_{var} = 0.9 pF to 1.1 pF L_p and R_p not specified NXP-BB181 C_{var} = 0.7 pF to 14 pF R_p = 3 Ω L_p not reported	- UC simulations. - Waveguide measurements.
[50]	Single resonant: Square patch + rectangular slot	Transmission phase control	No	Active	Not reported	MGV100-20 C_{var} = 0.15 pF to 2 pF R_p = 2 Ω L_p 0.4 nH	- UC simulations. - Waveguide measurements.
This Work	Double resonant: Meander Dogbone, T Dogbone and T-ring Dogbone	Wide-refraction (bianisotropy), and beam tilting (phase gradient)	Yes	Active	∼250 for the meander dogbone Variable for the T dogbone ∼200 for the T-ring dogbone	SMV1275-079LF C_{var} = 0.83 pF to 4.74 pF L_p = 0.7 nH R_p = 0.8 Ω	- UC/supercell simulations. - Waveguide measurements.

* Values reported using a single-layer analysis (neglecting the inter-layer coupling effects).
** Package possessing soldering pads underneath the case.

CHAPTER 5 RECONFIGURABLE HUYGENS METASURFACE

5.1 Introduction

Periodic surfaces for transmission beam control are currently a hot topic in the antenna community, attracting significant attention for their potential to enhance communication links in next-generation telecommunications. Among the key applications, beam scanning has been extensively explored using metasurfaces and transmitarrays. Most designs utilize p-i-n and/or varactor diodes to achieve this purpose. However, these designs often encounter challenges related to the losses introduced by the diodes, the biasing required to polarize them, and the number of layers. Theoretically, a minimum of three layers is necessary to cover a phase of 360° for applying phase gradient in applications of transmitarray [58]. Various works in this regard are found in the literature. For example, a three-layer reconfigurable transmitarray is presented in [69], demonstrating beam scanning capabilities of ±25°. Despite its capabilities, this design has several limitations: the diodes introduce substantial losses, limiting phase coverage to 245° with transmission levels between -2.7 dB and -5.7 dB. Additionally, biasing requires hundreds of resistor chokes, considerably increasing fabrication complexity. And finally, the middle layer requires different polarization to the other two layers, further complicating the design by increasing the number of required sources. One approach to reduce the number of sources is to make all layers identical. This approach requires more than three layers, as studied in [49, 90, 91]. These works enhanced beam scanning capability and eliminated biasing chokes, but at the expense of increasing the surface thickness to $0.49\lambda_0$ and $0.8\lambda_0$. Additionally, high losses from the varactor diodes persisted in these designs.

An alternative method to reduce surface thickness with more than three layers is to use hybrid circuits for phase control, as explored in [91]. However, this approach increases the number of varactors per unit cell (UC), requiring four p-i-n diodes, two varactor diodes, and various capacitors, inductors, and resistors for biasing chokes. All previously discussed designs employ UCs with periodicity close to $0.5\lambda_0$. Conversely, Huygens metasurfaces present an alternative approach, as demonstrated in [71], where a dual-layer UC with p-i-n diodes was used as a 1-bit lens. However, this approach is limited by discrete reconfigurability, in contrast to the continuous reconfigurability that Huygens metasurface methodologies require.

This chapter aims to explore the potential application of the UC presented in Chapter 4 for a metasurface with beam scanning capability. Unlike previous designs, this approach achieves a low profile with minimal losses and requires no biasing chokes. Furthermore, the

UC's offers impedance tunability in a wide range, allowing for the exploration of additional Huygens metasurface methodologies.

The study in this chapter focuses on a metasurface attached to a linearly-polarized horn antenna. Simulations will demonstrate the scanning capability in one plane, showcasing comparable beam scanning performance to previous work, and reduced fabrication complexity. Additionally, the metasurface is embedded within a radome-like structure, which is crucial for various applications and represents a rarely explored case in the literature.

The rest of the chapter is structured as follows. Section 5.2 discusses how the feed lines for biasing are incorporated into the UC and studies their impact on the performance of the UC. Based on this analysis, the optimal design is selected for evaluating the complete metasurface. Section 5.3 presents the far-field performance of the metasurface, followed by a comparison with previous works in Section 5.4. Finally, Section 5.5 concludes with a summary of the results.

5.2 Effect of the feedlines in the UC

The reconfigurability of the metasurface depends on the accurate control of its elements. The design requires an array of $m \times n$ feedlines, multiplied by the number of layers in cases where each UC is controlled independently. This strategy can lead to hundreds of outputs and introduce uncertainties. An alternative approach is the control of rows and columns, as explored in [91]. This method connects all cathodes and anodes in rows and columns, reducing the number of elements to be polarized to $(m+n)$ times the number of layers. Fig. 5.1 illustrates this configuration which can be set to test the two main planes of the radiation ($\phi = 0°$ and $90°$) by connecting all the rows or columns to the bias ground, and controlling the other voltages.

The analysis in Section 4.3 demonstrated the inter-layer coupling effect in the two families of UCs. However, the inclusion of feedlines modifies the performance. The configuration of the feedlines in the UCs are depicted in Figs. 5.2a and 5.2b. All the other characteristics (geometries, thicknesses, materials, and so on) are preserved. Nonetheless, some practical modifications have been introduced. Instead of using two RO5880LZ substrates with a thickness of 5.08 mm each, the new configuration maintains the same total thickness but utilizes substrates with different thickness. Notably, the substrates with the geometries measure 1.27 mm. This thickness meets the maximum value that allows to do plated vias in the Poly-Grames facilities.

Figs. 5.2c, 5.2d, and 5.2e depict each layer with six feedlines, while Fig. 5.2f presents a

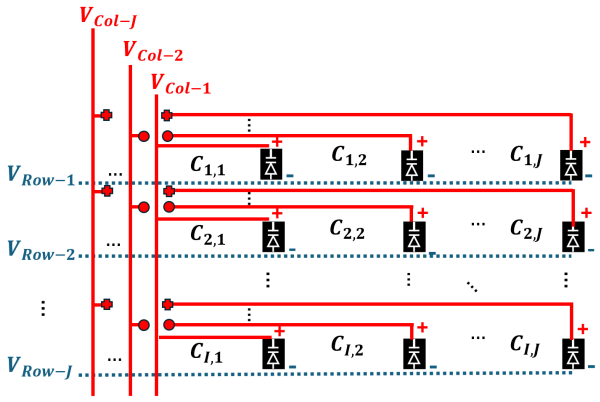

Figure 5.1 Configuration of the feedlines in the metasurface.

supercell composed of 6 UCs. The supercell illustrates how each column of UCs has different number of feedlines. The feedlines are spaced 0.2 mm apart with a width of 0.2 mm. The following subsections examine the impact of the feedlines on the performance of the UC families.

5.2.1 Meander Dogbones

Figs. 5.3a – 5.3c show the reactance of the meander dogbone structure with 6, 3, and 1 feedlines, compared to the single-layer calculation without feedlines as described in Chapter 4. The primary effect of inter-layer coupling is a shift in the reactance range, similar to the case without feedlines (see Fig. 4.10b). Table 5.1 summarizes the maximum and minimum reactance values for all cases. This analysis reveals that the reactance range with the feedlines equals approximately 265 Ω, which closely resembles the result of the single-layer configuration. However, the reactance range shifts towards more positive values. Although this shift should be considered for accurate metasurface tuning, it does not significantly impact the design, as it still meets the requirements for the top and bottom layers to synthesize anisotropic and bianisotropic metasurfaces.

Table 5.1 Meander reactance after inter-layer coupling

	Number of feedlines						
	No Feedlines	**1**	**2**	**3**	**4**	**5**	**6**
Max. Reactance (Ω)	-2.7	36	47	48	50	53	56
Min. Reactance (Ω)	-222	-235	-224	-219	-220	-213	-208

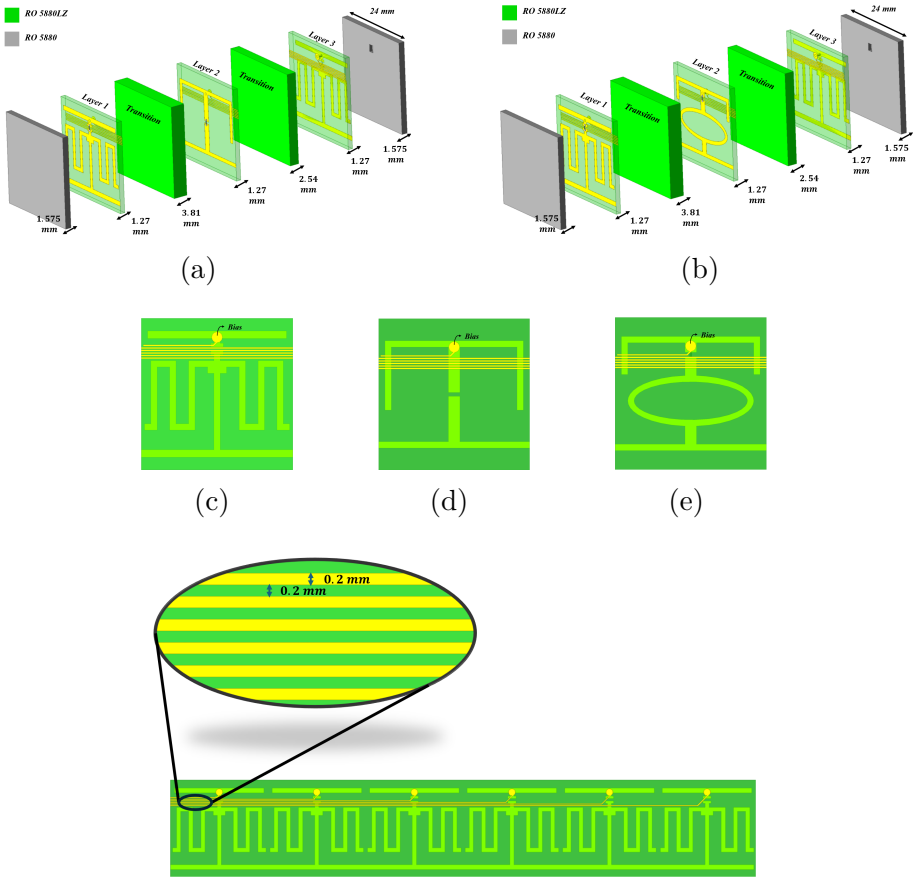

Figure 5.2 UCs with feed lines (a) family 1, (b) family 2, (c) meander dogbone, (d) T dogbone, (e) T_{ring} dogbone, and (f) supercell showing the meander dogbone and the feedlines zoomed.

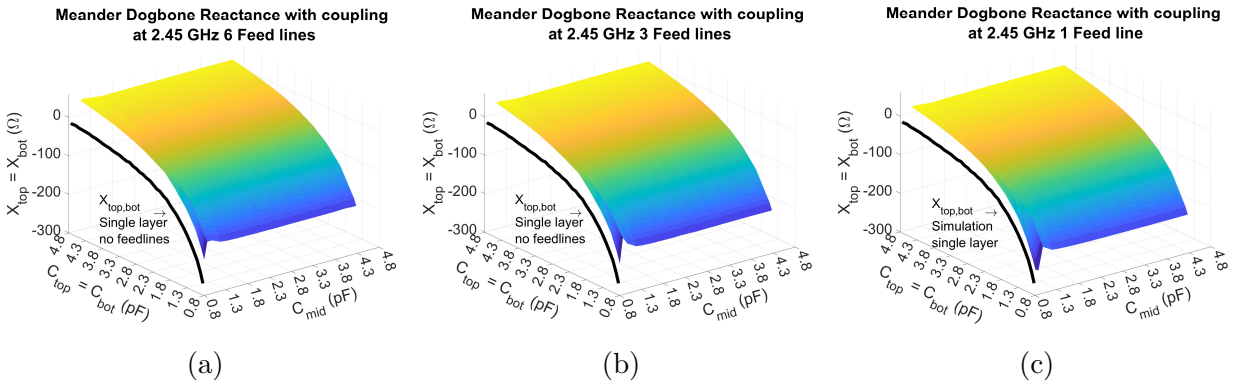

Figure 5.3 Reactance of the meander dogbone considering the coupling and (a) six feedlines, (b) three feedlines, and (c) one feedline.

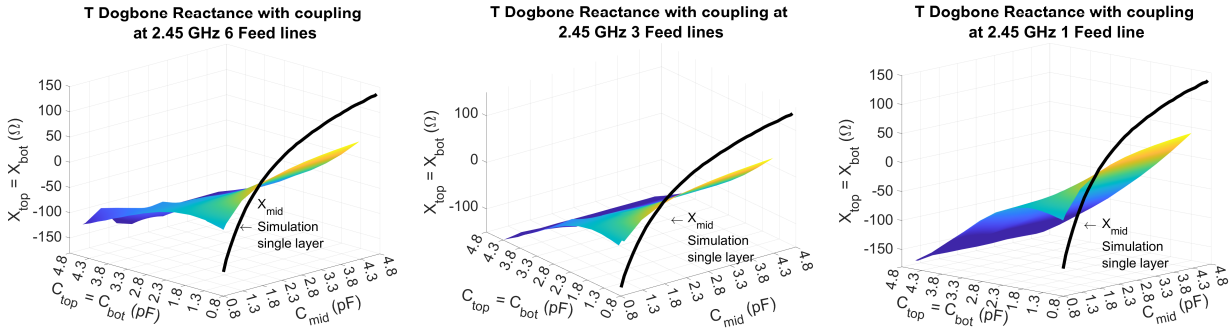

(a) (b) (c)

Figure 5.4 Reactance of the T dogbone considering the coupling and (a) six feedlines, (b) three feedlines, and (c) one feedline.

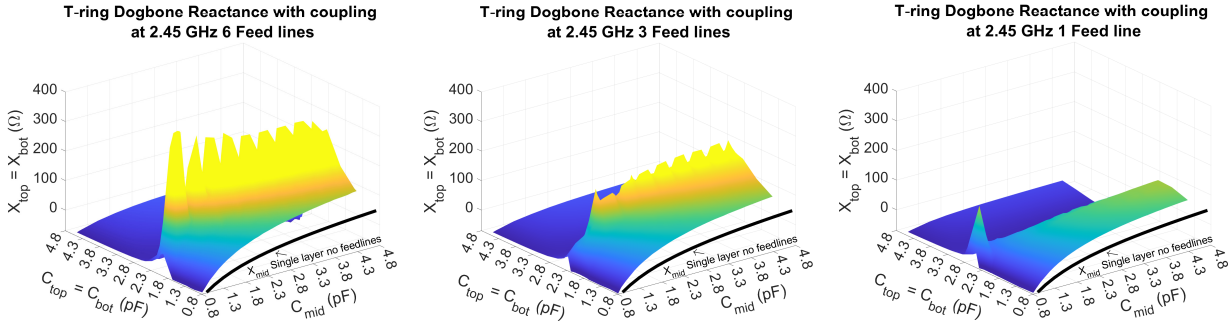

(a) (b) (c)

Figure 5.5 Reactance of the T dogbone considering the coupling and (a) six feedlines, (b) three feedlines, and (c) one feedline.

5.2.2 T and - T_{ring} Dogbones

Figs. 5.4a – 5.4c display the reactance of the T-dogbone with 6, 3, and 1 feedlines. The reactance maps exhibit behaviors similar to that shown in Fig. 4.10c. The reactance of the T dogbone is affected by the top and bottom layers, limiting tunability across most of the range. However, in a small region, the middle varactor diode adjusts the reactance between -50 Ω and 52 Ω. Similarly, Figs. 5.5a – 5.5c depict the reactance of the T_{ring} dogbone with 6, 3, and 1 feedlines. For this geometry, the feedlines introduce multiple resonances and cause a region of non-tunability for the top/bottom varactor diodes beyond 2.5 pF. The result of this deterioration is an increase in the losses of the T_{ring} dogbone, leading to two main consequences:

- The transmission phase range of the UC of family 2 (Fig. 5.6b) is reduced to 210° in

contrast to the 250° for the case without feedlines. This decrease in phase, constraints the utilization of this family for an anisotropic metasurface synthesis.

- Various required reactances for bianisotropic metasurface synthesis, fall within the resonance and non-tunable zones. Thus, the impedance matching of the UC in family 2 with feedlines will not be as optimal as in cases without feedlines. This will be demonstrated in the next subsection.

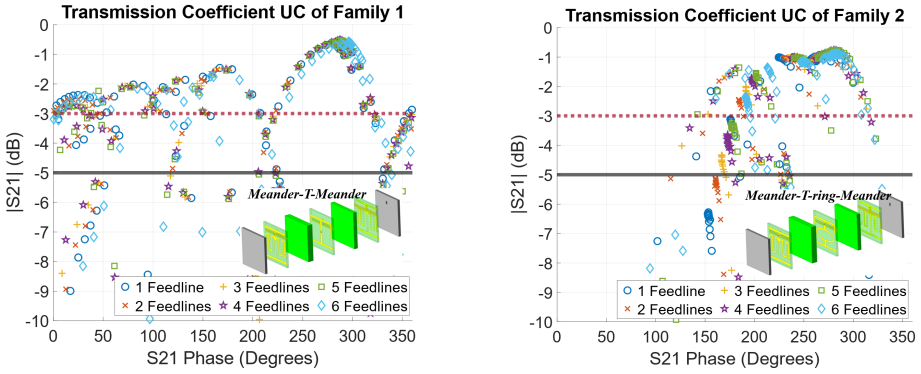

(a) (b)

Figure 5.6 Transmission coefficient for each case of feed lines for the (a) family 1, and (b) family 2.

5.2.3 Degradation of the bianisotropy

The proposed supercell with feedlines is composed of four UCs from family 1 and two from family 2, as shown in Fig. 5.7b. The feedlines include chokes represented by gaps in the supercell. This arrangement leads to the generalized parameters (Gpar) depicted in Fig. 5.8a. The reactances and capacitances used for each of the UCs are presented in Tables 5.2 and 5.3. The family of each UC corresponds to the configuration that provides the closest reactances to the required values. UC3 (which belongs to family 2) is the one with largest difference to the requirements as shown in Table 5.3. This error strongly impacts the efficiency of the metasurface. This is evident in Fig. 5.8b, which shows that the mode to excite (T_{-1}) equals -6.25 dB, resulting in a refraction efficiency of 65%. This efficiency is comparable to a configuration of an anisotropic metasurface realized using only the UCs from family 1. This effect, in addition of the superior performance in transmission of family 1, lead to a preference of this family over the other for the complete metasurface, as will be shown in the next section.

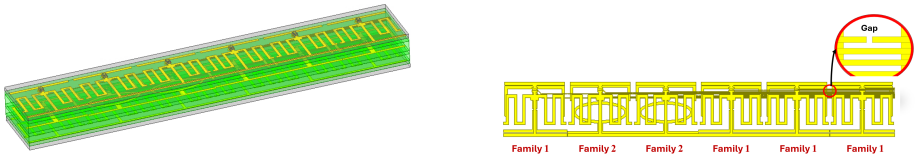

(a) (b)

Figure 5.7 Supercell with horizontal feedlines (a) complete structure with transparent substrates, and (b) geometries of all the layers.

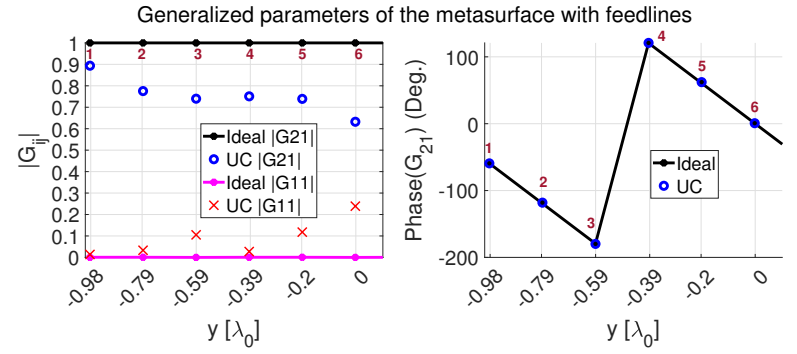

(a)

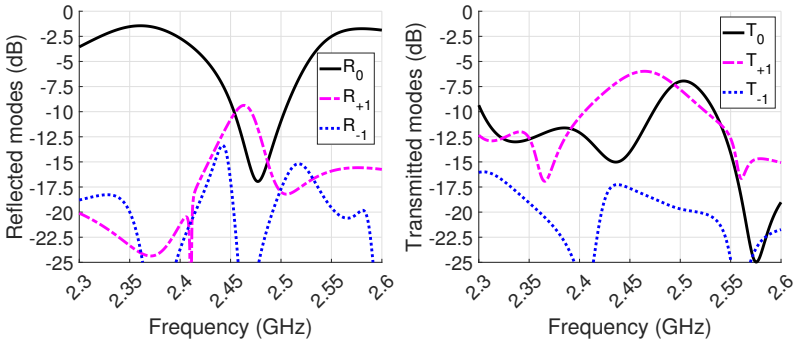

(b)

Figure 5.8 Performance of the supercell with feedlines (a) generalized parameters, and (b) S-parameters from the full-wave simulation.

Table 5.2 Capacitances for the bianisotropic metasurface supercell with feedlines

	Family 1	**Family 2**		**Family 3**		
	UC1	**UC2**	**UC3**	**UC4**	**UC5**	**UC6**
C_{top} **(pF)**	0.83	1.11	0.95	1.2	1.47	2.28
C_{mid} **(pF)**	3.3	1.35	0.83	1.3	1.53	1.55
C_{bot} **(pF)**	0.95	1.11	1.35	1.4	1.4	2.07

Table 5.3 Reactance of the proposed supercell with horizontal feedlines

	UC 1		UC 2		UC 3		UC 4		UC 5		UC 6	
	Family 1		Family 2		Family 2		Family 1		Family 1		Family 1	
	1 Feedline		2 Feedlines		3 Feedlines		4 Feedlines		5 Feedlines		6 Feedlines	
	Requ.	Achiev.	Requ.	Achiev.	Requ.	Achiev.	Requ.	Achiev.	Requ.	Achiev.	Requ.	Achiev.
X_{top} (Ω)	-203.04	-199.36	-118.38	-121.11	-67.95	***-87.62***	-101.58	-95.71	-79.03	-75.77	-22.72	-21.11
X_{mid} (Ω)	40.54	42.56	31.08	33.42	-83.69	***-65.24***	-15.74	-17.08	-14.09	-15.34	-37.27	-38.74
X_{bot} (Ω)	-174.11	-180.97	-128.63	-130.41	-190.73	***-128.48***	-93.80	-95.24	-83.48	-81.92	-29.02	-24.56

5.3 Reconfigurable anisotropic metasurface

The simulation setup consists of the metasurface attached to a horn antenna (ETS 3160-03) with an aperture measuring 33.96 x 25.97 cm^2, as shown in Fig. 5.9a. The distance between the metasurface and the horn aperture is around 5 cm. The size of the metasurface is 33.6 x 33.6 cm^2 ($2.7\lambda_0$ x $2.7\lambda_0$ at 2.45 GHz), and it has twelve rows and columns of UCs. The surface also includes additional feedlines to connect the metasurface to the voltage source (Fig. 5.9b). Additionally, to mitigate the effect of the small area of the metasurface, the simulation setup includes absorbers represented as perfectly matched layers surrounding the metasurface, as shown in Fig. 5.9c.

Three cases are evaluated to test the reconfigurability of the metasurface: broadside, $\theta = 20°$, and $\theta = 30°$, all in the plane $\phi = 90°$. The capacitances of the UCs are assigned according to the phases calculated using (4.9), the reactances of the UCs, and their respective phases from Fig. 5.6a. Table 5.4 shows the capacitances of each UC. The far fields obtained from the simulations in CST are presented in Fig. 5.10, and the performance is summarized in Table 5.5.

The results show that the metasurface tilts the beam, but it has a pointing error of 1.5° in the broadside case and 5.25° for the other two cases. The errors are mainly due to the small aperture size of the metasurface. Moreover, the worst sidelobe levels related to the maximum equal -1.4 dB in the broadside case, -5.2 dB for $\theta = 20°$, and -1.78 dB for $\theta = 30°$. These sidelobes are a consequence of the small metasurface's aperture size which is of $2.7\lambda_0$ x $2.7\lambda_0$ (counting the 12x12 UCs). This aperture size is comparable to the aperture size of the horn antenna ($2.83\lambda_0$ x $2.18\lambda_0$). The comparable aperture size leads to a large illumination in the edges of the metasurface causing edge difraction. Moreover, there is an interaction of the incident wave with the feed lines. In conclusion, the high sidelobe level is an intrinsic limitation of the metasurface's aperture size. However, the results demonstrate the capability of the metasurface to tilt the beam in various directions.

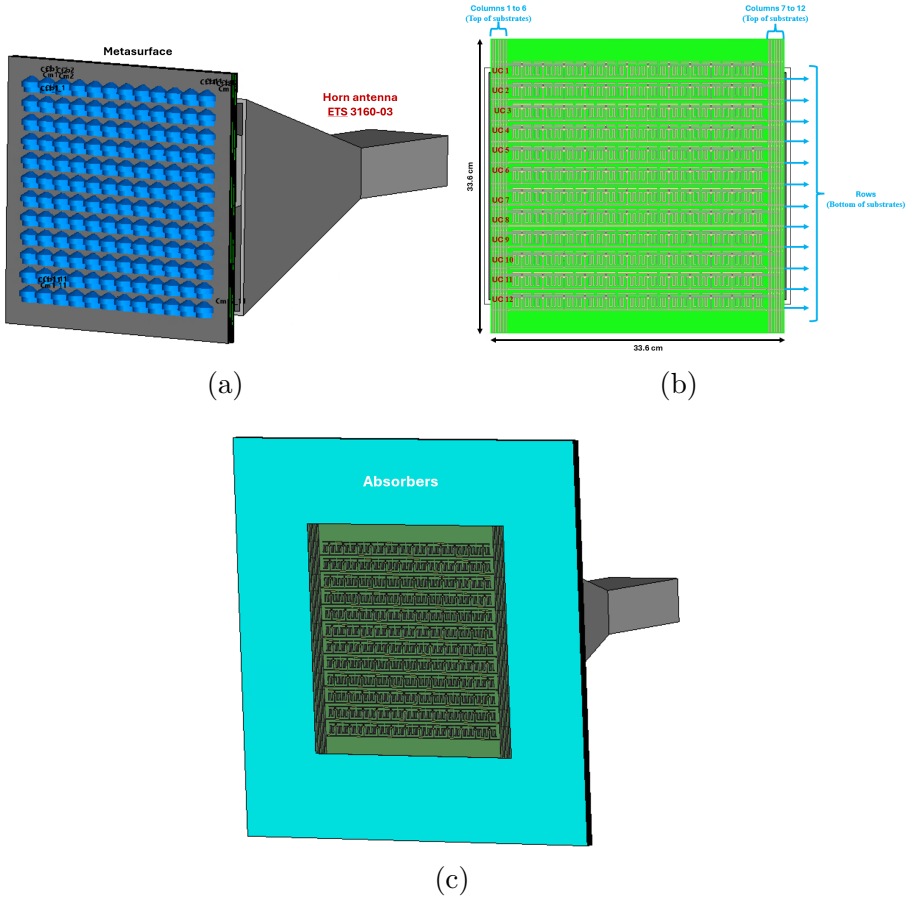

(a) (b)

(c)

Figure 5.9 Horn and metasurface setup for the fullwave simulations (a) isometric view, (b) Front view of the metasurface, and (c) setup with absorbers.

Table 5.4 Capacitances for the anisotropic metasurface with feedlines

		UC1	UC2	UC3	UC4	UC5	UC6	UC7	UC8	UC9	UC10	UC11	UC12
Broadside	$C_{top,bot}$ **(pF)**	0.89	0.9	0.9	0.9	0.9	0.97	0.97	0.9	0.9	0.9	0.9	0.89
	C_{mid} **(pF)**	4.74	4.3	4.3	4.3	4.74	4.74	4.74	4.74	4.3	4.3	4.3	4.74
$\theta = \mathbf{20}^o$	$C_{top,bot}$ **(pF)**	1.61	1.41	1.41	1.29	1.28	1.34	1.25	1.09	1.19	1.09	0.96	0.83
$phi = \mathbf{0}^o$	C_{mid} **(pF)**	1.6	1.6	1.4	1.4	1.2	0.83	0.83	0.83	4.74	4.74	4.74	3.3
$\theta = \mathbf{30}^o$	$C_{top,bot}$ **(pF)**	1.9	1.51	1.45	1.34	1.29	1.23	1.05	1.08	0.86	0.83	1.93	1.61
$phi = \mathbf{0}^o$	C_{mid} **(pF)**	1.6	1.6	1.4	1.3	0.9	0.83	0.83	4.74	4.74	2.1	1.6	1.6

5.4 Comparison with previous works

Table 5.6 compares various characteristics of the proposed metasurface with other designs. This table shows that:

- The proposed anisotropic metasurface offers advantages in terms of fabrication and design. It uses fewer layers than most designs, has a lower profile, requires fewer diodes

Table 5.5 Simulation of the beam-scanning reconfigurable metasurface at 2.45 GHz in the plane $\phi = 90^o$

Horn antenna gain		17.5 dB		
Scan Angle (Deg.)	**Target**	0	20	30
	Simulation	1.5	14.75	35.25
Gain with metasurface (dB)		11	10.5	12
SLL (dB)		-1.4	-5.2	-1.7
Grating lobes (Deg.)	**Simulation**	35 -35	56 -46	0
	Prediction	26.8 -23.5	50.1 -30.6	3.8

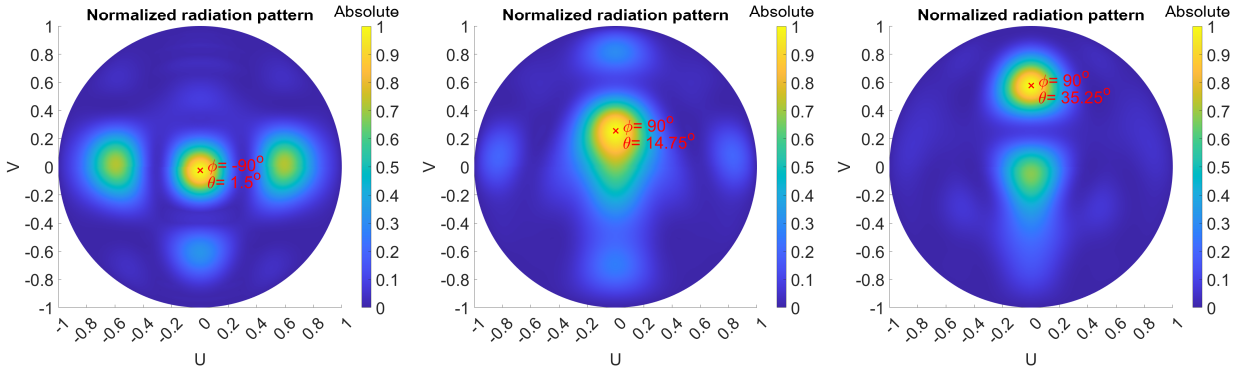

(a) (b) (c)

Figure 5.10 Farfield radiation pointing to (a) ϕ = -90^o, $\theta = 1.5^o$, (b) $\phi = 0^o$, $\theta = 14.75^o$, (c) $\phi = 0^o$, $\theta = 35.25^o$.

per UC, and does not require resistors or inductor chokes.

- The metasurface has lower losses than the works presented in [69, 90, 92]. While some of these studies report surfaces with a phase coverage greater than 360°, they account for losses of more than -4 dB, which is the baseline loss of the metasurface proposed in this work.

- The metasurface presented in [71] is also a Huygens metasurface. However, it has limited applications, as its double layer and type of p-i-n diode do not allow for a wide range of impedance shifts, unlike the metasurface proposed in this work.

- The proposed metasurface also includes top/bottom substrates that act as radomes. This feature is rarely explored in the literature but is useful for applications requiring protection from environmental damage.

- Although the proposed metasurface has a smaller aperture than the other works, its

scanning capability is comparable to most of them. However, its smaller aperture is the main constraint leading to point error and high SLL. In this sense, the other works offer better capabilities.

Overall, while the metasurface demonstrates comparable performance in terms of beam scanning with similar designs, its advantages lie in lower losses and simpler fabrication, requiring fewer metallic layers and fewer varactor diodes than other designs.

5.5 Conclusion

This chapter presented an analysis based on simulations of the reconfigurable implementations of the dual-resonant UCs proposed in Chapter 4. A detailed analysis of the feed lines for biasing the varactors is presented to highlight the limitations in utilizing the UC of family 2 to synthetize an electronically tunable bianisotropic, or anisotropic metasurface. The primary consequence of this limitation is a reduction in refraction efficiency for the bianisotropic metasurface, with an observed efficiency of approximately 65%, comparable to that of an anisotropic metasurface composed of only the UC of family 1. Consequently, the evaluated Huygens metasurface with the horn antenna was designed to be anisotropic, utilizing only UCs of family 1.

The proposed metasurface demonstrates a lower profile compared to previous designs in the literature, achieving a thickness of $0.11\lambda_0$ with reduced losses, providing a phase coverage of 360° with transmission higher than -4 dB. The proposed metasurface was simulated for beam scanning capability up to 30° in one plane, with results confirming successful beam steering while simplifying fabrication complexity.

These findings establish that the proposed metasurface as an effective solution for beam tilting, minimizing losses, and offering structural simplicity compared to existing designs. This work lays the foundation for further research into enhanced metasurface designs with potential applications in advanced communication systems.

Future work includes fabricating and test a metasurface with 12x12 UCs and measuring its scanning capability. Moreover, a different distribution of the feedlines, and larger aperture would make more evident the potential advantages of this metasurface.

Table 5.6 Comparison with previous designs

Reference	**Methodology of design**	**Frequency (GHz)**	**No. of metallic layers**	**Thickness (λ_0)**	**Diodes per UC**	**Chokes**	**Transmission coverage**	**Aperture size ($\lambda_0 x \lambda_0$)**	**Beam Scanning (Deg.)**	**SLL (dB)**	**Point Error (Deg.)**	**Radome**
[71]	Huygens Metasurface	12.8	2 (No air spaces)	0.14	2 p-i-n	Yes	N/A	5.2 x 5.2	-50 to 50	$<$ -7	$<$ 1	No
[91]	Phase gradient Transmitarray	19	5 (Air spaced-layers)	0.8	5 varactors	No	$\geq -3.5dB \rightarrow 360^o$	5 x 5	-40 to 40	$\sim$ -11	$<$ 1	No
[90]	FSS-Inspired Transmitarray	5.3	5 (Air spaced-layers)	0.49	10 varactors	No	$\geq -8dB \rightarrow 400^o$	3.18 x 3.18	2D tilt -30 to 30	-5 to -13	0 to 3	No
[92]	Phase shifting Transmitarray	5.4	4 (No air spaces)	0.13	2 p-i-n + 4 varactors	Yes	$\geq -5.5dB \rightarrow 400^o$	3.87 x 3.87	-60 to 60	$\sim$ -10	$<$ 1	No
[69]	Phase gradient Transmitarray	5.7	3 (No air spaces)	0.11	5 varactor	Yes	$\geq -5.7dB \rightarrow 245^o$ $\geq -10dB \rightarrow 330^o$	3.42 x 3.42	-25 to 25	$<$ -6	$<$ 1	No
This work	Anisotropic Huygens Metasurface	2.45	3 (No air spaces)	0.11	3 varactors	No	$\geq -3dB \rightarrow 330^o$ $\geq -4dB \rightarrow 360^o$	2.7 x 2.7	-35 to 35	-1.4 to -5.2	1 to 5	Yes

CHAPTER 6 CONCLUSION

6.1 Conclusions

This thesis introduced innovative solutions in designing and analyzing advanced reconfigurable Huygens' metasurfaces and millimeter-wave reflectarrays for satellite applications. Chapter 2 presented a seven-faceted RA with an equivalent aperture size of $62.3\lambda_0$ at 50 GHz. The design is based on a single-band UC, and its 1- and 3-dB gain bandwidths are 13.4% and 25.6%, covering the whole V-band and a portion of the Q-band. Similarly, the axial ratio remains below 0.9 dB in the two bands. Moreover, the radiation pattern is pencil-beam along the two bands. This outstanding performance overcomes classical planar RAs and three-faceted configurations with similar aperture sizes. The performance improvement is due to the exploration of the multi-faceted perspective. The thesis explores for the first time a complete methodology to design multi-faceted RAs and to evaluate them by extending the array approach method. This method estimates the gain and co-polarized radiation pattern of the antenna with an error margin of ± 1.5 dB and it takes a few minutes in contrast to the hours (or even weeks) required by full-wave simulations for large-aperture, multi-faceted reflectarrays.

Chapter 3 expanded the multi-faceted work by integrating a frequency selective surface that allows designing a dual-band UC for independent phase control across the Q- and V-bands. The phase coverage in each band exceeds 400° in the two bands, showing better performance than previous designs. Moreover, the UC is more compact as it does not require air spacers. The independent phase control leads to the optimization of the gain at 40 GHz and 50 GHz, achieving two peaks and keeping gain BWs between 5% and 7%, which are comparable to better than other designs. However, the proposed design has a larger aperture size.

These contributions establish foundations for next-generation satellite systems, addressing challenges such as wide and multi-band operation for large-aperture, circularly polarized, multi-faceted reflectarrays.

Chapters 4 and 5 explore the development of reconfigurable Huygens metasurfaces, highlighting the significant advancements in tunability and reduced-profile designs. An in-depth study of UC design was proposed to prove that dual-resonant geometries can increase the reactance tunability up to 250Ω over the $\leq 100\Omega$ offered by single-resonant designs. Additionally, the research presented a theoretical and practical characterization of inter-layer coupling and its influence on reactance control. The results show that the coupling effects decrease the

impedance tunability of some geometries. Therefore, a metasurface with wide-impedance tunability depends on selecting proper geometries that allow efficient control. The study proposed a solution using two families of UCs to synthesize anisotropic and bianisotropic metasurfaces. The proposed reconfigurable UC has a beam scanning capability of ± 30° on its anisotropic mode, while it can refract a beam to 59° with 86% of efficiency on its bianisotropic mode. The thesis also includes simulations of the UC in a metasurface of 12x12 UCs. The analysis shows how the biasing feedlines impact the UC's impedance and provides results of full-wave simulations of the beam scanning in one plane up to 30°.

The contribution to reconfigurable metasurfaces lies in the study of UCs, which have the potential to be applied to Huygens metasurfaces that can exploit anisotropic and bianisotropic capabilities. This leads to various applications that offer potential solutions to future generations of telecommunications.

6.2 Future work

All the contributions in this thesis offer the possibility to extend the research. In the topic of multi-faceted reflectarrays some of the recommendations for future research are:

- To explore more in-depth other parameters of the multi-faceted perspective. This thesis compared the petals' inclination for a seven-faceted reflectarray to a three-faceted and a planar case. However, there is a gap in studies of different faces and irregular shapes. Including these characteristics could improve even more the performance of this perspective.
- A fundamental step to consolidate the multi-faceted perspective is to explore methods offering better alignment to improve the quality of the measurements.
- The proposed dual-band UC has a gap to notably improve the axial ratio. The key parameter to achieve this enhancement is the frequency selective surface. It is fundamental to study a geometry offering less sensitivity to oblique incidences. This optimization would improve the RA gain in the two bands.

On the other side, the recommendations for the reconfigurable Huygens metasurfaces are:

- Including the biasing feedlines remains one of the major challenges in designing reconfigurable metasurfaces. In-depth research is required to include the feedlines while minimizing their impact on the impedance tunability achieved by the dual-resonant

geometries. One possibility to explore in future works is to consider the feedlines as part of the design from the beginning.

- To explore other geometries with low impact of the inter-layer coupling, such as the T-ring dogbone. Potential candidates are loops. Nonetheless, these geometries are single single-resonant. Therefore, it is essential to research how to include a second resonance to achieve wide-impedance tunability.

- The fabrication and measurement of the metasurface remains as future work. While the proposed UCs show advantages in terms of tunability and less insertion loss, the fabrication and measurement of the metasurface would be an interesting contribution to testing the beam scanning capabilities in the two main planes of the antenna.

6.3 Scientific contributions of the thesis

6.3.1 Journal papers

1. P. Camacho, K. Glatre, E. Baladi and M. S. Sharawi, "Wideband, Circularly Polarized, Large Multi-Faceted Reflectarray for Satellite Applications," in IEEE Transactions on Antennas and Propagation, doi: 10.1109/TAP.2024.3521210.

2. P. Camacho, E. Baladi, and M. S. Sharawi, "Design and Characterization of a Unit Cell with Wide-Reconfigurable Impedance for Anisotropic and Bianisotropic Huygens Metasurfaces" under preparation

3. P. Camacho, K. Glatre, E. Baladi, and M. S. Sharawi, "A Dual-Band, Large Multi-Faceted Reflectarray Using a Frequency Selective Surface-Based Unit Cell" under preparation

6.3.2 Conference papers

1. P. Camacho and M. S. Sharawi, "Active Unit Cell with Continuous Transmission Phase for a Radome-Periodic Structure in S-band," 2022 16th European Conference on Antennas and Propagation (EuCAP), Madrid, Spain, 2022, pp. 1-4, doi: 10.23919/EuCAP53622.2022.9769011

2. P. Camacho and M. S. Sharawi, "Analysis of the Interlayer Coupling Impact on the Impedance and Transmission of a 3-layer Unit Cell Embedded on a Radome," 2023 17th European Conference on Antennas and Propagation (EuCAP), Florence, Italy, 2023, pp. 1-4, doi: 10.23919/EuCAP57121.2023.10133601.

3. P. Camacho, K. Glatre, E. Baladi and M. S. Sharawi, "Large, Multi-Faceted Reflectarray with Quasi-Constant Directivity in the V-Band," 2024 18th European Conference on Antennas and Propagation (EuCAP), Glasgow, United Kingdom, 2024, pp. 1-5, doi: 10.23919/EuCAP60739.2024.10501532.

4. P. Camacho, K. Glatre, E. Baladi and M. S. Sharawi, "A Large, Seven-Faceted Reflectarray for Millimiter-Wave Applications," 2024 IEEE International Symposium on Antennas and Propagation and INC/USNC-URSI Radio Science Meeting (AP-S/INC-USNC-URSI), Firenze, Italy, 2024, pp. 2369-2370, doi: 10.1109/AP-S/INC-USNC-URSI52054.2024.10686245.

6.3.3 Patent

1. **A Dual-Dand Unit Cell with a Frequency Selective Surface Integrated:** K. Glatre and P. Camacho. Patent in process by MDA Space.

6.3.4 Acknowledgements

1. **TICRA-EurAAP Grant:** Grant to assist in the EuCAP 2024 conference to present the paper "Large, Multi-Faceted Reflectarray with Quasi-Constant Directivity in the V-Band".

2. **3rd place in the competition *My thesis in three minutes* in the Ecole Polytechnique de Montreal:** This is a competition of scientific divulgation to the general public.

6.3.5 Other contributions

1. **Publication in the IEEE Open Journal of the Communications Society:**

   E. Guven, P. Camacho, E. Baladi and G. Karabulut Kurt, "On the Role of Reflectarrays for Interplanetary Links," in IEEE Open Journal of the Communications Society, vol. 5, pp. 6227-6238, 2024, doi: 10.1109/

2. **2021 IEEE Indian Conference on Antennas and Propagation (InCAP):**

   - J. Wani, P. Camacho, R. S. Malfajani and M. S. Sharawi, "A multi-wide-band Planar 4-element MIMO Antenna System for WLAN Applications," 2021 IEEE Indian Conference on Antennas and Propagation (InCAP), Jaipur, Rajasthan, India, India, 2021, pp. 121-124, doi: 10.1109/InCAP52216.2021.9726290.

- J. Wani, P. Camacho, R. S. Malfajani and M. S. Sharawi, "Design and Fabrication of a multi-band 2Element MIMO Antenna for Sub-6 GHz Applications," 2021 IEEE Indian Conference on Antennas and Propagation (InCAP), Jaipur, Rajasthan, India, India, 2021, pp. 198-200, doi: 10.1109/InCAP52216.2021.9726512.

REFERENCES

[1] R. E. Hodges, J. C. Chen, M. R. Radway, L. R. Amaro, B. Khayatian, and J. Munger, "An extremely large ka-band reflectarray antenna for interferometric synthetic aperture radar: Enabling next-generation satellite remote sensing," *IEEE Antennas and Propagation Magazine*, vol. 62, no. 6, pp. 23–33, 2020.

[2] B. Imaz-Lueje, M. R. Pino, and M. Arrebola, "Deployable multi-faceted reflectarray antenna in offset configuration with band enhancement," *IEEE Transactions on Antennas and Propagation*, vol. 70, no. 12, pp. 11 686–11 696, 2022.

[3] D. R. Smith, W. J. Padilla, D. C. Vier, S. C. Nemat-Nasser, and S. Schultz, "Composite medium with simultaneously negative permeability and permittivity," *Phys. Rev. Lett.*, vol. 84, pp. 4184–4187, May 2000. [Online]. Available: https://link.aps.org/doi/10.1103/PhysRevLett.84.4184

[4] B. A. Munk, *Frequency selective surfaces: theory and design*. John Wiley & Sons, 2005.

[5] P. Nayeri, F. Yang, and A. Z. Elsherbeni, *Reflectarray antennas: theory, designs, and applications*. John Wiley & Sons, 2018.

[6] J. Huang and J. A. Encinar, *Reflectarray antennas*. John Wiley & Sons, 2007.

[7] M. R. Chaharmir, J. Ethier, and J. Shaker, *Reflectarray Antennas: Analysis, Design, Fabrication, and Measurement*, 2013.

[8] P. I. Theoharis, R. Raad, F. Tubbal, M. U. A. Khan, and A. Jamalipour, "Wideband reflectarrays for 5g/6g: A survey," *IEEE Open Journal of Antennas and Propagation*, vol. 3, pp. 871–901, 2022.

[9] J. A. Joy, S. K. Palaniswamy, S. Kumar, M. Kanagasabai, S. Bashyam, and M. I. Hussein, "Modern reflectarray antennas: A review of the design, state-of-the-art, and research challenges," *IEEE Access*, vol. 12, pp. 46 717–46 740, 2024.

[10] M. H. Dahri, M. H. Jamaluddin, M. I. Abbasi, and M. R. Kamarudin, "A review of wideband reflectarray antennas for 5g communication systems," *IEEE Access*, vol. 5, pp. 17 803–17 815, 2017.

[11] S. V. Hum and J. Perruisseau-Carrier, "Reconfigurable reflectarrays and array lenses for dynamic antenna beam control: A review," *IEEE Transactions on Antennas and Propagation*, vol. 62, no. 1, pp. 183–198, 2014.

[12] E. Carrasco, J. A. Encinar, and M. Barba, "Bandwidth improvement in large reflectarrays by using true-time delay," *IEEE Transactions on Antennas and Propagation*, vol. 56, no. 8, pp. 2496–2503, 2008.

[13] X. Xia, Q. Wu, H. Wang, C. Yu, and W. Hong, "Wideband millimeter-wave microstrip reflectarray using dual-resonance unit cells," *IEEE Antennas and Wireless Propagation Letters*, vol. 16, 2017.

[14] Z.-W. Miao and Z.-C. Hao, "A wideband reflectarray antenna using substrate integrated coaxial true-time delay lines for qlink-pan applications," *IEEE Antennas and Wireless Propagation Letters*, vol. 16, pp. 2582–2585, 2017.

[15] W.-L. Guo, G.-M. Wang, K.-Y. Liu, Y.-Q. Zhuang, and Q.-C. Ge, "Design of single-layered ultrawideband high-efficiency circularly polarized reflectarray," *IEEE Antennas and Wireless Propagation Letters*, vol. 17, no. 8, pp. 1386–1390, 2018.

[16] Q. Gao, J. Wang, Y. Li, and Z. Li, "A multiresonant element for bandwidth enhancement of circularly polarized reflectarray antennas," *IEEE Antennas and Wireless Propagation Letters*, vol. 17, no. 5, pp. 727–730, 2018.

[17] E.-C. Choi and S. Nam, "W-band low phase sensitivity reflectarray antennas with wideband characteristics considering the effect of angle of incidence," *IEEE Access*, vol. 8, pp. 111 064–111 073, 2020.

[18] S. M. A. M. H. Abadi and N. Behdad, "True-time-delay uwb reflectarray with linear to circular polarization transformation," in *2016 IEEE International Symposium on Antennas and Propagation (APSURSI)*, 2016, pp. 1205–1206.

[19] S. M. A. Momeni Hasan Abadi, K. Ghaemi, and N. Behdad, "Ultra-wideband, true-time-delay reflectarray antennas using ground-plane-backed, miniaturized-element frequency selective surfaces," *IEEE Transactions on Antennas and Propagation*, vol. 63, no. 2, pp. 534–542, 2015.

[20] S. M. A. Momeni Hasan Abadi and N. Behdad, "Broadband true-time-delay circularly polarized reflectarray with linearly polarized feed," *IEEE Transactions on Antennas and Propagation*, vol. 64, no. 11, pp. 4891–4896, 2016.

[21] M. Zhou, S. B. Sørensen, Y. Brand, and G. Toso, "Doubly curved reflectarray for dual-band multiple spot beam communication satellites," *IEEE Transactions on Antennas and Propagation*, vol. 68, no. 3, pp. 2087–2096, 2020.

[22] E. Baladi, M. Y. Xu, N. Faria, J. Nicholls, and S. V. Hum, "Dual-band circularly polarized fully reconfigurable reflectarray antenna for satellite applications in the ku-band," *IEEE Transactions on Antennas and Propagation*, vol. 69, no. 12, pp. 8387–8396, 2021.

[23] P. Naseri, M. Riel, Y. Demers, and S. V. Hum, "A dual-band dual-circularly polarized reflectarray for k/ka-band space applications," *IEEE Transactions on Antennas and Propagation*, vol. 68, no. 6, pp. 4627–4637, 2020.

[24] R. S. Malfajani and Z. Atlasbaf, "Design and implementation of a dual-band single layer reflectarray in x and k bands," *IEEE Transactions on Antennas and Propagation*, vol. 62, no. 8, pp. 4425–4431, 2014.

[25] R. Shamsaee Malfajani and B. Abbasi Arand, "Dual-band orthogonally polarized single-layer reflectarray antenna," *IEEE Transactions on Antennas and Propagation*, vol. 65, no. 11, pp. 6145–6150, 2017.

[26] R. L. Farias, C. Peixeiro, and M. V. T. Heckler, "Single-layer dual-band dual-circularly polarized reflectarray for space communication," *IEEE Transactions on Antennas and Propagation*, vol. 70, no. 7, pp. 5989–5994, 2022.

[27] T. Su, X. Yi, and B. Wu, "X/ku dual-band single-layer reflectarray antenna," *IEEE Antennas and Wireless Propagation Letters*, vol. 18, no. 2, pp. 338–342, 2019.

[28] X. Li, X. Li, and L. Yang, "Single-layer dual-band wide band-ratio reflectarray with orthogonal linear polarization," *IEEE Access*, vol. 8, pp. 93 586–93 593, 2020.

[29] D. Martinez-de Rioja, R. Florencio, E. Martinez-de Rioja, M. Arrebola, J. A. Encinar, and R. R. Boix, "Dual-band reflectarray to generate two spaced beams in orthogonal circular polarization by variable rotation technique," *IEEE Transactions on Antennas and Propagation*, vol. 68, no. 6, pp. 4617–4626, 2020.

[30] X. Tong, Z. H. Jiang, Y. Li, F. Wu, R. Sauleau, and W. Hong, "Dual-wideband dual-circularly-polarized shared-aperture reflectarrays with a single functional substrate for k-/ka-band applications," *IEEE Transactions on Antennas and Propagation*, vol. 70, no. 7, pp. 5404–5417, 2022.

[31] H. Hasani, C. Peixeiro, A. K. Skrivervik, and J. Perruisseau-Carrier, "Single-layer quad-band printed reflectarray antenna with dual linear polarization," *IEEE Transactions on Antennas and Propagation*, vol. 63, no. 12, pp. 5522–5528, 2015.

[32] J. Zhu, Y. Yang, D. Mcgloin, S. Liao, and Q. Xue, "3-d printed all-dielectric dual-band broadband reflectarray with a large frequency ratio," *IEEE Transactions on Antennas and Propagation*, vol. 69, no. 10, pp. 7035–7040, 2021.

[33] P. Xu, L. Li, R. Li, and H. Liu, "Dual-circularly polarized spin-decoupled reflectarray with fss-back for independent operating at ku-/ka-bands," *IEEE Transactions on Antennas and Propagation*, vol. 69, no. 10, pp. 7041–7046, 2021.

[34] M. Abdollahvand, K. Forooraghi, J. A. Encinar, Z. Atlasbaf, and E. Martinez-de Rioja, "A 20/30 ghz reflectarray backed by fss for shared aperture ku/ka-band satellite communication antennas," *IEEE Antennas and Wireless Propagation Letters*, vol. 19, no. 4, pp. 566–570, 2020.

[35] R. Deng, S. Xu, F. Yang, and M. Li, "An fss-backed ku/ka quad-band reflectarray antenna for satellite communications," *IEEE Transactions on Antennas and Propagation*, vol. 66, no. 8, pp. 4353–4358, 2018.

[36] M. R. Chaharmir and J. Shaker, "Design of a multilayer x-/ka-band frequency-selective surface-backed reflectarray for satellite applications," *IEEE Transactions on Antennas and Propagation*, vol. 63, no. 4, pp. 1255–1262, 2015.

[37] R. Deng, F. Yang, S. Xu, and M. Li, "An fss-backed 20/30-ghz dual-band circularly polarized reflectarray with suppressed mutual coupling and enhanced performance," *IEEE Transactions on Antennas and Propagation*, vol. 65, no. 2, pp. 926–931, 2017.

[38] N. Chahat, E. Decrossas, D. Gonzalez-Ovejero, O. Yurduseven, M. J. Radway, R. E. Hodges, P. Estabrook, J. D. Baker, D. J. Bell, T. A. Cwik, and G. Chattopadhyay, "Advanced cubesat antennas for deep space and earth science missions: A review," *IEEE Antennas and Propagation Magazine*, vol. 61, no. 5, pp. 37–46, 2019.

[39] N. Chahat, *CubeSat antenna design*. John Wiley & Sons, 2021.

[40] A. J. Rubio, A.-S. Kaddour, C. Ynchausti, S. Magleby, L. L. Howell, and S. V. Georgakopoulos, "A foldable reflectarray on a hexagonal twist origami structure," *IEEE Open Journal of Antennas and Propagation*, vol. 2, pp. 1108–1119, 2021.

[41] D. Martinez-de Rioja, E. Martinez-de Rioja, Y. Rodriguez-Vaqueiro, J. A. Encinar, A. Pino, M. Arias, and G. Toso, "Transmit–receive parabolic reflectarray to generate two beams per feed for multispot satellite antennas in ka-band," *IEEE Transactions on Antennas and Propagation*, vol. 69, no. 5, pp. 2673–2685, 2021.

[42] B. Imaz-Lueje, M. Arrebola, and M. R. Pino, "Design of a 5-panel multi-faceted reflectarray in offset configuration," in *2022 Global Conference on Wireless and Optical Technologies (GCWOT)*, 2022, pp. 1–5.

[43] V. Patel, P. Mevada, D. Pujara, S. Chakrabarty, and M. Mahajan, "Analysis of multi-faceted reflectarray antenna for spatial bandwidth improvement," in *2020 IEEE International Symposium on Antennas and Propagation and North American Radio Science Meeting*, 2020, pp. 359–360.

[44] M. Zhou and S. B. Sørensen, "Design of multi-faceted dual-polarization dual-coverage contoured beam reflectarray," in *2014 IEEE Antennas and Propagation Society International Symposium (APSURSI)*, 2014, pp. 799–800.

[45] M. Zhou, S. B. Sørensen, P. Meincke, and E. Jørgensen, "Design and optimization of multi-faceted reflectarrays for satellite applications," in *The 8th European Conference on Antennas and Propagation (EuCAP 2014)*, 2014, pp. 1423–1427.

[46] B. A. Homssi, C. C. Chan, K. Wang, W. Rowe, B. Allen, B. Moores, L. Csurgai-Horváth, F. P. Fontán, S. Kandeepan, and A. Al-Hourani, "Deep learning forecasting and statistical modeling for q/v-band leo satellite channels," *IEEE Transactions on Machine Learning in Communications and Networking*, vol. 1, pp. 78–89, 2023.

[47] M. Aloisio, P. Angeletti, F. Coromina, and R. De Gaudenzi, "Exploitation of q/v-band for future broadband telecommunication satellites," in *IVEC 2012*, 2012, pp. 351–352.

[48] Q. Xi, C. Ma, H. Li, B. Zhang, C. Li, and L. Ran, "A reconfigurable planar fresnel lens for millimeter-wave 5g frontends," *IEEE Transactions on Microwave Theory and Techniques*, vol. 68, no. 11, pp. 4579–4588, 2020.

[49] J. R. Reis, R. F. S. Caldeirinha, A. Hammoudeh, and N. Copner, "Electronically reconfigurable fss-inspired transmitarray for 2-d beamsteering," *IEEE Transactions on Antennas and Propagation*, vol. 65, no. 9, pp. 4880–4885, 2017.

[50] J. Y. Lau and S. V. Hum, "Analysis and characterization of a multipole reconfigurable transmitarray element," *IEEE Transactions on Antennas and Propagation*, vol. 59, no. 1, pp. 70–79, 2011.

[51] M. Chen, E. Abdo-Sánchez, A. Epstein, and G. V. Eleftheriades, "Theory, design, and experimental verification of a reflectionless bianisotropic huygens' metasurface for wide-angle refraction," *Phys. Rev. B*, vol. 97, p. 125433, Mar 2018. [Online]. Available: https://link.aps.org/doi/10.1103/PhysRevB.97.125433

[52] G. Lavigne, K. Achouri, V. S. Asadchy, S. A. Tretyakov, and C. Caloz, "Susceptibility derivation and experimental demonstration of refracting metasurfaces without spurious diffraction," *IEEE Transactions on Antennas and Propagation*, vol. 66, no. 3, pp. 1321–1330, 2018.

[53] A. E. Olk, P. E. M. Macchi, and D. A. Powell, "High-efficiency refracting millimeter-wave metasurfaces," *IEEE Transactions on Antennas and Propagation*, vol. 68, no. 7, pp. 5453–5462, 2020.

[54] F. Giusti, E. Martini, S. Maci, and M. Albani, "Comparison between different approaches for the design of anomalous refractors," *IEEE Transactions on Antennas and Propagation*, vol. 72, no. 4, pp. 3495–3506, 2024.

[55] J. Budhu, N. Ventresca, and A. Grbic, "Unit cell design for aperiodic metasurfaces," *IEEE Transactions on Antennas and Propagation*, vol. 71, no. 9, pp. 7387–7394, 2023.

[56] A. Epstein and G. V. Eleftheriades, "Arbitrary power-conserving field transformations with passive lossless omega-type bianisotropic metasurfaces," *IEEE Transactions on Antennas and Propagation*, vol. 64, no. 9, pp. 3880–3895, 2016.

[57] J. P. S. Wong, A. Epstein, and G. V. Eleftheriades, "Reflectionless wide-angle refracting metasurfaces," *IEEE Antennas and Wireless Propagation Letters*, vol. 15, pp. 1293–1296, 2016.

[58] A. H. Abdelrahman, F. Yang, A. Z. Elsherbeni, and P. Nayeri, "Analysis and design of transmitarray antennas," in *Synthesis Lectures on Antennas*, 2017. [Online]. Available: https://link.springer.com/book/10.1007/978-3-031-01541-0

[59] K. Achouri and C. Caloz, *Electromagnetic metasurfaces: Theory and applications*. John Wiley & Sons, 2021.

[60] V. G. Ataloglou, M. Chen, M. Kim, and G. V. Eleftheriades, "Microwave huygens' metasurfaces: Fundamentals and applications," *IEEE Journal of Microwaves*, vol. 1, no. 1, pp. 374–388, 2021.

[61] A. Clemente, L. Dussopt, R. Sauleau, P. Potier, and P. Pouliguen, "1-bit reconfigurable unit cell based on pin diodes for transmit-array applications in x -band," *IEEE Transactions on Antennas and Propagation*, vol. 60, no. 5, pp. 2260–2269, 2012.

[62] A. Clemente, F. Diaby, L. D. Palma, L. Dussopt, and R. Sauleau, "Experimental validation of a 2-bit reconfigurable unit-cell for transmitarrays at ka-band," *IEEE Access*, vol. 8, pp. 114 991–114 997, 2020.

[63] B. Zheng, H. Ren, S. An, H. Tang, H. Li, M. Haerinia, Y. Dong, C. Fowler, and H. Zhang, "Tunable metasurface with dynamic amplitude and phase control," *IEEE Access*, vol. 9, pp. 104 522–104 529, 2021.

[64] T. Sleasman, R. Duggan, R. S. Awadallah, and D. Shrekenhamer, "Dual-resonance dynamic metasurface for independent magnitude and phase modulation," *Phys. Rev. Appl.*, vol. 20, p. 014004, Jul 2023. [Online]. Available: https://link.aps.org/doi/10.1103/PhysRevApplied.20.014004

[65] A. Clemente, L. Dussopt, R. Sauleau, P. Potier, and P. Pouliguen, "Wideband 400-element electronically reconfigurable transmitarray in x band," *IEEE Transactions on Antennas and Propagation*, vol. 61, no. 10, pp. 5017–5027, 2013.

[66] T. Jiang, Z. Wang, D. Li, J. Pan, B. Zhang, J. Huangfu, Y. Salamin, C. Li, and L. Ran, "Low-dc voltage-controlled steering-antenna radome utilizing tunable active metamaterial," *IEEE Transactions on Microwave Theory and Techniques*, vol. 60, no. 1, pp. 170–178, 2012.

[67] H. Li, C. Ma, D. Ye, Y. Sun, W. Zhu, C. Li, and L. Ran, "Dual-band fresnel zone plate antenna with independently steerable beams," *IEEE Transactions on Antennas and Propagation*, vol. 66, no. 4, pp. 2113–2118, 2018.

[68] S. Cho, A. Salim, and H.-J. Song, "Two-dimensional beam steering active lens with simple grid bias lines at 19 ghz," *IEEE Transactions on Vehicular Technology*, vol. 70, no. 10, pp. 9716–9724, 2021.

[69] J. Y. Lau and S. V. Hum, "A planar reconfigurable aperture with lens and reflectarray modes of operation," *IEEE Transactions on Microwave Theory and Techniques*, vol. 58, no. 12, pp. 3547–3555, 2010.

[70] M. Kim and G. V. Eleftheriades, "Reconfigurable leaky-wave antennas with independent control of the leakage constant and radiation angle," in *2020 14th European Conference on Antennas and Propagation (EuCAP)*, 2020, pp. 1–5.

[71] X. Wang, P.-Y. Qin, A. Tuyen Le, H. Zhang, R. Jin, and Y. J. Guo, "Beam scanning transmitarray employing reconfigurable dual-layer huygens element," *IEEE Transactions on Antennas and Propagation*, vol. 70, no. 9, pp. 7491–7500, 2022.

[72] Z. H. Jiang, Y. Zhang, and W. Hong, "Anisotropic impedance surface-enabled low-profile broadband dual- circularly polarized multibeam reflectarrays for ka-band applications," *IEEE Transactions on Antennas and Propagation*, vol. 68, no. 8, pp. 6441–6446, 2020.

[73] P. Camacho, K. Glatre, E. Baladi, and M. S. Sharawi, "Large, multi-faceted reflectarray with quasi-constant directivity in the v-band," in *2024 18th European Conference on Antennas and Propagation (EuCAP)*, 2024, pp. 1–5.

[74] C. Balanis, "Antenna theory: Analysis and design," in *Antenna Theory: Analysis and Design*. Wiley, 2015, ch. 2 Fundamental Parameters and Figures-of-Merit of Antennas.

[75] TICRA, QUPES, Denmark, https://www.ticra.com/software/qupes/.

[76] B. Toh, R. Cahill, and V. Fusco, "Understanding and measuring circular polarization," *IEEE Transactions on Education*, vol. 46, no. 3, pp. 313–318, 2003.

[77] C. Liu, F. Yang, S. Xu, and M. Li, "An e-band reconfigurable reflectarray antenna using p-i-n diodes for millimeter-wave communications," *IEEE Transactions on Antennas and Propagation*, vol. 71, no. 8, pp. 6924–6929, 2023.

[78] P. Camacho, K. Glatre, E. Baladi, and M. S. Sharawi, "A large, seven-faceted reflectarray for millimiter-wave applications," in *2024 IEEE International Symposium on Antennas and Propagation and INC/USNC-URSI Radio Science Meeting (AP-S/INC-USNC-URSI)*, 2024, pp. 2369–2370.

[79] M. U. Afzal and K. P. Esselle, "Steering the beam of medium-to-high gain antennas using near-field phase transformation," *IEEE Transactions on Antennas and Propagation*, vol. 65, no. 4, pp. 1680–1690, 2017.

[80] M. Kim and G. V. Eleftheriades, "Guided-wave-excited binary huygens' metasurfaces for dynamic radiated-beam shaping with independent gain and scan-angle control," *Phys. Rev. Appl.*, vol. 15, p. 054037, May 2021. [Online]. Available: https://link.aps.org/doi/10.1103/PhysRevApplied.15.054037

[81] A. Olk and D. Powell, "Accurate metasurface synthesis incorporating near-field coupling effects," *Phys. Rev. Applied*, vol. 11, p. 064007, Jun 2019. [Online]. Available: https://link.aps.org/doi/10.1103/PhysRevApplied.11.064007

[82] P. Camacho and M. S. Sharawi, "Active unit cell with continuous transmission phase for a radome-periodic structure in s-band," in *2022 16th European Conference on Antennas and Propagation (EuCAP)*, 2022, pp. 1–4.

[83] D. M. Pozar, *Microwave engineering*. John wiley & sons, 2011.

[84] "Skyworks plastic surface mount (smt) hyperabrupt varactor diodes," 2023, https://www.skyworksinc.com/en/Product-Specification?family=Diodes&categories=Plastic%20Surface%20Mount%20(SMT)%20Hyperabrupt%20Varactor%20Diodes [Accessed: 2024-05-07].

[85] P. Nayeri, F. Yang, and A. Z. Elsherbeni, *Analysis and Design of Reflectarray Elements*, 2018, pp. 9–48.

[86] M. Chen, *Design and Applications of Printed-Circuit-Board Huygens' Metasurfaces*. University of Toronto (Canada), 2021.

[87] A. K. Bhattacharyya, *Phased array antennas: Floquet analysis, synthesis, BFNs and active array systems*. John Wiley & Sons, 2006, vol. 179.

[88] D. Frickey, "Conversions between s, z, y, h, abcd, and t parameters which are valid for complex source and load impedances," *IEEE Transactions on Microwave Theory and Techniques*, vol. 42, no. 2, pp. 205–211, 1994.

[89] M. K. Emara, D. Kundu, K. Macdonell, L. M. Rufail, and S. Gupta, "Coupled resonator-based metasurface reflector with enhanced magnitude and phase coverage," *IEEE Transactions on Antennas and Propagation*, vol. 72, no. 1, pp. 901–914, 2024.

[90] J. R. Reis, N. Copner, A. Hammoudeh, Z. M.-E. Al-Daher, R. F. S. Caldeirinha, T. R. Fernandes, and R. Gomes, "Fss-inspired transmitarray for two-dimensional antenna beamsteering," *IEEE Transactions on Antennas and Propagation*, vol. 64, no. 6, pp. 2197–2206, 2016.

[91] S. Cho, A. Salim, and H.-J. Song, "Two-dimensional beam steering active lens with simple grid bias lines at 19 ghz," *IEEE Transactions on Vehicular Technology*, vol. 70, no. 10, pp. 9716–9724, 2021.

[92] C. Huang, W. Pan, X. Ma, B. Zhao, J. Cui, and X. Luo, "Using reconfigurable transmitarray to achieve beam-steering and polarization manipulation applications," *IEEE Transactions on Antennas and Propagation*, vol. 63, no. 11, pp. 4801–4810, 2015.

APPENDIX A DEVELOPMENT OF THE REACTANCE'S EQUATIONS FOR A THREE-LAYER UNIT CELL

Consider the ABCD parameters of transmission lines (A.1), which represents the dielectrics of the unit cell (UC). k_{diel} is the wavenumber, t_{diel} the thickness, and η_{diel} the impedance. Likewise, the impedance of the metallic layers is represented by the ABCD parameters (A.2). The ABCD parameters of the complete UC is the cascade of all the elements as shown in (A.3).

$$\begin{aligned} M_{diel} &= \begin{pmatrix} \alpha_{diel} & \beta_{diel} \\ \gamma_{diel} & \alpha_{diel} \end{pmatrix} \\ &= \begin{pmatrix} cos(k_{diel}t_{diel}) & j\eta_{diel}sin(k_{diel}t_{diel}) \\ jsin(k_{diel}t_{diel})/\eta_{diel} & cos(k_{diel}t_{diel}) \end{pmatrix} \end{aligned} \tag{A.1}$$

$$M_{Y_n} = \begin{pmatrix} 1 & 0 \\ 1/Z_n & 1 \end{pmatrix} \tag{A.2}$$

$$M_{3lay} = M_{rad}M_{Ytop}M_{sub}M_{Ymid}M_{sub}M_{Ybot}M_{rad} \tag{A.3}$$

Isolating the radome's parameters M_{rad} in (A.3) leads to (A.4)

$$M_{rad}^{-1}M_{3lay}M_{rad}^{-1} = M_{Ytop}M_{sub}M_{Ymid}M_{sub}M_{Ybot} \tag{A.4}$$

Substituting (A.1) and (A.2) in (A.4) gives (A.5) and (A.6).

$$M_{rad}^{-1}M_{3lay}M_{rad}^{-1} = \begin{pmatrix} \frac{\mathrm{A}\alpha_r^2-\alpha_r(\mathrm{B}\Upsilon_r+\mathrm{C}\beta_r)+\mathrm{D}\beta_r\Upsilon_r}{(\alpha_r^2-\beta_r\Upsilon_r)^2} & \frac{-(\mathrm{A}+\mathrm{D})\alpha_r\beta_r+\mathrm{B}\alpha_r^2+\mathrm{C}\beta_r^2}{(\alpha_r^2-\beta_r\Upsilon_r)^2} \\ \frac{-(\mathrm{A}+\mathrm{D})\alpha_r\Upsilon_r+\mathrm{B}\Upsilon_r^2+\mathrm{C}\alpha_r^2}{(\alpha_r^2-\beta_r\Upsilon_r)^2} & \frac{\mathrm{A}\beta_r\Upsilon_r-\alpha_r(\mathrm{B}\Upsilon_r+\mathrm{C}\beta_r)+\mathrm{D}\alpha_r^2}{(\alpha_r^2-\beta_r\Upsilon_r)^2} \end{pmatrix} \tag{A.5}$$

$$M_{Ytop}M_{sub}M_{Ymid}M_{sub}M_{Ybot} =$$
$$\begin{pmatrix} \alpha_s^2+\alpha_s\beta_s(Y_{mid}+2Y_{bot})+\beta_s\left(Y_{mid}Y_{bot}\beta_s+\Upsilon_s\right) \\ \alpha_s\left(\beta_s(Y_{top}Y_{mid}+2Y_{top}Y_{bot}+Y_{mid}Y_{bot})+2\Upsilon_s\right)+\alpha_s^2(Y_{top}+Y_{mid}+Y_{bot})+\beta_s\left(Y_{top}Y_{mid}Y_{bot}\beta_s+\Upsilon_s(Y_{top}+Y_{bot})\right) \\ \beta_s\left(2\alpha_s+Y_{mid}\beta_s\right) \\ \alpha_s^2+\alpha_s\beta_s(2Y_{top}+Y_{mid})+\beta_s\left(Y_{top}Y_{mid}\beta_s+\Upsilon_s\right) \end{pmatrix} \tag{A.6}$$

Equating (A.5) and (A.6) allows to calculate Y_{mid} from the equation of column 2, row 1:

$$\begin{aligned} \beta_s\left(2\alpha_s+Y_{mid}\beta_s\right) &= \frac{-(\mathrm{A}+\mathrm{D})\alpha_r\beta_r+\mathrm{B}\alpha_r^2+\mathrm{C}\beta_r^2}{\left(\alpha_r^2-\beta_r\Upsilon_r\right)^2} \\ \Rightarrow Y_{mid} &= \frac{-A\alpha_r\beta_r+B\alpha_r^2+C\beta_r^2-D\alpha_r\beta_r+4\alpha_r^2\beta_r\gamma_r\alpha_s\beta_s-2\beta_r^2\gamma_r^2\alpha_s\beta_s-2\alpha_r^4\alpha_s\beta_s}{\beta_s^2(\alpha_r^2-\beta_r\gamma_r)^2} \end{aligned} \tag{A.7}$$

Next, Y_2 is replaced in (A.6) and the expressions of the row 2, column 2 is equated to the corresponding one of (A.5) to calculate $Ytop$:

$$\alpha_s^2+\alpha_s\beta_s(2Y_{top}+Y_{mid})+\beta_s\left(Y_{top}Y_{mid}\beta_s+\Upsilon_s\right)=\frac{\mathrm{A}\beta_r\Upsilon_r-\alpha_r\left(\mathrm{B}\Upsilon_r+\mathrm{C}\beta_r\right)+\mathrm{D}\alpha_r^2}{\left(\alpha_r^2-\beta_r\Upsilon_r\right)^2}$$

$$\begin{aligned} \Rightarrow Y_{top} = &-\frac{\beta_r\gamma_r\left(-A+\beta_r\gamma_r\alpha_s^2+\beta_r\gamma_r\beta_s\gamma_s+Z_{mid}^{-1}\beta_r\gamma_r\alpha_s\beta_s\right)+\alpha_r\left(B\gamma_r+C\beta_r\right)}{\beta_s\left(\alpha_r^2-\beta_r\gamma_r\right)^2\left(2\alpha_s+Z_{mid}^{-1}\beta_s\right)} \\ &+\frac{-\alpha_r^2\left(D+2\beta_r\gamma_r\alpha_s^2+2\beta_r\gamma_r\beta_s\gamma_s+2Z_{mid}^{-1}\beta_r\gamma_r\alpha_s\beta_s\right)+\alpha_r^4\left(\alpha_s^2+\beta_s\gamma_s+Z_{mid}^{-1}\alpha_s\beta_s\right)^{-1}}{\beta_s\left(\alpha_r^2-\beta_r\gamma_r\right)^2\left(2\alpha_s+Z_{mid}^{-1}\beta_s\right)} \end{aligned} \tag{A.8}$$

Finally, Y_{bot} can be calculated from equating the expression form the position in row 1, column 1. Since the UC is symmetric, it leads to Y_{bot}=Y_{top}, which is the same expression (A.8).

The impedances are calculated as the inverse of the admittances shown in (A.7) and (A.8).